X-ray resonant magnetic scattering investigations of hexagonal multiferroics $R\mathbf{MnO_3}$ (R = **Dy, Ho, Er**)

by

Shibabrata Nandi

A dissertation submitted to the graduate faculty

in partial fulfillment of the requirements for the degree of

DOCTOR OF PHILOSOPHY

Major: Condensed Matter Physics

Program of Study Committee:
Alan I. Goldman, Major Professor
Paul C. Canfield
Joerg Schmalian
Jianwei Qiu
Xiaoli Tan

Iowa State University

Ames, Iowa

2009

TABLE OF CONTENTS

LIST OF TABLES

LIST OF FIGURES

CHAPTER 1. INTRODUCTION TO MULTIFERROIC COMPOUNDS

Electricity and magnetism were unified into a common subject by James Clerk Maxwell in the nineteenth century yielding the electromagnetic theory.[1] Four equations govern the dynamics of electric charges and magnetic fields, commonly known as Maxwell's equations. Maxwell's equations demonstrate that an accelerated charged particle can produce magnetic fields and a time varying magnetic field can induce a voltage − thereby linking the two phenomena. However, in solids, electric and magnetic ordering are most often considered separately and usually with good reason: the electric charges of electrons and ions are responsible for the charge effects, whereas the electron spin governs magnetic properties.[2, 3]

In some materials ferroelectric and magnetic order coexist and are termed magnetoelectric multiferroics. The beginning of this field dates to 1959 with a short re-mark by Landau and Lifshitz in the book "Course of Theoretical Physics":[4] "*Let us point out two more phenomena, which, in principle, could exist. One is piezomagnetism, which consists of linear coupling between a magnetic field in a solid and a deformation (analogous to piezoelectricity). The other is a linear coupling between magnetic and electric fields in a media, which would cause, for example, a magnetization proportional to an electric field. Both these phenomena could exist for certain classes of magnetocrystalline symmetry. We will not however discuss these phenomena in more detail because it seems that till present, presumably, they have not been observed in any substance."* Before proceeding further, it is useful to define several terms used by researchers in this field.

1. Definition of multiferroics: According to Schmidt[5] multiferroic materials are those which combine two or more *"ferroic"* properties such as electric polarization, magnetization and strain. The mutual cross-coupling between these properties and the control of them by

external perturbations are shown in Fig. 1.1.

2. Definition of magnetoelectric multiferroics: Magnetoelectric multiferroic materials are those in which ferroelectricity (antiferroelectricity) and ferromagnetism (antiferromagnetism) coexist within the same phase. In these materials, the magnetoelectric effect, the induction of a magnetization by an electric field, or of polarization by a magnetic field should in principle exist and can yield entirely new device paradigms, such as the above mentioned electric field-controlled magnetic data storage. The cross coupling between ferromagnetism and ferroelectricity and the possibility of a multistage memory device is illustrated in Fig. 1.2.

After the disclaimer by Landau and Lifshitz, Dzyaloshinskii predicted,[6] and Astrov observed,[7] this type of coupling, which is now known as the linear magnetoelectric effect. This was followed by the discovery of compounds and their classification by Hans Schmidt.[5] However, in general multiferroicity proved to be difficult to find as these two order parameters are, for the most part, mutually exclusive.[8]

The renaissance of magnetoelectric multiferroics was initially triggered by the proposal by Lottermoser *et al.*[9, 10] that the magnetic phase can be controlled by an applied electric fields and, later, by the discovery of spiral magnets where ferroelectricity is induced by the spiral magnetic order. This recent boom in multiferroic research is driven by potential applications as well as fundamental science. For example, controlling charges by an applied magnetic field and magnetic moments by an applied electric field opens the possibility of multistage memory devices with high data density. It also offers some advantages to the present day memory devices such as FRAMs (ferromagnetic random access memory) and FeRAMs (ferroelectric random access memory). The primary disadvantage of FRAMs is that the write operation requires substantial current to generate the field for "writing" and, therefore, this process is dissipative. Applying an electric field to write the data is relatively easy, fast and does not involve dissipation effects. On the other hand, for FeRAMs, the primary disadvantage is the read operation which requires discharging the capacitor during the read and recharging again to reset the memory back to it's initial value. Therefore, writing data by applying an electric

field and reading the data magnetically could (possibly) optimize both processes.[11] From the theory point of view, studies have shown that the usual atomic-level mechanisms driving ferromagnetism and ferroelectricity are mutually exclusive because they require empty and partially filled transition metal orbitals, respectively.[8] Therefore, understanding the coexistence between ferroelectricity and magnetism in the same material presents a theoretical challenge.

1.1 The Classification of Multiferroic Compounds

In a ferromagnetic (antiferromagnetic) material time-reversal symmetry is spontaneously broken and all magnetic moments point in the same (opposite) direction as illustrated in Fig. 1.3. Broken time reversal symmetry implies a change of sign of the magnetic moment under the symmetry operation, $\mathbf{M}(-\mathrm{t}) = -\mathbf{M}$ whereas the polarization remains invariant, $\mathbf{P}(-\mathrm{t}) = \mathbf{P}$. Changing the sign of a magnetic moment by time reversal can be understood by visualizing the magnetic moment as a current carrying loop, with $\mathrm{j} = \mathrm{dq/dt}$. Therefore, as $\mathrm{t}\rightarrow-\mathrm{t}$, $\mathrm{j}' = \mathrm{dq/d}(-\mathrm{t}) = -\mathrm{j}$; and hence, under time reversal symmetry operation, $\mathbf{M} \rightarrow -\mathbf{M}$, as shown in Fig. 1.3. In a ferroelectric material, space inversion symmetry is spontaneously broken below the ferroelectric transition temperature i.e $\mathbf{P}(-x) = -\mathbf{P}$ whereas for magnetism it remain invariant. The effect of space inversion symmetry on a ferroelectric material is shown in Fig. 1.4.

Depending on the origin of ferroelectricity, Cheong and Mostovoy[2] have classified ferroelectrics within two categories, 'proper' and 'improper' as shown in Table 1.1. In 'proper' ferroelectrics, ferroelectricity occurs due to electronic pairing between the transition metal ion (e.g. Ti in $BaTiO_3$) and oxygen. On the other hand, in 'improper' ferroelectrics, ferroelectricity arises due to complex lattice distortions or by other types of ordering such as charge ordering and magnetic ordering.

1.2 The Origin of Multiferroicity

Multiferroic effects can originate for different reasons. For example, lattice distortions can give rise to a lower symmetry non-centrosymmetric ferroelectric state. Antiferromagnetic order

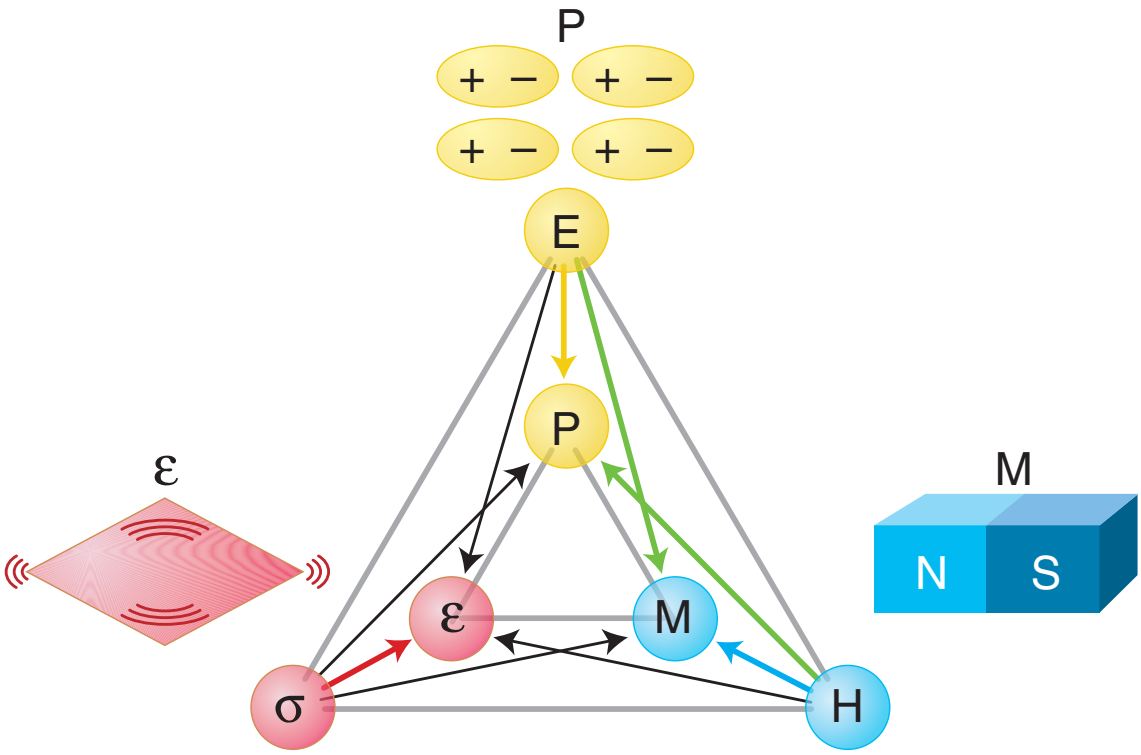

Figure 1.1 Phase control in ferroics and multiferroics. The electric field E, magnetic field H, and stress σ control the electric polarization P, magnetization M, and strain ϵ, respectively. In a ferroic material, P, M, or ϵ are spontaneously formed to produce ferromagnetism, ferroelectricity, or ferroelasticity, respectively. In a multiferroic, the coexistence of at least two ferroic forms of ordering leads to additional interactions. In a magnetoelectric multiferroic, a magnetic field may control P or an electric field may control M (green arrows). After Ref. [10].

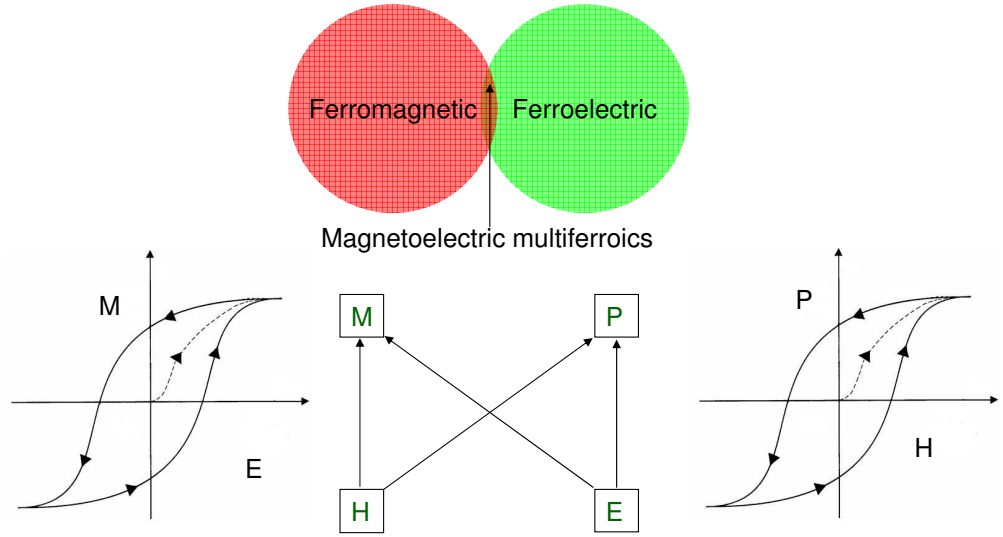

Figure 1.2 Magnetoelectric multiferroics combine ferromagnetic (antiferromagnetic) and ferroelectric (antiferroelectric) properties in the same phase. In general, the magnetization of a ferromagnetic material shows a M-H hysteresis loop and a ferroelectric material shows a P-E hysteresis loop. In ideal multiferroics (for memory device applications), there should be a magnetic hysteresis loop in an applied electric field (left figure) and a ferroelectric hysteresis loop in an applied magnetic field. The above figure also illustrates the possibility of a four stage memory device: (+**M**+**P**), (+−), (−+) and (−−)

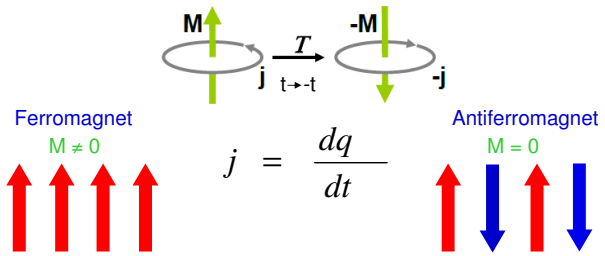

Figure 1.3 1-D schematic of a ferromagnet and an antiferromagnet. In a ferromagnetic material the net magnetization is non-zero. In the case of an antiferromagnet, the net magnetization is zero, however, sublattice magnetization is non-zero. The upper part of the figure shows effect of the time reversal symmetry (T) on a current carrying loop.

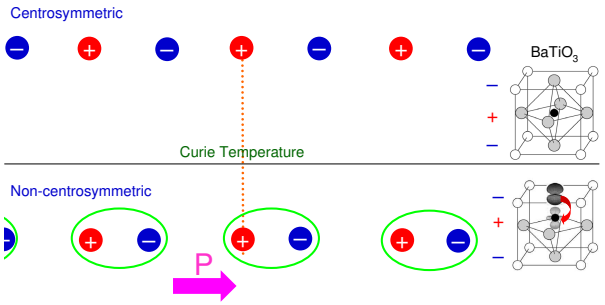

Figure 1.4 1-D schematic of a ferroelectric material. In a ferroelectric material the net polarization is non-zero below the ferroelectric Curie temperature. The dotted red line shows the center of space inversion symmetry in the paraelectric cetrosymmetric phase. This center of symmetry is spontaneously broken in the ferroelectric phase. The right figure shows a real example of a typical ferroelectric material $BaTiO_3$ where space inversion symmetry is broken by the off-center displacement of Ti^{4+} ion that occurs due to the Ti^{4+}-O^{3-} hybridization.

Table 1.1 Classification of ferroelectrics after Ref. [2]

	Mechanism of Inversion Symmetry Breaking	Materials
Proper	Covalent bonding between $3d^0$ transition metal (Ti) and Oxygen (O)	$BaTiO_3$
	Polarization of $6s^2$ lone pair of Bi or Pb	$BiMnO_3$, $BiFeO_3$, $Pb(Fe_{2/3}W_{1/3})O_3$
Improper	Structural transition 'Geometric ferroelectrics'	K_2SeO_4, Cs_2CdI_4, Hexagonal RMnO$_3$
	Charge ordering: 'Electronic ferroelectrics'	$LuFe_2O_4$
	Magnetic ordering: 'Magnetic ferroelectrics'	Orthorhombic RMnO$_3$, RMn$_2$O$_5$, $CoCr_2O_4$

may then arise due to the presence of magnetic ions in the system and thus, the system may be classified as multiferroic. This is the case for hexagonal mutiferroics such as RMnO$_3$ (R = Ho−Lu, Sc, Y). On the other-hand, there are some compounds where first antiferromagnetism sets in and, at some lower temperature, due to a specific magnetic order, spatial inversion symmetry is broken and ferroelectricity results. This is the case for the orthorhombic multiferroics such as RMnO$_3$ compounds with R = Gd, Tb, and Dy. For charge ordered multiferroics such as $LuFe_2O_4$, a specific charge ordering induces ferroelectricity. We will discuss individual origins in detail below.

Magnetic Ordering as the Origin of Ferroelectricity

Here we outline the origin of ferroelectricity for the orthorhombic RMnO$_3$ multiferroic compounds. In this class of compounds, a particular arrangement of magnetic moments induces ferroelectricity as first illustrated by Kenzelmann *et al.*[12] in the compound $TbMnO_3$. The same mechanism was employed to explain ferroelectricity in several other orthorhombic com-

pounds including $Ni_3V_2O_8$,[13] $MnWO_4$[14] and $Eu_{1-x}Y_xMnO_3$ ($x = 0.55$)[15]. For $TbMnO_3$ the Mn^{3+} moments order at $T = 41$ K in an amplitude modulated sinusoidal structure with moments in the **b** direction of the orthorhombic *Pbnm* structure and a magnetic propagation vector $\mathbf{Q} \approx (0\ 0.27\ 0)$. The magnetic order of the Mn^{3+} moments changes from an amplitude modulated sinusoidal structure to a spiral like structure at $T = 28$ K. The spiral magnetic structure breaks the space inversion symmetry and induces a polarization as illustrated in Fig. 1.5.

The origin of magnetically induced polarization can be understood phenomenologically by the theory developed by Mostovoy[16] or microscopically by spin current model developed by Katsura *et al.*[16, 17]. According to Ginzburg-Landau theory, applied by Mostovoy, the form of the coupling between the electric polarization **P** and magnetization **M** depends on the transformation properties of these two variables upon time reversal and space inversion, mentioned above. The simultaneous invariance upon time reversal (t$\rightarrow -$t) and space inversion ($x \rightarrow -x$) suggests that the lowest order coupling must be quadratic in **M** as well as **P**. Thus, a fourth order term in free energy of the form $-P^2M^2$ is expected. However, this term does not induce ferroelectricity because the energy cost of a polar lattice distortion proportional to $+P^2$ will overcompensate the energy gain by $-P^2M^2$.[2] However, a coupling linear in **P** and quadratic in **M** is allowed if there is a spatial variation in **M**. Therefore, the lowest order magnetoelectric coupling term has the form [16]

$$\Phi_{em}(\mathbf{P}, \mathbf{M}) = \gamma \mathbf{P} \cdot [\mathbf{M}(\nabla \cdot \mathbf{M}) - (\mathbf{M} \cdot \nabla)\mathbf{M} + ...] \tag{1.1}$$

where γ is an arbitrary constant. The "electric part" of the thermodynamic potential has the form $\Phi_e(\mathbf{P}) = \frac{P^2}{2\chi_e}$ where χ_e is the dielectric susceptibility in the absence of magnetism. The variation of $\Phi_e + \Phi_{em}$ with respect to **P** gives

$$\mathbf{P} = \gamma \chi_e [(\mathbf{M} \cdot \nabla)\mathbf{M} - \mathbf{M}(\nabla \cdot \mathbf{M})] \tag{1.2}$$

Now, assuming a helical magnetic structure of the form

$$\mathbf{M} = M_1 \mathbf{e}_1 \cos(\mathbf{Q} \cdot \mathbf{x}) + M_2 \mathbf{e}_2 \sin(\mathbf{Q} \cdot \mathbf{x}) + M_3 \mathbf{e}_3 \tag{1.3}$$

and using the above equation for polarization 1.2, the average polarization can be written as

$$\bar{\mathbf{P}} = \frac{1}{V}\int d^3x\mathbf{P} = \gamma\chi_e M_1 M_2[\mathbf{e}_3 \times \mathbf{Q}] \tag{1.4}$$

where, the $\mathbf{e}_i$, i = 1, 2, 3, form an orthogonal basis. $\mathbf{Q}$ is the propagation vector. Equation 1.3 describes a helix with spin rotation axis $\mathbf{e}_3$ if M_1, $M_2 \neq 0$. If also M_3 is non-zero, then the magnetic structure is conical helix. No polarization is induced for a pure sinusoidal structure as can be understood from Eq. 1.4 since a sinusoidal wave is described by only one component of the magnetic moment (M_1 or M_2). In this case, inversion symmetry remains intact as shown in Fig. 1.5(a).[18] The important thing is to note from Eq. 1.4 is that the polarization is non-zero for a helix only if the spin rotation axis $\mathbf{e}_3$ and $\mathbf{Q}$ are not parallel. In this situation the space inversion symmetry is broken and a finite polarization can be induced as illustrated in Fig. 1.5(b). Using the aforementioned theory, the induced polarization in the magnetically ordered state of $TbMnO_3$ can be explained. For example, the Mn^{3+} moments order sinusoidally in the temperature range 28 K$\leq T \leq$ 41 K without any polarization. Below 28 K, the sinusoidal order is replaced by a helix with $\mathbf{Q}\| \mathbf{b}$. Since the Mn^{3+} moments rotate in the **b-c** plane, the spin rotation axis is $\mathbf{e}_3 \| \mathbf{a}$, and thus, $\mathbf{P} \| \mathbf{c}$ is expected according to Eq. 1.4 and is observed experimentally.[12] Here we note that the spiral magnetic order with broken inversion symmetry can be found in metallic systems but no ferroelectric effect will be seen. Observation of induced polarization requires an insulating material.

As explained above, the polarization is induced by a specific magnetic structure and so, this type of multiferroic shows unprecedented control of polarization under magnetic field. This has been observed for the orthorhombic RMnO$_3$ (R = Gd, Tb, and Dy)[19, 20, 21] compounds where the polarization flops when the magnetic structure flops as illustrated for the case of $Eu_{1-x}Y_xMnO_3$ (x=0.55)[15] in Fig. 1.6. Here, the polarization flops from the **a** axis to **c** axis when the magnetic filed is applied along the **a** axis due the flop of spin spiral from the **a-b** plane to the **b-c** plane. Since the polarization and dielectric constants of a material are intimately linked, this kind of multiferroic shows a giant magneto-capacitance effect.[20] Since, magnetism appears at low temperatures, cross coupling between ferroelectricity and magnetism is only observed at low temperatures and high magnetic fields.

(a)

$$\mathbf{M} = \mathbf{A}\sin Qx$$

$$\overline{\mathbf{P}} = 0$$

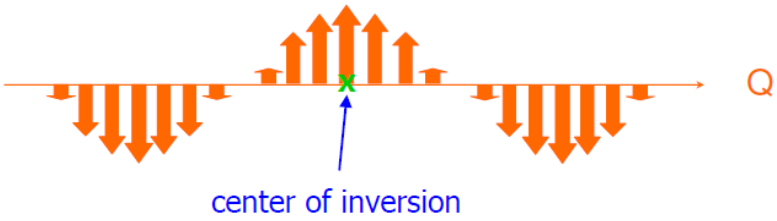

(b)

$$\mathbf{M} = M_0\left(\mathbf{e}_1\cos\mathbf{Qx} + \mathbf{e}_2\sin\mathbf{Qx}\right)$$

$$\overline{\mathbf{P}} \propto \left[\mathbf{e}_3 \times \mathbf{Q}\right]$$

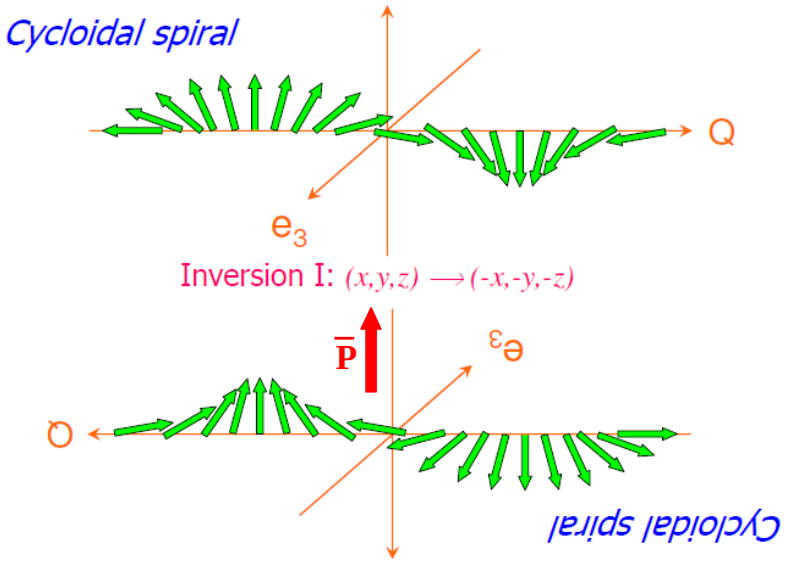

Figure 1.5 (a) For a pure sinusoidal magnetic structure space inversion symmetry is not broken and, therefore, there is no polarization that can be induced by magnetic order. (b) Breaking of space inversion symmetry from spiral magnetic order inducing a net polarization. The above two figures have been adapted from lecture note of Maxim Mostovoy.[18]

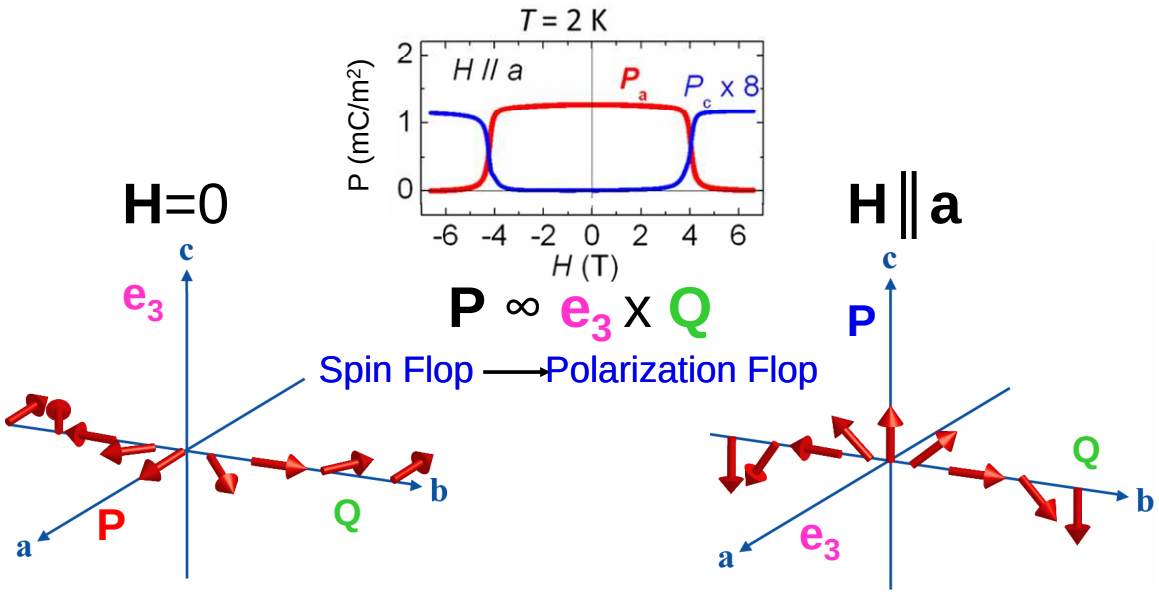

Figure 1.6 Control of magnetization by an external magnetic field illustrated for the compound $Eu_{1-x}Y_xMnO_3$ ($x = 0.55$). After Ref. [15]. Polarization $\mathbf{P}$ is proportional to $\mathbf{e}_3 \times \mathbf{Q}$, where $\mathbf{e}_3$ is the spin rotation axis and $\mathbf{Q}$ is the propagation vector (see text for details). Polarization flops from the **a** axis to **c** axis when the magnetic filed is applied along the **a** axis due the flop of spin spiral from **a-b** plane to **b-c** plane.

Exchange Striction as the Origin of Ferroelectricity

Spiral spin order is not the only means of inducing electric polarization. Polarization can also be induced by collinear magnetic order as observed for $R\mathrm{Mn_2O_5}$ (R = Gd, Tb, Dy) compounds[22] and for $\mathrm{Ca_3Co_{1.04}Mn_{0.96}O_6}$.[23] Due to the simplicity of its magnetic structure, $\mathrm{Ca_3Co_{1.04}Mn_{0.96}O_6}$ has been chosen as an example and is illustrated in Fig. 1.7. When Co ions are replaced by Mn ions in $\mathrm{Ca_3Co_2O_6}$, Mn ions have a strong tendency to avoid the trigonal prismatic oxygen coordination. Thus, for example, for equal amount of Co and Mn ions, all the Co ions are located in the trigonal prismatic sites, and all the Mn ions occupy the octahedral sites.[24] At high temperature the distance between $\mathrm{Co^{2+}}$ and $\mathrm{Mn^{4+}}$ ions are equal and, therefore, the chain has inversion symmetry and the net electric polarization is zero. However, at low temperature a specific collinear magnetic structure breaks the inversion symmetry via the exchange striction mechanism. Due to competing exchange interactions between nearest neighbor and next-nearest neighbor magnetic ions, an up-up-down-down ($\uparrow\uparrow\downarrow\downarrow$) type magnetic structure is realized at low temperatures. As a consequence of this type of magnetic structure, symmetric superexchange interaction shortens the bonds between parallel spins while the bonds between anti-parallel spins becomes elongated. Thus, inversion symmetry is broken and a spontaneous polarization is induced along the chain axis, **c**.

Charge Order as the Origin of Ferroelectricity

$\mathrm{LuFe_2O_4}$ is a well known example of a charge ordered multiferroic compound.[25, 26] The temperature variation of the electric polarization is shown in Fig. 1.8. Below 350 K, $\mathrm{LuFe_2O_4}$ shows a spontaneous polarization that increases below approximately 250 K. It was shown by Christianson *et al.*[27] that the Fe moments order ferrimagnetically at around 250 K and therefore, the increase of polarization at 250 K suggests significant coupling between ferroelectricity and the magnetic ordering.

Ferroelectricity in this material occurs due a specific charge order in the triangular lattice shown in Fig. 1.9. At temperatures above 350 K, an equal number of $\mathrm{Fe^{2+}}$ and $\mathrm{Fe^{3+}}$ ions coexist randomly at the same site in the triangular lattice and, thus, iron has an average valence of +2.5. However, at temperatures below 350 K, a charge redistribution takes place

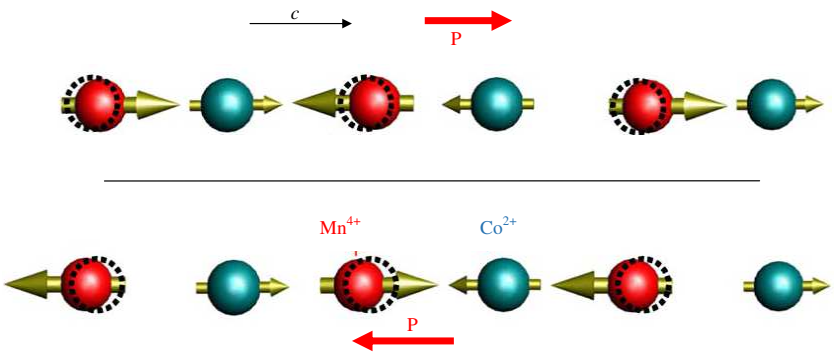

Figure 1.7 Ising chains with the up-up-down-down spin order and alternating ionic order, in which electric polarization is induced through symmetric exchange striction for the compound $Ca_3Co_{1.04}Mn_{0.96}O_6$. Two possible magnetic configurations leading to opposite polarizations are shown. The atomic positions in the undistorted chains are shown with dashed circles. After Ref. [23].

between the layers so that upper layer has a 2:1 ratio between Fe^{2+} and Fe^{3+} and the lower layer has the opposite, 1:2 ratio.[25] In this manner frustration in the triangular lattice can be broken and a charge ordered state emerges. Due to this specific charge ordered state, each plane in the bilayer structure acquires a net charge. For example, in the Fig. 1.9, the upper layer has a net positive charge and the layer below has a net negative charge and so, these two layers together (bilayer) form a dipole moment and ferroelectricity emerges.

Lattice Distortions as the Origin of Ferroelectricity: Hexagonal Mutiferroics

RMnO$_3$ (R = rare-earths) compounds with the smaller ionic radius of the heavy rare-earths (Ho-Lu and Y, Sc) generally crystallize in the hexagonal lattice.[28] The ferroelectricity in this class of compounds originates from the coordinated movement of atoms at the rare-earth site and a simultaneous rotation of the MnO_5 polyhedra below the ferroelectric transition temperature of $\sim$ 800 K.[29] The Mn^{3+} moments order in the temperature range of 80-120 K[30] and the rare-earths moments order at temperatures below the magnetic ordering of Mn^{3+}.

The origin of ferroelectricity in the hexagonal RMnO$_3$ compounds has been discussed by Van Aken *et al.*[29] for YMnO$_3$ and is shown in Figs. 1.10 and 1.11. At high temperatures, all ions are constrained within the **a-b** plane whereas, below the ferroelectric transition tem-

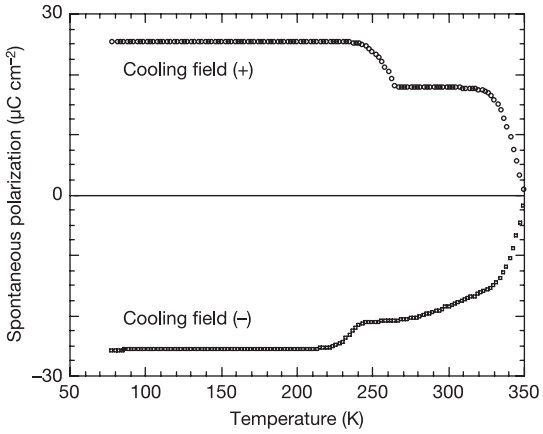

Figure 1.8 Temperature variation of the electric polarization of $LuFe_2O_4$. The plot is the integration of a pyro-electric current measurement. The current flow from the sample was recorded on heating after electric field cooling along the **c** axis. The direction of the electric polarization depends on the direction of electric field, which indicates that $LuFe_2O_4$ possesses macroscopic electric polarization. After Ref. [25].

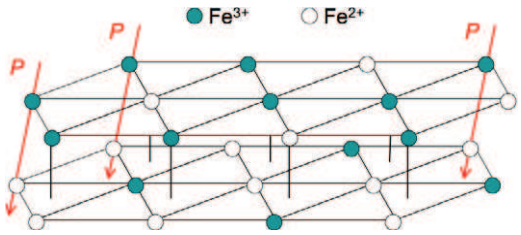

Figure 1.9 Bilayer of the FeO_2 triangular lattices in $LuFe_2O_4$ with a schematic view of charge redistribution between the layers and the interlayer charge ordering that results in a macroscopic electric polarization indicated by the red arrows. After Ref. [26].

perature, the mirror plane perpendicular to the **c** axis is lost. There are two major changes in the structure during the ferroelectric phase transition. The first one is the buckling of MnO_5 polyhedra leading to a shorter **c** axis. The second change involves the rotation of the MnO_5 polyhedra and movement of Y ion such that Mn remains at the center of the polyhedra leaving the Y-O_T (O_T is the apical oxygen atom) bond length unchanged while the Y-O_P (O_P is in plane oxygen atom) bond lengths change: some of the bonds become shorter while others become elongated. The change of the Y-O_P bond lengths, as well as the rotation of the MnO_5 polyhedra, is demonstrated in Fig. 1.11. One can easily see that there are two "down" dipoles per one "up" dipole and therefore, the system becomes ferroelectric (properly called 'ferrielectric"). Due to this *ferrielectric* property, although the displacement is large and comparable to conventional ferroelectrics like $BaTiO_3$ and $PbTiO_3$, the net polarization is small compared to $BaTiO_3$ and $PbTiO_3$ (in $BaTiO_3$, P = $25\mu Ccm^{-2}$ and $PbTiO_3$, P = $75\mu Ccm^{-2}$ which is much greater than P = $5\mu Ccm^{-2}$ for $YMnO_3$).[29, 31] For a quantitative comparison of the magnitude of ferroelectric polarization between different compounds, a determination of the atomic displacements is necessary.

The main driving force behind the structural phase transition involves electrostatic and size effects rather than hybridization between different atoms as opposed to conventional ferroelectrics and supported by total energy calculations.[29] The Mn ion remains close to the center of the oxygen cage and moves only by $\sim$ 0.01 Å along the **c** axis. Therefore, it is unlikely that Mn ion re-hybridizes with neighboring oxygen ions. On the other hand the distance between Y-O_P after the off-center displacement is $\sim$ 2.3 Å, larger than minimum distance required for the bond to be fully ionic[32] and, therefore, rehybridization between Y and O_P is also unlikely.

1.3 The Electric Field Control of Magnetism and Magnetic Field Control of Polarization

Regarding the electric field control of magnetism, there are many examples which show that antiferromagnetic domains can be controlled by external electric fields.[33, 34, 35] However,

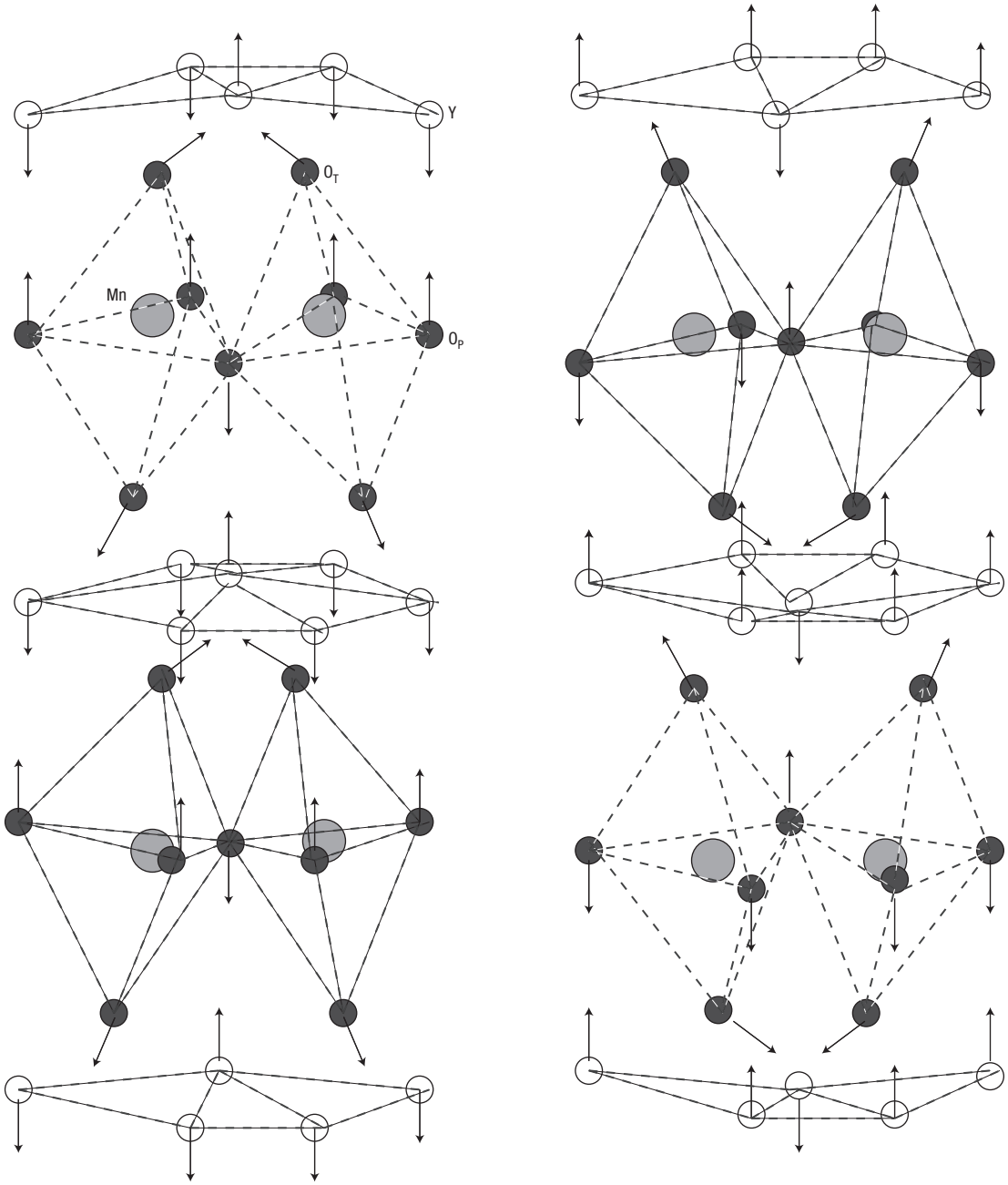

Figure 1.10 Three-dimensional schematic view of $YMnO_3$ in the two enantiomorphous polarized states. Arrows indicate the directions of the atomic displacements moving from the centrosymmetric to the ferroelectric structure. After Ref. [29].

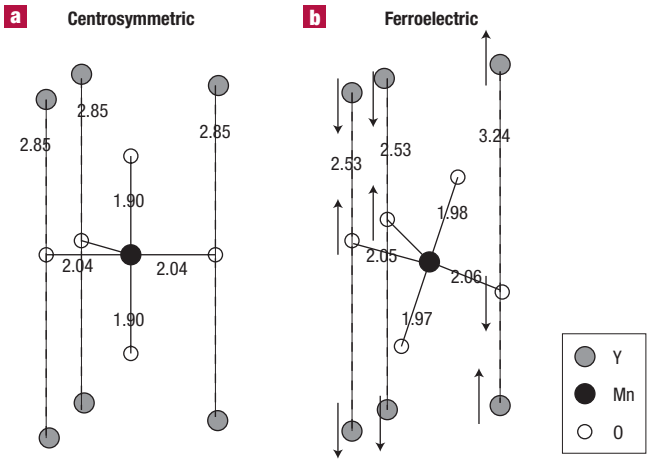

Figure 1.11 Schematic of a MnO_5 polyhedron with Y layers above and below. (a, b) The calculated atomic positions of the centrosymmetric (a) and ferroelectric structures (b) The numbers give the bond lengths in Å. The arrows indicate atomic displacements with respect to the centrosymmetric structure. After Ref. [29].

there are only a few examples, where ferromagnetism can be induced by an external electric field. Back in the 1970's it was shown that the linear magnetoelectric effect exist for chromic oxide (i.e. polarization can be induced by applied magnetic fields and magnetization can be induced by an applied electric fields).[7, 36, 37] However, the induced magnetization was very small ($\sim$ 0.03 emu/cm^3) and thus, not really practical as a multiferroic material. In 2004, Lottermoser *et al.*[9] proposed that the ferromagnetism ($\sim$ 500 emu/cm^3) can be induced in antiferromagnetic $HoMnO_3$ under an applied electric field. In particular, they proposed that, Ho^{3+} moments are responsible for the ferromagnetic response and it can be reversibly switched on and off by applying electric fields below $T = 76$ K.

The polarization can be reversibly switched along a particular crystallographic direction for RMn_2O_5 multiferroics with R = Tb [22] in a moderate magnetic field shown in Fig. 1.12. The polarization reversal in this compound has been modeled assuming that the total polarization, P, is composed of two independent components, a positive component P_1 which depends weakly on magnetic fields and a negative component P_2 which depends strongly on the magnetic field. The microscopic origin of this two components remains unknown due to the complexity of the

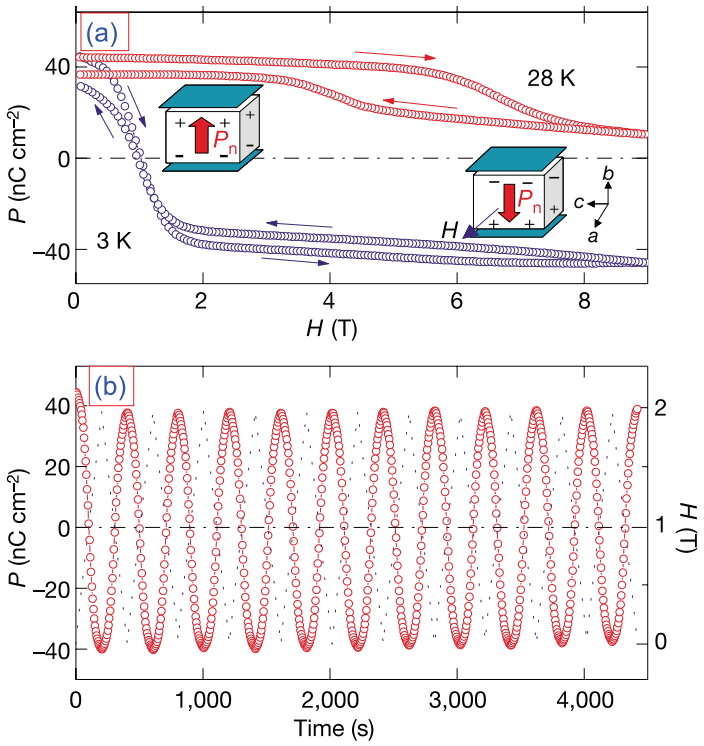

Figure 1.12 (a) Change of the total electric polarization by applied magnetic fields at 3 and 28 K for $TbMn_2O_5$. The magnetic-field dependence of the total electric polarization was obtained by measuring the magnetoelectric current as a function of magnetic field, which was varied linearly with time at a uniform rate of 100 Oe/s. The magnetoelectric current was measured after cooling with E poled (polarized with an applied electric field) along the **b** axis without magnetic field. The total polarization was obtained by adding the spontaneous polarization to the field-induced polarization, which was calculated from the magnetoelectric current. The schematic shows the orientation of the net polarization (P_n=P_1+P_2) in zero field and high fields $\geq$ 2 T. (b) Polarization flipping at 3 K by linearly varying magnetic field from 0 to 2 T. These results clearly display highly reproducible polarization switching by magnetic fields. After Ref. [22].

magnetic structure in this compound. However, it was suggested by Radaelli and Chapon[38] that the two polarization components originate from the two magnetic sublattices, Mn and Tb. The Mn sublattice remain unaffected by the applied magnetic fields while Tb becomes ferromagnetic under applied magnetic fields. Nevertheless, the microscopic origin still needs to be clarified by detailed diffraction measurements.

1.4 A Survey of the Hexagonal $R\mathbf{MnO_3}$ Compounds

$R\mathrm{MnO_3}$ (R = Ho-Lu, Y, and Sc) compounds with smaller R ionic radii generally crystallize in the hexagonal structure.[28] Under the special condition of argon gas flow in floating zone growth, however, R = Dy can be synthesized in the hexagonal form as well.[39, 40] In this class of compounds ferroelectricity originates at very high temperature due to the displacement of R atoms and buckling of the $\mathrm{MnO_5}$ polyhedra, as discussed in detail above. The magnetism in these compounds arises primarily from the $\mathrm{Mn^{3+}}$ ions, but the rare-earth ions do order at lower temperature. The magnetic ordering of $\mathrm{Mn^{3+}}$ occurs at temperatures low compared to the ferroelectric transition (70−100 K) and in this temperature range the material satisfies the condition for multiferroicity.

$R\mathbf{MnO_3}$ Crystallographic Structure and Ferroelectric Properties

The hexagonal structure of the $R\mathrm{MnO_3}$ compounds consists of non-connected layers of $\mathrm{MnO_5}$ trigonal bipyramids corner-linked by in-plane oxygen ions, with apical oxygen ions forming close-packed planes separated by a layer of R^{3+} ions. Schematic views of the crystal structure are given in Fig. 1.13 and the experimentally determined atomic positions for hexagonal $R\mathrm{MnO_3}$ are shown in Table 1.2.[28, 41]

Group theoretical analysis and high-temperature diffraction[42] have shown that the transition from the paraelectric $P6_3/mmc$ phase to the ferroelectric $P6_3cm$ phase takes place in two steps. First, the paraelectric $P6_3/mmc$ phase transforms to the non-ferroelectric $P6_3cm$ phase leading to a tripling of the unit cell at T = 1200-1450 K. At a significantly lower temperature, T = 850-1100 K, the ferroelectric transition takes place without a further reduction

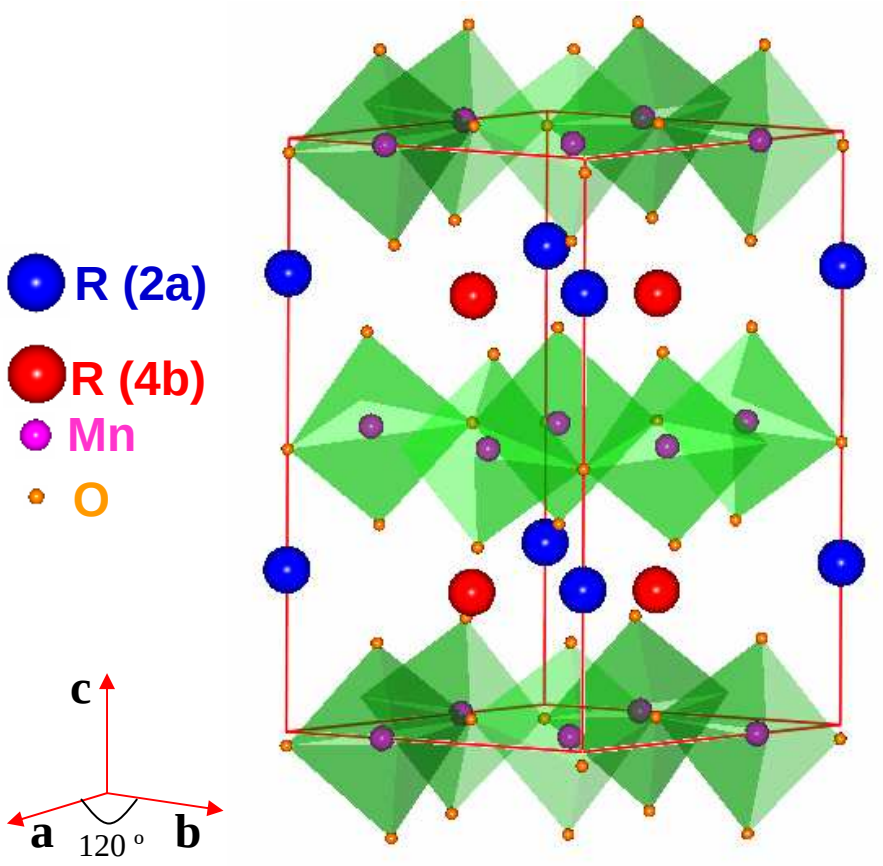

Figure 1.13 The hexagonal unit cell of $R\mathrm{MnO_3}$. Note that there are two Wyckoff sites for the rare-earth ions, $2a$ and $4b$. The $\mathrm{MnO_5}$ polyhedra is shown in green where Mn atoms are surrounded by oxygen atoms. The red line outlines the unit cell.

Table 1.2 Structural parameters for hexagonal compounds with crystallographic space group $P6_3cm$ and lattice parameters $a \approx 6.12$ Å, $c \approx 11.4$ Å. After Ref. [28, 41].

Atoms	Wyckoff site	Position	x	y	z
$R(1)$	$2a$	$(0\ 0\ z)$	0	0	0.27
$R(2)$	$4b$	$(\frac{1}{3}\ \frac{2}{3}\ z)$	$\frac{1}{3}$	$\frac{2}{3}$	0.23
Mn	$6c$	$(x\ 0\ z)$	$\approx \frac{1}{3}$	0	0
O(1)	$6c$	$(x\ 0\ z)$	$\approx \frac{1}{3}$	0	$\approx \frac{1}{6}$
O(2)	$6c$	$(x\ 0\ z)$	$\approx \frac{2}{3}$	0	$\approx \frac{1}{3}$
O(3)	$2a$	$(0\ 0\ z)$	0	0	$\approx \frac{1}{2}$
O(4)	$4b$	$(\frac{1}{3}\ \frac{2}{3}\ z)$	$\frac{1}{3}$	$\frac{2}{3}$	≈ 0

in symmetry.[29, 42]

The ferroelectric phase has $P6_3cm$ symmetry and the ferroelectric polarization is along the hexagonal **c** axis with $\mathbf{P}_c = 5.6\mu\text{Ccm}^{-2}$.[31] The value of the ferroelectric polarization is comparable to conventional ferroelectrics and, is two orders of magnitude larger than the magnetically driven ferroelectrics.[22] Despite strong magnetoelectric effects, magnetically driven ferroelectrics are not convenient for practical applications because they have to be poled frequently by applying an electric field to maintain a single ferroelectric domain state. This is necessary because their polarization is too small and they can be easily broken into multidomain polarization.[43] Thus, multiferroics with a high T_C and a robust large polarization at room temperature, such as hexagonal multiferroics, are more desirable. The single ferroelectric domain state can easily be maintained once they are poled.

Magnetic Properties

Despite numerous studies dating from the 1960s the magnetic structure and corresponding magnetic symmetries of different phases in $R\text{MnO}_3$ remain unclear, particularly for the rare-earth elements.[30, 41, 44, 45, 46, 47, 48] Details of the controversies, and their resolution by this x-ray resonant magnetic scattering study, will be discussed in Chapter 3. Despite the controversies, certain features are clear and well established about the magnetic structure of these materials: First, the magnetic unit cell is same as the crystallographic unit cell. Second, the Mn^{3+} moments order in the hexagonal **a-b** plane non-collinearly at around $T \sim 60$-100 K. Third, the Mn^{3+} moments undergo one or more reorientations within the **a-b** plane at lower temperatures. Finally, the rare-earth moments order along the hexagonal **c** direction at temperatures below the magnetic ordering of Mn^{3+} moments. The magnetic structures of the Mn^{3+} moments are well understood due to the detailed studies of Fiebig and co-workers.[45, 46, 47] The representative magnetic phase diagram for $R\text{MnO}_3$ series is shown in Fig. 1.14 for the Mn^{3+} moments, and the magnetic structure of Mn^{3+} moments at different temperatures is shown in Fig. 1.15 for HoMnO_3. For the specific case of HoMnO_3, the Mn^{3+} moments are arranged in a two-dimensional (2D) triangular lattice, with successive layers offset from each other. The Mn^{3+} moments order at $T_\text{N} = 76$ K with a spin reorientation transition at

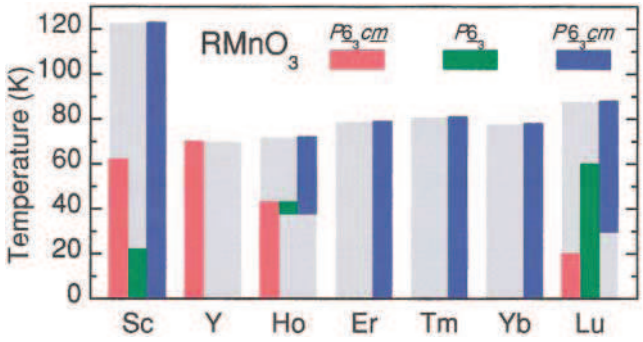

Figure 1.14 Magnetic symmetry of the hexagonal manganites. Sc, Ho, and Lu show a coexistence of magnetic phases with temperature intervals being sample specific. Intervals are thus given for a single sample. Rare-earth spins ordering below 6 K was not taken into account. After Ref. [87]

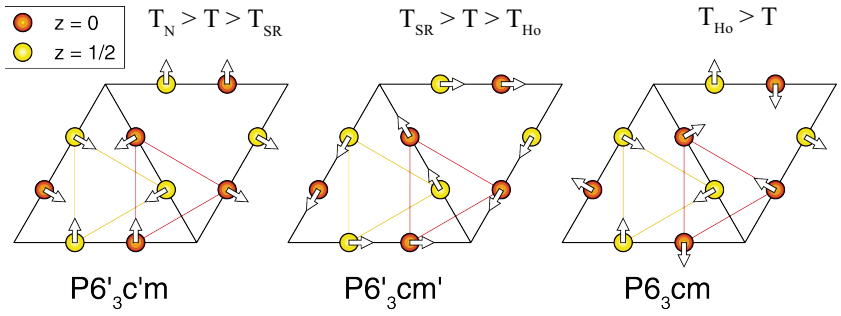

Figure 1.15 The Mn^{3+} spin configurations for three different phases of $HoMnO_3$. The open circles indicate the position of Mn ions at $z = 0$, filled circles indicate Mn ions at $z = c/2$, and arrows indicate the direction of the local magnetic moment.

$T_{\rm SR} = 40$ K. They reorient again within the plane at $T_{\rm Ho} = 5$ K, where $T_{\rm Ho}$ was the proposed ordering temperature of Ho^{3+}.[46, 49] It is worth mentioning here that the nomenclature $T_{\rm Ho} = 5$ K is misleading since an *induced* ordered component of magnetic moment can be found at 40 K (as we will show in this work).

Coupling Between Ferroelectricity and Magnetism

Among hexagonal multiferroic compounds, $HoMnO_3$ shows a large magnetoelectric coupling at the magnetic phase transitions, particularly for the intermediate magnetic phase transition (around $T = 40$ K) and at the normal Ho^{3+} ordering temperature (around 5 K) shown in

Fig. 1.16. The coupling between the in-plane magnetization and c axis polarization is not symmetry allowed.[50] There have been a few explanations for the increase of ε in the intermediate phase. Lorenz *et al.*[51] proposed that the magnetoelectric coupling between polarization along c axis and magnetization is enabled by the Mn spin canting along the c axis. To the contrary, Fiebig *et al.*[52] proposed magnetoelectric coupling based on the formation of spin-rotation domain walls. For example, the formation of a Néel domain wall at the reorientation transition can explain the observed dielectric anomaly since in a Néel domain wall, spins rotate parallel to axis of the wall and the domain wall configuration is very similar to a spiral magnetic structure with the rotation of the magnetic moment ($\mathbf{e}_3$) perpendicular to the propagation vector, $\mathbf{Q}$. Therefore, a polarization which depends on the total rotation angle of the spins across the domain wall can be induced according to Eq. 1.4.

Lottermoser *et al.*[9] also proposed that ferromagnetism can be induced by applying an external electric field for $HoMnO_3$ below $T = 76$ K, implying a robust coupling between ferroelectric polarization and magnetization. Specifically, Lottermoser *et al.* claimed that the antiferromagnetic or paramagnetic state of Ho^{3+} can be changed to a ferromagnetic state while Mn^{3+} moments remain antiferromagnetic, based on their second harmonic generation and optical Faraday rotation experiments. They also claimed that ferromagnetism can be reversibly switched on and off by the application of electric field. Therefore, $HoMnO_3$ and related hexagonal multiferroics represent a promising class of magnetoelectric multiferroic compound for potential technological applications.

1.5 An Overview of the Thesis

Hexagonal RMnO$_3$ compounds are an important class of mutiferroics for several reasons. First, the ferroelectric polarization of this class is large and comparable to conventional ferroelectrics and, therefore, show promise for practical applications. By comparison, for the magnetically driven ferroelectrics, the ferroelectric polarization is approximately two orders of magnitude smaller and they have to be poled frequently to maintain a single ferroelectric domain state. Second, the observed coupling between magnetism and ferroelectricity in zero

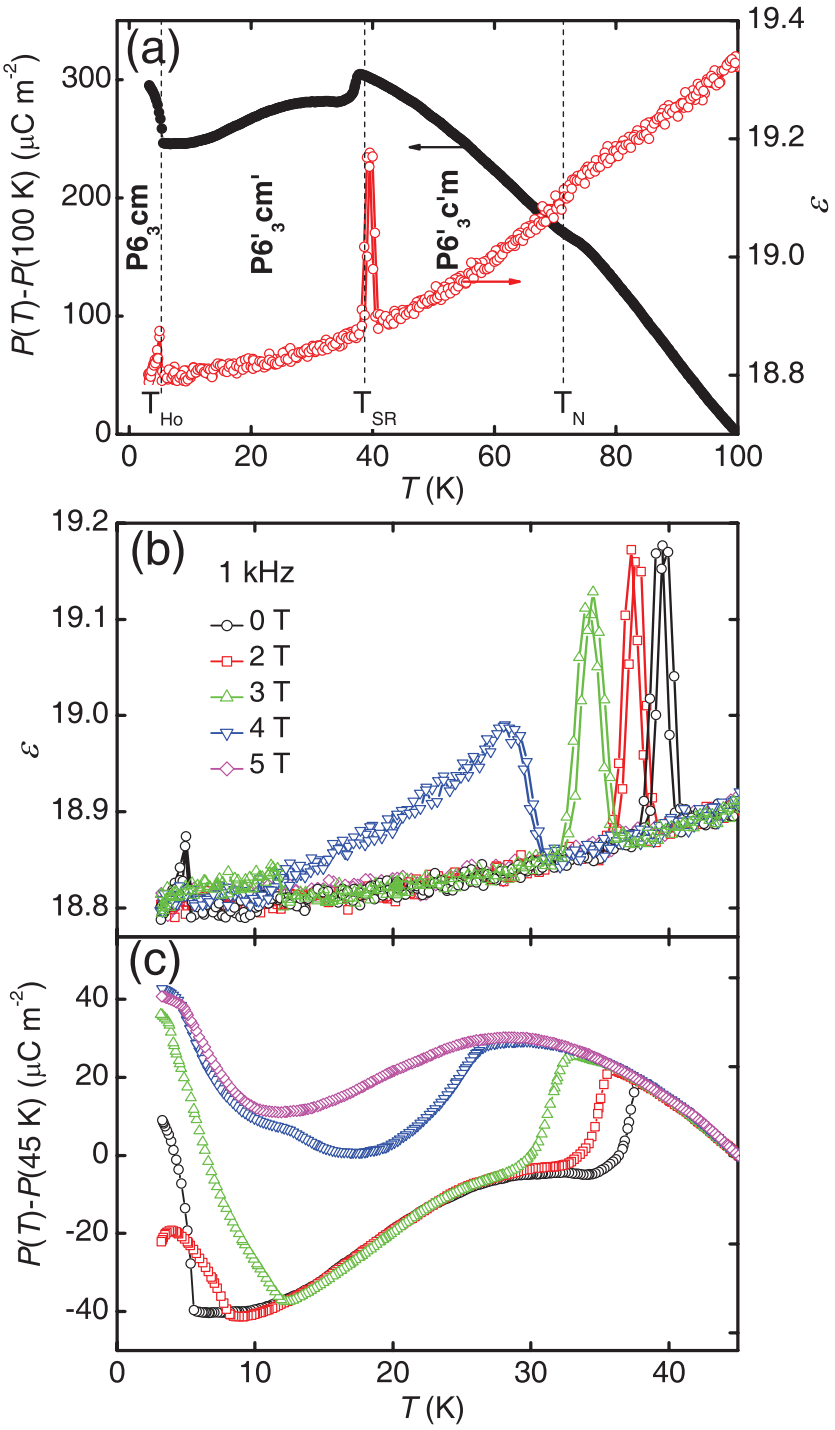

Figure 1.16 (a) Temperature (T) dependence of the polarization P (solid circle) and dielectric constant ε (open circle) for $HoMnO_3$ in zero magnetic field H. Vertical dashed lines indicate magnetic phase boundaries. (b) T dependence of ε along the c axis in various H applied along the c axis. (c) T dependence of P along the c axis in H. After Ref. [43]

field is large, offering the possibility for control of electric polarization by external magnetic fields and magnetism by external electric fields. Indeed, the proposal by Lottermoser *et al.*[9] that antiferromagnetism/paramagnetism of Ho^{3+} in $HoMnO_3$ can be transformed to ferromagnetism in an applied electric field, implying a large magnetoelectric coupling was an important stimulus for this work. Since the determination of the magnetic structure and corresponding symmetry in the $R\mathrm{MnO}_3$ compounds is the first and most important step in understanding any coupling between ferroelectricity and magnetism, we have undertaken a determination of the magnetic structures of the rare-earth moments in hexagonal $R\mathrm{MnO}_3$ compounds.

Despite numerous studies in the past,[30, 41, 44, 45, 46, 47, 48] the magnetic structures of Ho^{3+} reported by different groups are contradictory. The controversies present in the literature are mainly due to the lack of sensitivity of the previously used techniques to rare-earth magnetic ordering. The conventional route for magnetic structure determination is neutron scattering. However, neutron scattering in this instance proved to be difficult in the following sense. In neutron scattering experiments on a multicomponent magnetic system, a magnetic structure must first be assumed and the ordered moments of the two sublattices are then extracted from the intensities of a number of reflections. In the case of $HoMnO_3$, the neutron magnetic signal is dominated by Mn^{3+} moments since the Mn^{3+} carries a fully ordered moment compared to small ordered component of Ho^{3+} moments and the Ho^{3+} contribution must be determined from a careful fitting process together with the Mn^{3+} contribution. We have employed x-ray resonant magnetic scattering (XRMS) to circumvent the difficulties observed in the previous neutron scattering experiments. Since XRMS experiments are performed at the absorption edge of the element of interest, one can focus on one magnetic contribution at a time. Due to this elemental specificity a direct determination of the magnetic order of the rare-earth component is possible. In this sense, an XRMS study of $R\mathrm{MnO}_3$ compounds is more reliable in determining the magnetic structure of R^{3+} and the magnetic order parameter.

We have determined uniquely the magnetic structure of Ho^{3+} moments through a detail analysis of the XRMS data and thereby resolved the above-mentioned controversies. Specifically, we found that the Ho^{3+} moments order antiferromagnetically along the **c** axis below 40 K

(ITP, the intermediate temperature phase) and the antiferromagnetic structure changes below 4.5 K (LTP, the low temperature magnetic phase). We have also found that the temperature dependence of the magnetic moments in the temperature range 4.5 K$\leq T \leq$40 K is unusual, but can be modeled assuming an exchange interaction between Ho^{3+} and Mn^{3+} and a splitting of the ground state quasi-doublet crystal electric field levels of Ho^{3+} by this exchange field. Modeling the temperature dependence for Ho^{3+} provides the first qualitative understanding of the nature of Ho^{3+} ordering in this temperature range. For a better understanding of the magnetic ordering of rare-earths in the RMnO$_3$ compounds, we have also determined the magnetic ordering of other hexagonal multiferroic compounds including DyMnO$_3$ and ErMnO$_3$. We found the same magnetic structure for Dy^{3+} and very similar temperature dependence of magnetic moments as that for Ho^{3+} in the temperature range 8 K$\leq T \leq$68 K (ITP). However, Dy^{3+} moments order ferrimagnetically below 8 K (LTP) which is different than for Ho^{3+}. For ErMnO$_3$, we conclude that Er^{3+} moments order only below 3 K with the same magnetic structure as that of Dy^{3+} in the LTP.

After determining the zero-field magnetic structure of these compounds, we focused on determining the magnetic structure in an applied electric field. We approached this problem in three ways. First, we measured changes in bulk magnetization by conventional magnetization measurement techniques such as SQUID measurements. Second, we probed element specific changes in magnetization by XRMS and the related x-ray magnetic circular dichroism (XMCD) technique. Specifically, we probed changes in antiferromagnetic structure by XRMS and searched for a ferromagnetic component of Ho^{3+} by XMCD. We were unable to find any ferromagnetic component of Ho^{3+} in an applied electric field in contrast to the proposal by Lottermoser *et al.*[9]

The organization of the dissertation is as follows. The following chapter introduces XRMS and XMCD as tools to study magnetic structure. In this chapter, the procedure for determining magnetic structure by an XRMS experiment is detailed. Specifically, the role of symmetry in determining possible magnetic structures and calculation of magnetic structure factors (related to magnetic intensity) for all of the possible structures is discussed. Chapter 3 is concerned

with the zero-field magnetic structure of rare-earth moments as well as an understanding of the magnetic structures in terms of superexchange interactions. Chapter 4 deals with the magnetic order of rare-earth moments in an applied electric field. The last chapter summarizes the results of this study, and provides an outlook for future studies. A summary of the main results of the magnetic structure of $HoMnO_3$ in zero and applied electric field has been published in Phys. Rev. Lett.[53] The magnetic structure of the Dy^{3+} moments has been published in Phys. Rev B. [40]

CHAPTER 2. OVERVIEW OF X-RAY SCATTERING PROCESSES

Investigations of the structure and dynamics of materials have been an important and essential endeavor in condensed matter physics since the early 20^{th} century. Both neutron and x-ray scattering techniques have been used extensively to study the crystallographic structure of materials and provide complementary views of structure. For example, neutron scattering has traditionally been the standard tool for studies of magnetic structure and the dynamics of condensed matter systems. X-ray diffraction has largely been applied to detailed crystallographic structure determination. The principle interaction that makes structure determination possible for x-rays is the Coulomb interaction between x-rays and the electronic distribution which gives rise to driven harmonic oscillation of the electrons, and the emission of electric dipole radiation. This is the classical *Thomson scattering* process.

At x-ray absorption edges photoelectric absorption occurs and electrons are promoted from core levels into empty states above the Fermi level. Photons that take part in the photoelectric absorption are lost for the scattering experiment. However, the incident photons can also give rise to virtual transitions between core levels and states above the Fermi level that relax back to the core states with the emission of x-rays with the same energy as the initial beam. For charge scattering, this is known as *anomalous charge scattering* which yields additional terms in the x-ray scattering form factor that can be used to enhance the scattering contrast between neighboring elements. Anomalous scattering is also sensitive to the anisotropy of local environment, such as the arrangement of orbitals and orbital order. In addition to charge scattering, x-rays interact with the magnetic moment of the system. Indeed, the *magnetic scattering* of x-rays from electrons in molecules and solids is well documented in theory[54] and was observed experimentally by de Bergevin and Brunel in 1970's with a commercial x-ray

tube.[55] de Bergevin and Brunel also presented a classical picture of the interaction between x-rays with electrons and magnetic moments[56] illustrated in Fig. 2.1. Unfortunately, from a practical point of view, the x-ray scattering cross-sections from electron spins are reduced by approximately six orders of magnitude compared to normal charge scattering and, therefore, using x-ray magnetic scattering to study magnetism was largely impractical in 1970's.

The situation changed in 1990's when Gibbs and coworkers successfully observed magnetic scattering from Ho metal due to the dramatic increase of photon flux available from synchrotron radiation.[57] The increased photon flux compensates for the weakness of the magnetic scattering signal. The polarization properties and tunability of the x-ray energy at a synchrotron source provides additional advantages for magnetic x-ray scattering. As will be discussed in the next section when x-ray energies are tuned through the absorption edges of an element of interest there is a resonant enhancement of the scattering signal now known as *x-ray resonant magnetic scattering.*[58] Away from the resonance condition, the magnetic scattering signal is known as *non-resonant x-ray magnetic scattering.* All of the above processes have been reviewed and described in detail in several texts.[59] In the following, we will concentrate mainly on the descriptions of x-ray resonant magnetic scattering and x-ray magnetic circular dichroism.

2.1 X-Ray Resonant Magnetic Scattering

In x-ray resonant magnetic scattering, the x-ray energy is tuned through the absorption edge of the element of interest, an electron is photo-excited from the core levels to the unoccupied states above the Fermi energy, and the de-excitation to the core-level yields an elastically scattered photon. In an ordered magnetic state, this process is sensitive to the magnetization density because of exchange splitting in the bands.[60] The process of x-ray resonant magnetic scattering (XRMS) is shown schematically in Fig. 2.2. The first resonant magnetic scattering measurement in an antiferromagnetic material, Ho metal, was observed by Gibbs *et al.* and illustrated in Fig. 2.3.[61]

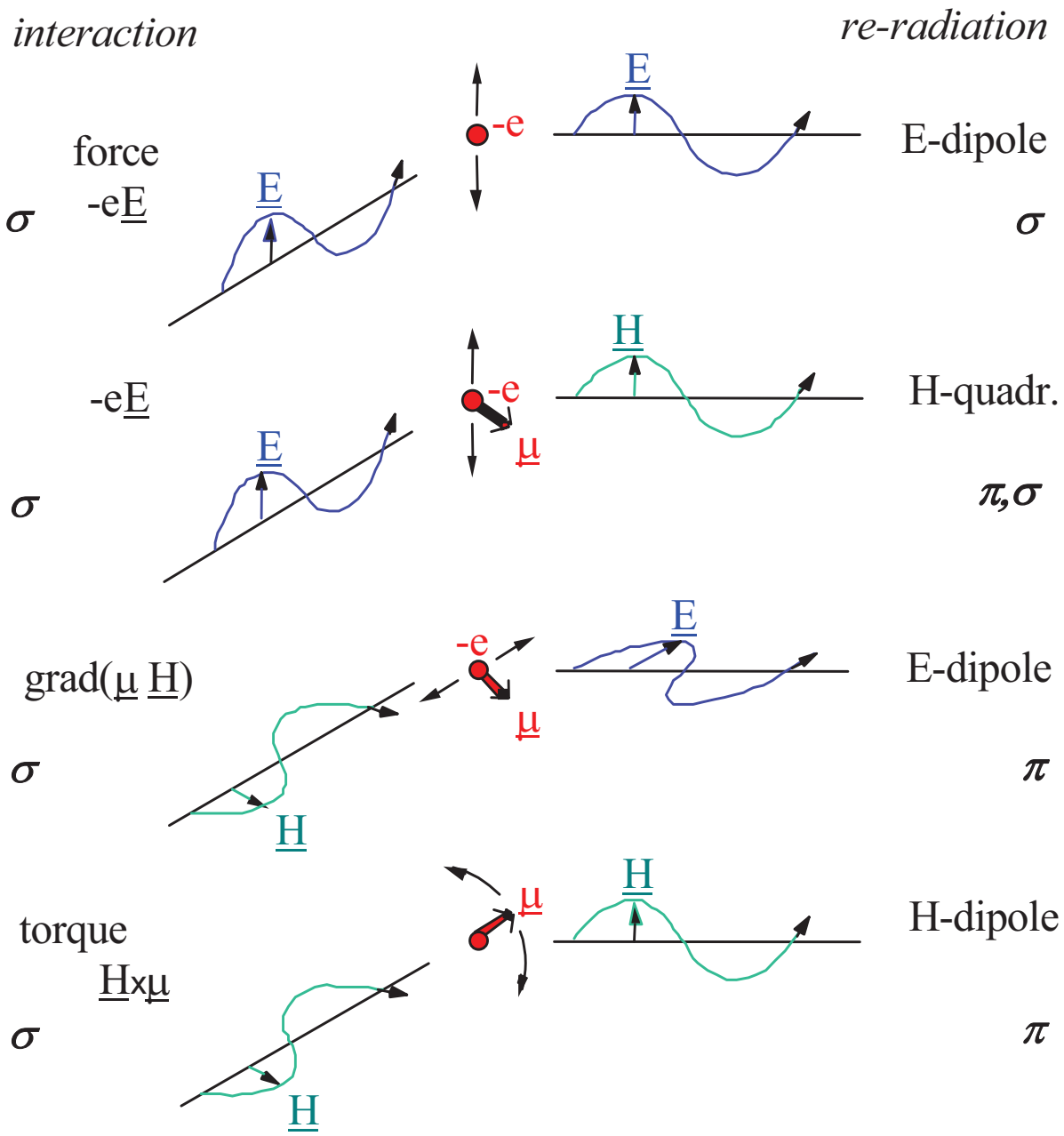

Figure 2.1 Illustration of the processes leading to scattering of x-rays by the charge (top) and the spin moment (bottom three) of the electron in a classical picture. After Refs. [56, 66]

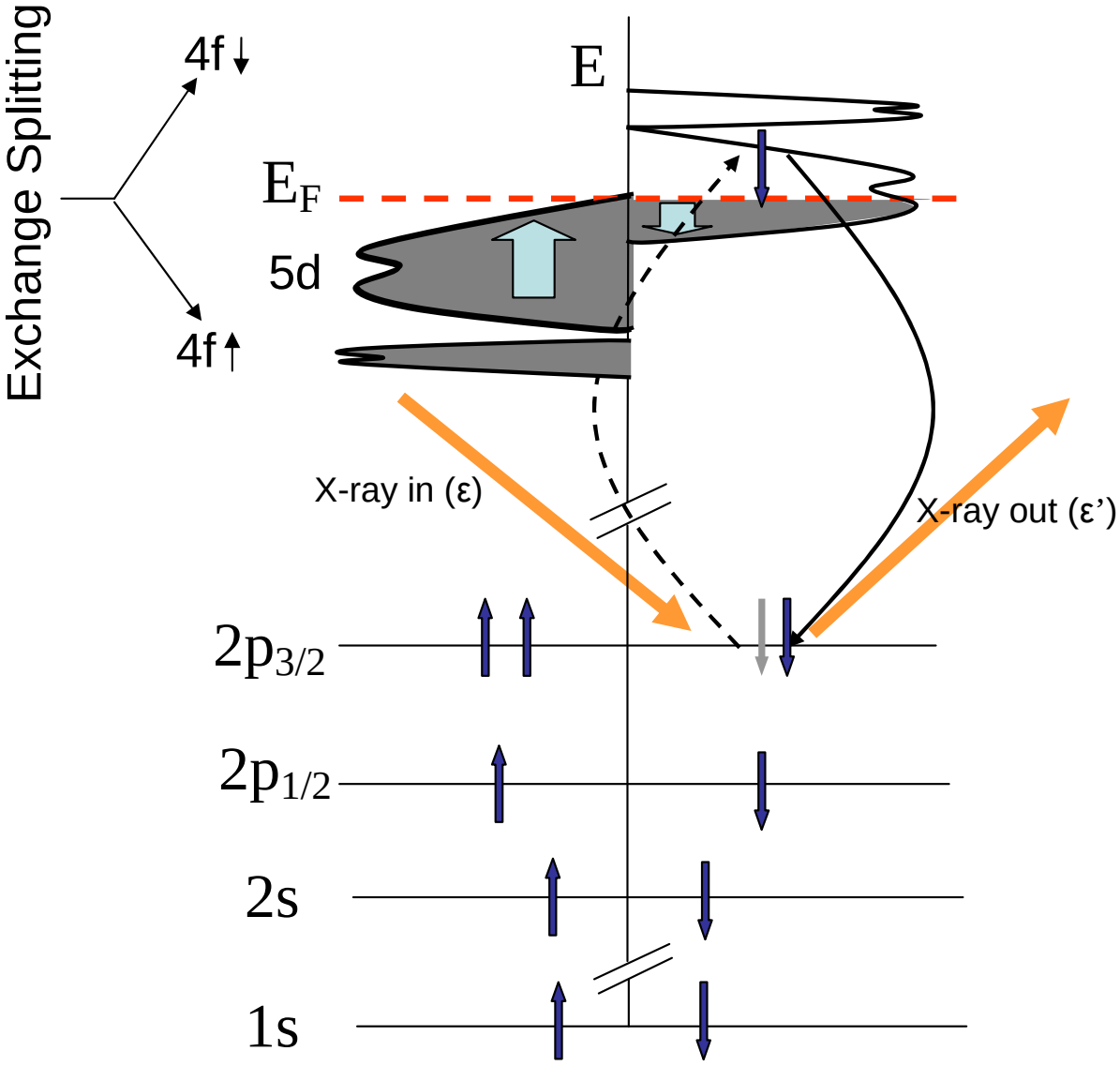

Figure 2.2 Schematic illustration of the second order perturbation process leading to XRMS in the case of a lanthanide metal. An electron being photo-excited from the core level to the empty states above the Fermi energy E_F. The subsequent decay of the electron to the core level gives rise to an elastically scattered photon.

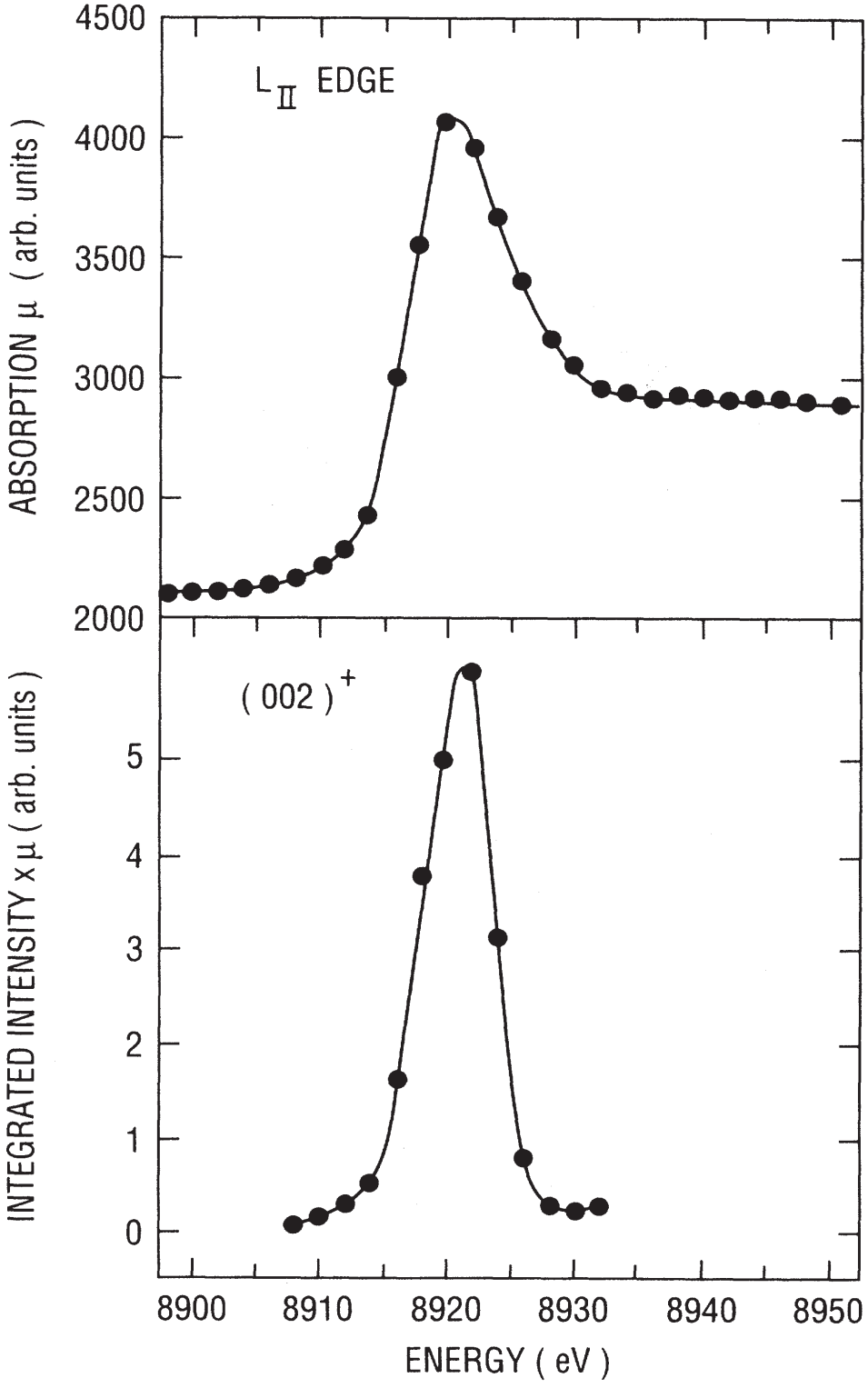

Figure 2.3 Top: The photoelectric absorption measured through a 5μm Ho film as the x-ray energy is tuned through the Ho L_{II} edge. Bottom: Integrated intensity of the (0 0 2+τ) reflection of Ho metal plotted vs incident x-ray energy. After Ref. [58]

2.1.1 The Cross Section for X-ray Resonant Magnetic Scattering

The calculation of the x-ray scattering cross-section from a quasi-relativistic Hamiltonian for a electron in a quantized electromagnetic field using second order perturbation theory was done by Blume[62] and Blume and Gibbs[63], and was later presented in a simplified form by Hill and McMorrow[64] in the coordinate system convenient for XRMS experiments. We start with the Hamiltonian for electrons in a quantized electromagnetic field:

$$\begin{aligned} H =& \sum_j \frac{1}{2m}\{\vec{P}_j - \frac{e}{c}\vec{A}(\vec{r}_{ij})\}^2 + \sum_{ij} V(\vec{r}_{ij}) - \frac{e\hbar}{2mc}\sum_j \vec{s}_j \cdot \nabla_j \times \vec{A}(\vec{r}_j) \\ & - \frac{e\hbar}{2(mc)^2}\sum_j \vec{s}_j \cdot \vec{E}(\vec{r}_j) \times \{\vec{p}_j - \frac{e}{c}\vec{A}(\vec{r}_j)\} + \sum_{\vec{k}\lambda} \hbar\omega_{\vec{k}}\{c^\dagger(\vec{k}\lambda)c(\vec{k}\lambda) + \frac{1}{2}\} \end{aligned} \tag{2.1}$$

Here, the first term corresponds to the kinetic energy of the electrons in the electromagnetic field, represented by the vector potential $\vec{\mathrm{A}}(\vec{\mathrm{r}})$. The second term corresponds to the Coulomb interaction between electrons, the third term corresponds to the Zeeman energy, $-\vec{\mu}\cdot\vec{H}$, of the electrons with spin $\vec{\mathrm{s}}_j$, the fourth term is the spin-orbit coupling in the initial or final states and the last term is the self energy of the electromagnetic field.

The vector potential $\vec{\mathrm{A}}(\vec{\mathrm{r}})$ is linear in photon creation and annihilation operator $c^\dagger(\vec{k}\lambda)$ and $c(\vec{k}\lambda)$, and can be expanded in plane wave form as:

$$\vec{A}(\vec{r}) = \sum_{\vec{q}\sigma}(\frac{2\pi\hbar c^2}{V\omega_q})^{\frac{1}{2}} \times [\vec{\epsilon}(\vec{q}\sigma)c(\vec{q}\sigma)e^{i\vec{q}\cdot\vec{r}} + \vec{\epsilon}^{\star}(\vec{q}\sigma)c^\dagger(\vec{q}\sigma)e^{-i\vec{q}\cdot\vec{r}}] \tag{2.2}$$

Here V is the quantization volume and $\epsilon(\vec{q}\sigma)$ is the unit polarization vector corresponding to a wave vector $\vec{q}$ and polarization state σ. The index $\sigma(=1,2)$ labels two polarizations for each wave vector $\vec{q}$. Since $\vec{\mathrm{A}}(\vec{\mathrm{r}})$ is linear in photon creation and annihilation operator, $c^\dagger(\vec{k}\lambda)$ and $c(\vec{k}\lambda)$, scattering occurs in second order for terms linear in $\vec{\mathrm{A}}$ and in first order for quadratic terms. For the spin orbit term in Eq. 2.1, $\vec{E}$ can be written in terms of scalar potential ϕ and the vector potential $\vec{A}$ as:

$$\vec{E} = -\nabla\phi - \frac{1}{c}\dot{\vec{A}} \tag{2.3}$$

After substituting $\vec{A}$ and $\vec{E}$ in Eq. 2.1, the Hamiltonian in Eq. 2.1 can be re-written as the sum of three terms:[62]

$$H = H_0 + H_R + H' \tag{2.4}$$

Where H_0 contains only the degrees of freedom for the electron system, H_R is the Hamiltonian for the quantized electromagnetic field and $H^{'}$ corresponds to the interaction between the electron and the radiation field. Scattering cross sections are calculated by assuming the solid is in a quantum state $|a\rangle$ which is an eigenstate of H_0 with energy E_0 and there is a single photon present. We then calculate the probability of a transition induced by the interaction term $H^{'}$ to a state $|b\rangle$, with photon $\vec{k}^{'}\lambda^{'}$. The transition probability (Ω) per unit time can be calculated using "Fermi's golden rule" up to second order:

$$\begin{aligned} \Omega &= \frac{2\pi}{\hbar}|\langle f|H^{'}|i\rangle + \sum_n \frac{\langle f|H^{'}|n\rangle\langle n|H^{'}|i\rangle}{E_i - E_f}|^2 \times \delta(E_i - E_f) \\ |i\rangle &= |a;\vec{k}\lambda\rangle;\ |f\rangle = |b;\vec{k}^{'}\lambda^{'}\rangle \end{aligned} \tag{2.5}$$

While the detailed derivation of the scattering cross section is given in Ref. [62], we will outline here the final results. For coherent elastic scattering, ($|a\rangle = |b\rangle$), and the amplitude can be written as a sum over the following terms:[64]

$$f = f_0 + f^{'} + if^{''} + f_{spin} \tag{2.6}$$

Here, $f_0 \propto Zr_0$ is the Thompson charge scattering amplitude and f_{spin} is the non-resonant spin-dependent magnetic scattering amplitude. Far from resonance, $f^{'}$ and $f^{''}$ contribute terms proportional to the orbital and spin angular momentum. At resonance both electric and magnetic multipole transitions contribute through the terms $f^{'}$ and $f^{''}$. However, the electric dipole and quadrupole transitions are dominant with respect to magnetic multipole transitions by a factor of $\hbar\omega/mc^2$ ($\sim$ 60 for typical x-ray edges) and so the only electric multipole transitions will be considered here.

For the electric 2^L-pole resonance in a magnetic ion, the resonant contribution to the coherent scattering amplitude can be written as[60]

$$f^e_{EL}(\omega) = \frac{4\pi}{k} f_D \sum_{M=-L}^{L} [\hat{\epsilon}^{'\star} \cdot Y^{(e)}_{LM}(\hat{k}^{'}) Y^{(e)\star}_{LM}(\hat{k}) \cdot \hat{\epsilon}] F^e_{EL}(\omega) \tag{2.7}$$

Where $\hat{\epsilon}$ and $\hat{\epsilon}^{'\star}$ are the incident and scattered polarization vectors, and $\hat{k}$ and $\hat{k}^{'}$ are the incident and scattered wave vectors, respectively. $Y^{(e)}_{LM}(\hat{k})$ are the vector spherical harmonics

and f_D is the Debye-Waller factor. The strength of the resonance is determined by the factor $F^e_{EL}(\omega)$, which is, to 0^{th} order, determined by atomic properties:

$$F^e_{EL}(\omega) = \sum_{a,n} \frac{P_a P_a(n) \Gamma_x(aMn; EL)}{2(E_n - E_a - \hbar\omega - i\Gamma/2)} \tag{2.8}$$

Here, $|n\rangle$ is the excited state of the ion and $|a\rangle$ the initial state. P_a is the probability of the ion existing in the initial state $|a\rangle$ and $P_a(n)$ is the probability for a transition from $|a\rangle$ to an excited state $|n\rangle$. It is determined by overlap integrals between the two states $|a\rangle$ and $|n\rangle$. Γ_x and Γ are the partial line widths of the excited state due to a pure electric 2^L-pole (EL) radiative decay and due to all processes, both radiative and non-radiative (including, for example, Auger decay), respectively. These electric multipole (predominantly dipole and quadrupole) transitions involve the virtual photo-excitation of an electron from a core level to the unoccupied states above the Fermi energy with a subsequent de-excitation to the core-levels yielding an elastically scattered photon. These processes become sensitive to the magnetic state in exchange split bands due to the difference in occupation of minority and majority bands as illustrated schematically in Fig. 2.2. Due to the resonant denominator in Eq. 2.8, enhancements occur at the absorption edges of the magnetic elements (e.g. when, E_n-E_a=$\hbar\omega$). The strengths of these enhancements for XRMS depend mainly on three factors as discussed by Hannon *et al.*[60] and shown by XRMS experiments on a series of rare-earth intermetallic compounds ($R\text{Ni}_2\text{Ge}_2$, R= rare-earths) by Kim *et al.*[65]:

1. The magnitude of the transition matrix element. Dipole transitions between states $|a\rangle$ and $|n\rangle$ differing in orbital angular momentum quantum number by $\Delta\text{L} = 1$ are generally stronger than quadrupolar transitions with $\Delta\text{L} = 2$. A large overlap of the wave functions $|a\rangle$ and $|n\rangle$ favors large transition matrix elements. In contrast, transitions from "s" core levels to "p" or "d" excited states do not show large resonance enhancements due to the small overlap of the wave functions.

2. The difference in the density of empty states above the Fermi level for minority and majority spin states. To give an example: in lanthanide metals, the $5d$ bands are spin polarized due to the magnetic $4f$ states. However, the exchange splitting in the $5d$ is

Table 2.1 Magnitude of the resonance enhancement for XRMS for some elements relevant for magnetism. Only order of magnitude estimates are given with "weak" corresponding to a factor of about "10^0", "medium" to about "10^2" and "strong" to "$>10^3$" compared to the non-resonant magnetic scattering. After Ref. [66]

Elements	Edge	Transition	Energy Range (keV)	Resonance Strength	Comment
$3d$	K	$1s \rightarrow 4p$	5-9	Weak	Small overlap
$3d$	L_I	$2s \rightarrow 3d$	0.5-1.2	Weak	Small overlap
$3d$	L_{II}, L_{III}	$2p \rightarrow 3d$	0.4-1.0	Strong	Dipolar, Large overlap, high spin polarization of $3d$
$4f$	K	$1s \rightarrow 4p$	40-63	Weak	Small Overlap
$4f$	L_I	$2s \rightarrow 5d$	6.5-11.0	Weak	Small overlap
$4f$	L_{II}, L_{III}	$2p \rightarrow 5d$, $2p \rightarrow 4f$	6.0-10.0	Medium	Dipolar and quadrupolar
$4f$	M_I	$3s \rightarrow 5p$	1.4-2.5	Weak	Small overlap
$4f$	M_{II}, M_{III}	$3p \rightarrow 5d$, $3p \rightarrow 4f$	1.3-2.2	Medium to strong	Dipolar, quadrupolar
$4f$	M_{IV}, M_V	$3d \rightarrow 4f$	0.9-1.6	Strong	Dipolar, large overlap, high spin polarization of $4f$
$5f$	M_{IV}, M_{II}	$3d \rightarrow 5f$	3.3-3.9	Strong	Dipolar, large overlap, high spin polarization of $5f$

much weaker as compared to the $4f$ states and dipolar transitions $2p \rightarrow 5d$ are sometimes not much stronger than quadrupolar transitions $2p \rightarrow 5f$.

3. The strength of the spin-orbit coupling in the ground and excited states. It is this coupling that provides electric multipole transitions with sensitivity to the spin magnetism.

Using the above-mentioned factors, we can qualitatively categorize the possible transitions according to the magnitude of the resonance enhancement, as listed in Table. 2.1.[66] Here we define the term "resonant enhancement" as the ratio between the intensity of magnetic Bragg peaks at the maximum of the resonance relative to the intensity for non-resonant magnetic

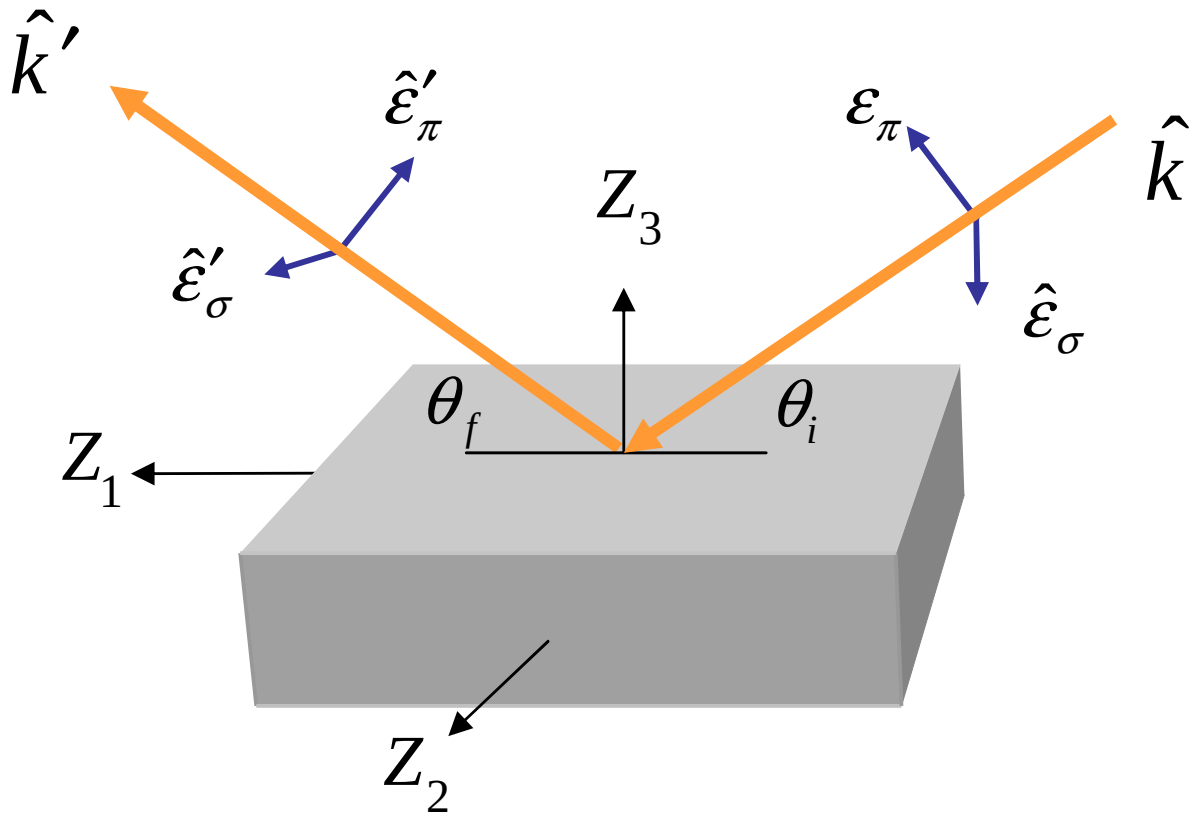

Figure 2.4 The coordinate system used for the polarization dependence of the resonant scattering amplitudes described in the text. $\hat{k}$ and $\hat{k}'$ are the incident and scattered wave vectors and θ_i and θ_f is the incident and outgoing angle with respect to the sample surface . $\hat{\epsilon}_\sigma$ ($\hat{\epsilon}'_\sigma$) and $\hat{\epsilon}_\pi$ ($\hat{\epsilon}'_\pi$) are the components of the polarization perpendicular and parallel to the scattering plane for incident (scattered) x-rays.

scattering.

2.1.2 Polarization Properties

One of the strengths of resonant magnetic scattering is that the polarization state of the scattered x-rays can be modified with respect to that of the incident beam. Therefore, by analyzing the polarization of scattered x-rays, it is possible to discriminate between charge and magnetic scattering. Furthermore, by analyzing the intensity of scattered x-rays in different polarization channels, the spatial components of the ordered magnetic moment can be

obtained.[67, 68] Therefore, in the following sections explicit relationship between the amplitude of scattered x-rays and incident x-rays will be shown according to Ref. [64].

2.1.2.1 Electric Dipole Transitions (E1)

For rare-earth L-edges, electric dipole transitions usually dominate the resonant magnetic cross section and are the simplest to calculate. An example of such a transition is the $2p_{3/2} \rightarrow 5d_{1/2}$ transition of Ho, which occurs at the L_{III} absorption edge. At this transition, the vector spherical harmonics can be written, for L = 1, M = ±1:

$$[\hat{\epsilon}'^{\star} \cdot Y^{(e)}_{1\pm1}(\hat{k}')Y^{(e)\star}_{1\pm1}(\hat{k}) \cdot \hat{\epsilon}] = (3/16\pi)[\hat{\epsilon}' \cdot \hat{\epsilon} \mp i(\hat{\epsilon}' \times \hat{\epsilon}) \cdot \hat{z}_n - (\hat{\epsilon}' \cdot \hat{z}_n)(\hat{\epsilon} \cdot \hat{z}_n)] \tag{2.9}$$

Similarly, for L = 1, M = 0

$$[\hat{\epsilon}'^{\star} \cdot Y^{(e)}_{10}(\hat{k}')Y^{(e)\star}_{10}(\hat{k}) \cdot \hat{\epsilon}] = (3/8\pi)[(\hat{\epsilon}' \cdot \hat{z}_n)(\hat{\epsilon} \cdot \hat{z}_n)] \tag{2.10}$$

where $\hat{z}_n$ is a unit vector in the direction of the magnetic moment of the nth ion. Thus,

$$f^{XRMS}_{nE1} = [(\hat{\epsilon}' \cdot \hat{\epsilon})F^{(0)} - i(\hat{\epsilon}' \cdot \times\hat{\epsilon}) \cdot F^{(1)} + (\hat{\epsilon}' \cdot \hat{z}_n)(\hat{\epsilon} \cdot \hat{z}_n)F^{(2)}] \tag{2.11}$$

where $F^{(i)}$'s are the terms containing dipole matrix elements which have been evaluated by Hamrick for several rare-earths.[69] The first term of Eq. 2.11 contributes to the charge Bragg peak as it does not contain any dependence on the magnetic moment. The other two terms depend on the magnetic moment. All terms in Eq. 2.11 can be represented in 2×2 matrix form with polarization states chosen either parallel and perpendicular to the scattering plane and resolving each of the vectors $\hat{k}$, $\hat{k}'$ and $\hat{z}_n$ into their components along the three orthogonal axes defined with respect to the diffraction plane shown in Fig. 2.4.

The amplitude of scattered x-rays, A'_σ and A'_π, can be written in terms of the amplitude of incoming x-rays, A_σ and A_π, the components of the magnetic moments along the three

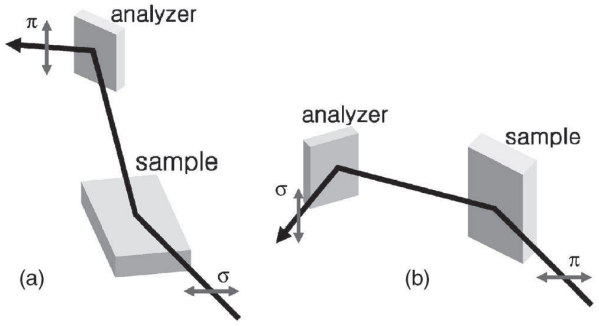

Figure 2.5 Experimental realization of different polarization channels for the (a) $\sigma \rightarrow \pi$ and (b) $\pi \rightarrow \sigma$ scattering geometries. After Ref. [70]

orthogonal directions, and the Bragg angle θ as follows:

$$\begin{aligned}\begin{bmatrix} A'_\sigma \\ A'_\pi \end{bmatrix} &= F^{(0)} \begin{pmatrix} 1 & 0 \\ 0 & \cos 2\theta \end{pmatrix} \begin{bmatrix} A_\sigma \\ A_\pi \end{bmatrix} \\ &- iF^{(1)} \begin{pmatrix} 0 & z_1 \cos\theta + z_3 \sin\theta \\ z_3 \sin\theta - z_1 \cos\theta & -z_2 \sin 2\theta \end{pmatrix} \begin{bmatrix} A_\sigma \\ A_\pi \end{bmatrix} \\ &+ F^{(2)} \begin{pmatrix} z_2^2 & -z_2(z_1 \sin\theta - z_3 \cos\theta) \\ z_2(z_1 \sin\theta + z_3 \cos\theta) & -\cos^2\theta(z_1^2 \tan^2\theta + z_3^2) \end{pmatrix} \begin{bmatrix} A_\sigma \\ A_\pi \end{bmatrix}\end{aligned} \tag{2.12}$$

The above matrix equation is sum of three sub-matrices: The first one contributes to the charge Bragg peak. The second and third contribute to the magnetic Bragg peak. A few points to note for the magnetic contribution:

1. The second term is linear in the components of the magnetic moment and therefore, mainly responsible for producing peaks at the magnetic wavevector, $\vec{\tau}$. For example, in an antiferromagnet with wavevector, $\vec{\tau}$, the linear term produces first harmonic satellite peaks. The third term, which is quadratic in the components of a magnetic moment produces second harmonic satellites as well as contributes to the charge Bragg peaks.[1] For a ferromagnetic material both the second and third term contribute to the positions of allowed charge reflections.

[1]for a commensurate antiferromagnet with propagation vector $\vec{\tau}$=0, it can produce intensity at the charge forbidden reciprocal lattice points.

2. Synchrotron radiation is linearly polarized in the plane of storage ring. Therefore, all combinations of polarization channels are accessible by suitably selecting the scattering plane (see Fig. 2.5 for experimental geometries[70]) and, hence, different components of the ordered magnetic moment can be probed. For example, scattering in the $\sigma \rightarrow \pi^{'}$ channel is sensitive to the component of magnetic moment in the scattering plane (in the Fig. 2.4, z_1 and z_3) and $\pi \rightarrow \pi^{'}$ channel is sensitive to the components of a magnetic moment out of the scattering plane (z_2 in Fig. 2.4).

3. The scattering amplitude depends on the Bragg angle, and therefore by analyzing the magnetic peak intensities as a function of scattering angle, a specific magnetic model can be proved or disproved.

2.1.2.2 Electric Quadrupole Transitions (E2)

The intensity of the scattered x-rays for quadrupole resonances can be calculated in a similar manner and is detailed by Hill and McMorrow in Ref. [64]. Here, we will write the final form in terms of components of magnetic moments:

$$\begin{aligned}
\begin{bmatrix} A_\sigma^{'} \\ A_\pi^{'} \end{bmatrix} &= F_{E2}^{(0)} \begin{bmatrix} c_2 & 0 \\ 0 & c_2^2 \end{bmatrix} \begin{bmatrix} A_\sigma \\ A_\pi \end{bmatrix} \\
&+ ic_2 F_{E2}^{(1)} \begin{bmatrix} z_2 t_2 & -z_1 c - z_3 s \\ -z_3 s + z_1 c & 2 z_2 s_2 \end{bmatrix} \begin{bmatrix} A_\sigma \\ A_\pi \end{bmatrix} \\
&+ (F_{E2}^{(2)} - F_{E2}^{(0)}) \begin{bmatrix} z_1^2 c^2 + z_2^2 c^2 - z_3^2 s^2 & -z_1 z_2 s c_2 + z_2 z_3 c c_2 \\ z_1 z_2 s c_2 + z_2 z_3 c c_2 & c_2^2 (z_1^2 + z_3^2) \end{bmatrix} \begin{bmatrix} A_\sigma \\ A_\pi \end{bmatrix} \\
&+ s_2 F_{E(2)}^{(2)} \begin{bmatrix} 0 & -z_1 z_2 c - z_2 z_3 s \\ z_1 z_2 c - z_2 z_3 s & -s_2 (z_1^2 + z_3^2) \end{bmatrix} \begin{bmatrix} A_\sigma \\ A_\pi \end{bmatrix}
\end{aligned}$$

$$
\begin{aligned}
&+s_2F^{(0)}_{E(0)}\begin{bmatrix} 0 & z_1z_2c+z_2z_3s \\ -z_1z_2c+z_2z_3s & -z_2^2s_2 \end{bmatrix}\begin{bmatrix} A_\sigma \\ A_\pi \end{bmatrix} \\
&+i(F^{(3)}_{E_2}-F^{(1)}_{E_2})\begin{bmatrix} -z_2^3s_2 & z_1^3c^3+z_1^2z_3sc^2-z_1z_3^2s^2c \\ & +z_1z_2^2s_2s-z_3z_2^2s_2c-z_3^3s^3 \\ -z_1^3c^3+z_1^2z_3sc^2+z_1z_3^2s^2c & -z_2c_2s_2(z_1^2+z_3^2) \\ -z_1z_2^2s_2s-z_3z_2^2s_2c-z_3^3s^3 & \end{bmatrix}\begin{bmatrix} A_\sigma \\ \\ \\ \\ A_\pi \end{bmatrix} \\
&-iF^{(3)}_{E_2}\begin{bmatrix} & -z_1z_2^2cc_2+z_1^2z_3(s_2c+s_3^3) \\ z_2(z_1^2+z_3^2)s_2 & -z_2^2z_3c_2s-z_1z_3^2(c_3^3+s_2s) \\ & -z_1^3cs^2+z_3^3c^2s \\ +z_1z_2^2cc_2+z_1^2z_3(s_2c+s^3)-z_2^2z_3c_2s & \\ +z_1z_3^2(c_3+s_2s)+z_1^3cs^2+z_3^3c^2s & -z_2c_2s_2(z_1^2+z_3^2) \end{bmatrix}\begin{bmatrix} A_\sigma \\ \\ \\ \\ A_\pi \end{bmatrix} \\
&+F^{(4)}_{E_2}\begin{bmatrix} z_1^2z_2^2c^2-z_2^2z_3^2s_2^2 & -z_1z_2z_3^2s^3-z_1^3z_2sc^2 \\ & -z_2z_3^3cs_2+z_1^2z_2z_3c^3 \\ -z_1z_2z_3^2s^3+z_1^3z_2sc^2 & z_1^2z_3^2(c^4+s^4) \\ -z_2z_3^3cs_2+z_1^2z_2z_3c^3 & -(z_1^4+z_3^4)s^2c^2 \end{bmatrix}\begin{bmatrix} A_\sigma \\ \\ \\ \\ A_\pi \end{bmatrix}
\end{aligned}
\tag{2.13}
$$

where c = $\cos\theta$, $c_2 = \cos 2\theta$, $c^2 = \cos^2\theta$ etc. Despite the complexity of the above equation, it can be used to interpret resonant scattering data as will be shown in the following sections.

2.1.3 Determination of Magnetic Structure: Symmetry Analysis

It is worth noting that commensurate magnetic structures, particularly those with more than one magnetic ion in the unit cell (e.g. Ho($2a$) and Ho($4b$) in $HoMnO_3$) require symmetry analysis for a complete solution whereas most of our group's previous work was focused on "simple" incommensurate systems. In both the, "simple" as well as "complex" systems, symmetry analysis simplifies the problem of solving magnetic structures.[71] We will outline the procedure for determining the magnetic structure for R^{3+} in the hexagonal $R\mathrm{MnO_3}$ and discuss the role of symmetry.

Determining the magnetic structure means:

1. Determining the relation between magnetic and chemical unit cell i.e. propagation vector.
2. Determining the magnetic moment direction.
3. Determining the symmetry relationship between different magnetic moments in the unit cell.

For hexagonal $R\mathrm{MnO_3}$, the magnetic propagation vector is known from neutron diffraction experiments to be $\vec{k} = 0$, so that the magnetic unit cell is same as the chemical unit cell. Symmetry analysis limits the possible magnetic structures and dictates the moment direction, and correlations between magnetic moments for a magnetic structure. To determine the possible magnetic structures, we will use representation analysis and outline the procedure for calculating the magnetic moment direction and correlations for a particular representation.

2.1.3.1 Representation Theory and Possible Magnetic Structures

Representational analysis[72, 73, 74, 75, 76, 77, 78] allows the determination of the symmetry-allowed magnetic structures that can result from a second-order magnetic phase transition given the crystal structure, and the propagation vector of the magnetic ordering. The calculation of magnetic structures (magnetic representations), shown in Table 2.8, require several steps starting from the symmetry operations of the crystallographic space group and the propagation vector. Briefly, the steps include:

1. Determination of the little group G_k which maintains the propagation vector invariant.
2. Decomposition of the magnetic representation in terms of the representations of G_k. This tells us the representations of G_k that are compatible with the symmetry operations on the magnetic moments.
3. Determination of basis vectors for a particular representation. This describes the components of the magnetic moments that are compatible with the symmetry operations.

The procedure for calculating magnetic representations will be outlined here with the real example of Ho($2a$) site in $HoMnO_3$. We will define the relevant group theoretical terms in the course of calculating magnetic representations.

Determination of Little Group G_k:

The symmetry operations of G_0 that are consistent with translational periodicity, defined by $\vec{k}$, are those that leave $\vec{k}$ invariant. Only the rotational parts of the symmetry operations change $\vec{k}$. Therefore, if the action of the rotational part of a symmetry operation on $\vec{k}$ is written as

$$\vec{k}' = \vec{k}R, \tag{2.14}$$

the symmetry operations that leave $\vec{k}$ invariant are those that obey the equation

$$\vec{k}' = \vec{k}, \tag{2.15}$$

The group of symmetry operations that obey this relation are called the group of the propagation vector, or the little group, G_k. In the case of RMnO$_3$, the propagation vector $\vec{k}$= (0 0 0), elements in the G_k are the same as G_0. For example, for the rotation operator, R=g_6 (see Table 2.2 for the symmetry operations in G_k),

$$\vec{k}g_6 = \begin{pmatrix} 0 & 0 & 0 \end{pmatrix} \begin{pmatrix} 1 & \bar{1} & 0 \\ 1 & 0 & 0 \\ 0 & 0 & 1 \end{pmatrix} = \begin{pmatrix} 0 & 0 & 0 \end{pmatrix} = \vec{k} \tag{2.16}$$

We have listed the elements of the group in the order of Kovalev's notation in Table 2.2.

Effect of Symmetry Elements on Atomic positions and the Permutation Representation, Γ_{perm}:

A crystal is invariant under all of the symmetry operations of its space group. However, equivalent atoms can be interchanged under the different symmetry operations. For example, operation g_6 interchanges atom 1 (X_1) and 2 (X_2) in the $R(2a)$ site whereas operation g_1 keeps

them invariant. The atomic positions for rare-earths are given in Table 1.2

$$\begin{aligned} g_6 X_1 &= g_6(0\ 0\ z) = (0\ 0\ z+1/2) = X_2 \\ g_2 X_1 &= g_2(0\ 0\ z) = (0\ 0\ z) = X_1 \end{aligned} \tag{2.17}$$

The manner in which all symmetry operations of a group permute the labels of equivalent atoms can be represented by a large matrix, called the permutation representation, Γ_{perm}. The character of the permutation representation for a symmetry operation, $\chi_{perm}(g)$, is simply the number of position labels that are unchanged under its action. In the above example $\chi_{perm}(g_6) = 0$ and $\chi_{perm}(g_1) = 2$. All the $\chi_{perm}(g_i)$ are listed in the Table 2.3.

Effect of Symmetry Elements on Magnetic Moments and the Magnetic Representation, Γ_{mag}:

A magnetic moment is described by an axial vector which, for convenience, will be represented in the axis system of the point or space group that we are using. We will always refer to moment components defined with respect to the crystallographic axes, not Cartesian projections. If the moment vector of an atom is $\vec{M} = (m_a; m_b; m_c)$, then the action of a rotational symmetry element is simply

$$\vec{M}' = R\vec{M} \times det(R) \tag{2.18}$$

Where the determinant, $det(R)$, is required to describe the current loop symmetry of an axial vector (which is not reversed by the inversion operation). The axial vector representation, Γ_{axial}, describes how the components of a moment vector are changed by the different symmetry operations. The character of a given symmetry element is χ_{axial}. Numerically, it is simply the trace (the sum of the leading diagonal elements) of the rotation matrix of the symmetry operation multiplied by the determinant of the rotation matrix. For example, for g_1 symmetry element,

$$\chi_{axial}(g_1) = (1 + 1 + 1) \times 1 = 3 \tag{2.19}$$

The χ_{axial} for all other symmetry elements are listed in Table 2.3.

The Magnetic Representation:

The magnetic representation, Γ_{mag}, describes both the result of the symmetry operations on the atomic positions and on the axial vectors that describe the atomic moments. As these effects are independent, the magnetic representation is given by their direct product:

$$\Gamma_{mag} = \Gamma_{mag} \times \Gamma_{axial} \tag{2.20}$$

The characters of these representations are related according to:

$$\chi_{mag} = \chi_{mag} \times \chi_{axial} \tag{2.21}$$

and are also listed in Table 2.3.

Irreducible Representations of the Space Groups:

Irreducible representations are matrices that map onto the algebra of the space group symmetry operations. They are of particular significance because they are the smallest unique blocks out of which all other representations can be made. In other words, any representation can be written in terms of the different irreducible representations of the group so that the representation can be decomposed into irreducible representations. The dimensionality of an irreducible representation is the dimensionality of the matrix representatives of the representation. The irreducible representations of the space group $G_k = P6_3cm$ for $\vec{k} = 0$ can be obtained from Kovalev's book [77] and are listed in Table 2.4.

Decomposition of the Magnetic Representation into Irreducible Representations of G_k:

Γ_{mag} describes how the atomic moments change under all the different symmetry operations of a space group. It is reducible and can be written in terms of the irreducible representations of the space group. Therefore, Γ_{mag} can be decomposed into the irreducible representations of the space group G_k. In this case, the magnetic representation for an atomic site can be decomposed into contributions from the irreducible representations of the little group.

$$\Gamma_{mag} = \sum_{\nu} n_\nu \Gamma_\nu \tag{2.22}$$

where n_ν is the number of times the irreducible representation Γ_ν appears in the magnetic representation Γ_{mag}. n_ν is given by:

$$n_\nu = \frac{1}{n(G_k)} \sum_{g \in G_k} \chi_{\Gamma_{mag}(g)} \chi^\star_{\Gamma_\nu(g)} \tag{2.23}$$

Here $\chi_{\Gamma_{mag}(g)}$ is the character of the magnetic representation listed in Table 2.3 and $\chi^\star_{\Gamma_\nu(g)}$ is the complex conjugate of the character of the irreducible representation with index ν for element g (see Table 2.4). Let's give here an example for the $R(2a)$ site in $R\mathrm{MnO_3}$.
For $\nu = 1$ (the Γ_1 representation),

$$\begin{aligned} n_2 =& 1/12[(6\times 1)+(0\times 1)+(0\times 1)+(0\times 1)+(0\times 1)+(0\times 1)+(0\times 1)+(-2\times 1)+(0\times 1) \\ &+(-2\times 1)+(0\times 1)+(-2\times 1)+(-2\times 1)+(0\times 1)+(-2\times 1)] = 0 \end{aligned} \tag{2.24}$$

For $\nu = 2$ (Γ_2 representation),

$$\begin{aligned} n_2 =& 1/12[(6\times 1)+(0\times 1)+(0\times 1)+(0\times 1)+(0\times 1)+(0\times 1)+(0\times -1)+(-2\times -1) \\ &+(0\times -1)+(-2\times -1)+(0\times -1)+(-2\times -1)+(-2\times -1)+(0\times -1)+(-2\times -1)] = 1 \end{aligned} \tag{2.25}$$

Following the procedure described above, the decomposition of Γ_{mag} into irreducible representations of G_k:

$$\Gamma_{mag} = 0\Gamma_1^1 + 1\Gamma_2^1 + 1\Gamma_3^1 + 0\Gamma_4^1 + 1\Gamma_5^2 + 1\Gamma_6^2 \tag{2.26}$$

where the superscript represents the order of the irreducible representation and the subscript is its index or label. $x\Gamma_1^1$ implies that the Γ_1 representation of order 1 contains x number of basis vectors.

Basis Vectors and Basis Vector Space:

Symmetry adapted linear combinations, also called *basis vectors*, are obtained by projection from test functions [e.g. (1 0 0), (0 1 0) and (0 0 1) are three test functions representing the direction of three crystallographic axes] components that are compatible with one row of an irreducible representation matrix. Only functions that have the same symmetry as the

irreducible representations under all of the different symmetry operations of the group give non-zero results and these are the symmetry adapted linear combinations. Calculation of the basis vectors is done using the projection operator technique, which involves taking a test function and projecting from it the part that transforms according to each of the irreducible representations. We will use the notation $\vec{\psi}_n$ as the basis vector that transforms according to the μ dimensional representation Γ^{μ}_{ν}, and D^{ν} is the matrix representative of the irreducible representation with index ν. The projection process determines the component of the test function that transforms according to the irreducible representation that is under investigation. If there is symmetry adapted component, then the projection will give non-zero results otherwise it will be zero. The projection operator formula is: [74]

$$\vec{\psi}^{\lambda}_{\alpha\nu} = \sum_{g \in G_k} D^{\lambda\star}_{\nu}(g) \sum_{i} \delta_{i,g_i} R_g \vec{\phi}_{\alpha} det(R_g) \tag{2.27}$$

where:

1. $\vec{\psi}^{\lambda}_{\alpha\nu}$ is the basis vector projected from the λth row of the νth irreducible representation using basis vector $\vec{\phi}_{\alpha}$.

2. $g \in G_k$ means that the sum is over the symmetry elements that are in G_k.

3. $D^{\lambda\star}_{\nu}(g)$ is the complex conjugate of the element of the matrix representative that is being examined: it is the λth row of the matrix representative of the ν irreducible representation, for symmetry operation g.

4. $\sum_i$ means that the following summation is over all of the atomic positions that are related by the symmetry elements of the space group.

5. δ_{i,g_i} is the Kronecker delta and means that effectively the sum is over the symmetry elements that move an atom to a position that has the same level.

6. $det(R_g)$ is the determinant of the rotational part of the symmetry element (R_g).

7. $\vec{\phi}_{\alpha}$ is the test function.

We will select the following test functions:

$$\begin{aligned} \vec{\phi}_1 &= (1\ 0\ 0) \\ \vec{\phi}_2 &= (0\ 1\ 0) \\ \vec{\phi}_3 &= (0\ 0\ 1) \end{aligned} \tag{2.28}$$

From the Tables 2.5, 2.6 and 2.7 and, for the $R(2a)$ site in the Γ_3 representation, we obtain the basis vector $\vec{\psi_3}$ where $\vec{\psi_3} = (0\ 0\ 6)$ for atom 1 at position X_1 and $(0\ 0\ -6)$ for atom 2 and position X_2. Therefore, for the Γ_3 representation, the magnetic moments are aligned along the hexagonal **c** direction with antiferromagnetic correlation between them. The same procedure has to be applied for other representations (Γ_2, Γ_5 and Γ_6) for the $R(2a)$ site and from Γ_1 to Γ_6 for the $R(4b)$ site. The calculations are tedious but straight-forward. The calculations can be verified or done with the software package SARAh [74] and we show the final results in Table 2.8 which describes the correlations between magnetic moments at the same Wyckoff site. The correlation between magnetic moments at the two independent Wyckoff sites ($2a$ and $4b$) has to be obtained experimentally. Fig. 2.6 show one of the possible realizations of the magnetic structure for every representation.

2.1.3.2 Determination of the Magnetic Moment Direction

The magnetic moment directions are specified by the magnetic representations. Therefore, determination of magnetic representation implies determination of magnetic moment direction as well as the correlation between magnetic moments. For a determination of the magnetic representation, a detailed calculation of the magnetic structure factor is necessary and will be presented in the next section.

2.1.3.3 Calculation of Magnetic Structure Factor to Discriminate Between Different Magnetic Representations

Here we outline the calculation of magnetic structure factors for different representations for the rare-earth moments, listed in the Table 2.8, for the crystallographic space group $P6_3cm$.

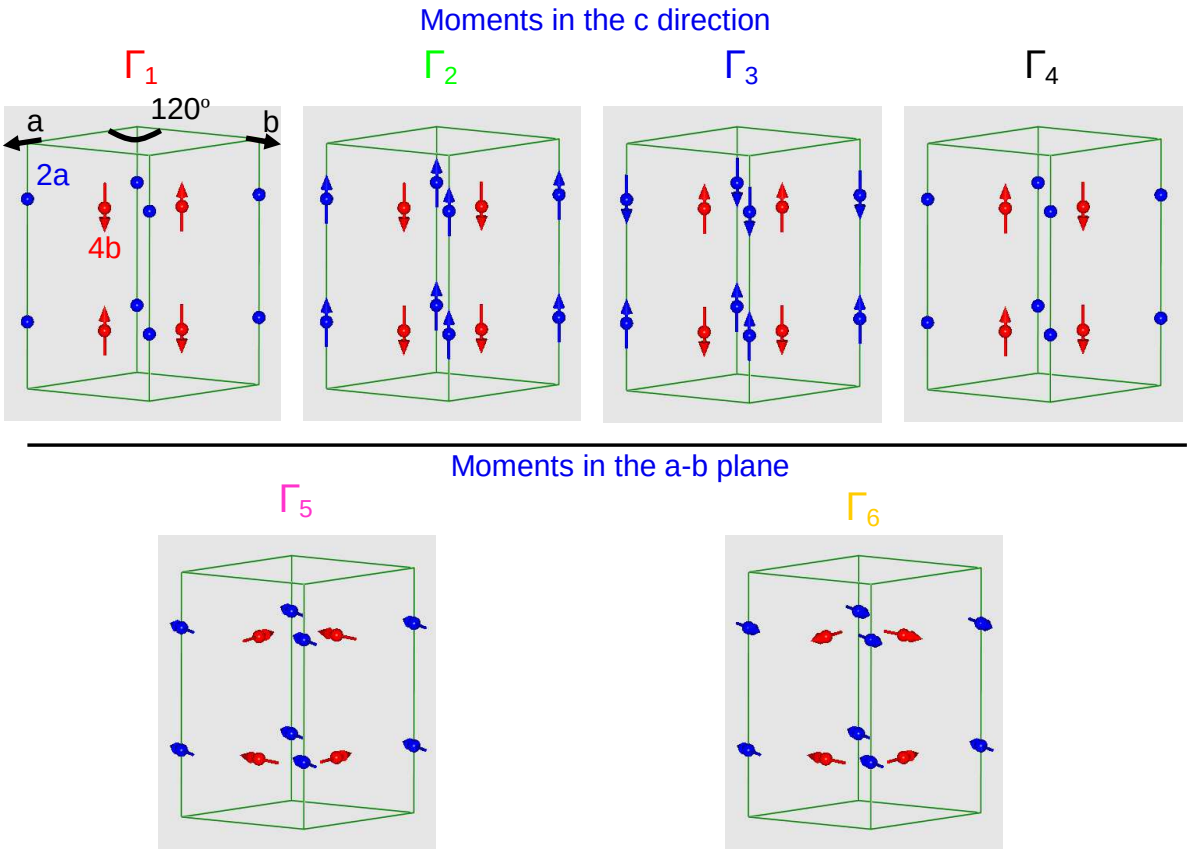

Figure 2.6 Possible magnetic representations for the crystallographic space group $P6_3cm$ associated with a magnetic unit cell same as the crystallographic unit cell. Only Ho^{3+} moments are shown.

The magnetic structure factor F_M for resonant magnetic scattering can be written as:

$$F_M = \sum_{j_k=1}^{\substack{4(k=4b)\\2(k=2a)}} f_{j_k}^{\mathrm{XRMS}} e^{2\pi i(hx_{j_k}+ky_{j_k}+lz_{j_k})} \tag{2.29}$$

The summation is over the two Wyckoff sites for the rare-earths, namely $R(2a)$ and $R(4b)$. f^{XRMS} is the resonant magnetic scattering amplitude which is listed for different polarization geometries in Eq's. 2.12, 2.13 for both the dipole and quadrupole resonances. In particular, f^{XRMS} depends on the polarization geometry as well as the moment direction. The different magnetic representations that are possible for the crystallographic space group $P6_3cm$ with a magnetic unit cell the same as the chemical unit cell are listed in Table 2.8. Since there are two distinct Wyckoff sites in the unit cell, both sites may not order in the same magnetic representation and the moments at the two different sites can be coupled or decoupled depending on the interaction between different magnetic sublattices. Without detailed knowledge of the magnetic Hamiltonian we will proceed to calculate F_M for the following cases:

(A) Both sites order in the same magnetic representation and are coupled.

(B) Both sites order in the same magnetic representation but are decoupled.

(C) Both sites order in two different magnetic representations and are decoupled.

The main difference between (A) and (B) is that number of possible domains will be different and hence, when averaged over domains, the diffraction intensities will be different.

Case A

As discussed in Ref. [79], case A is valid for a continuous or "approximately" continuous phase transition with dominant second order terms in the Hamiltonian. For dipole scattering in $\sigma \rightarrow \pi^{'}$ geometry we can write (see Eq. 2.12):

$$f_{E1}^{\mathrm{XRMS}} = -iF_{E1}^{(1)}[z_3 \sin(\theta+\alpha) - z_1 \cos(\theta+\alpha)] \tag{2.30}$$

where $(\theta+\alpha)$ is the angle between the outgoing wavevector $(\hat{\mathbf{k}}^{'})$ and the $\hat{\mathbf{a}}^*$ direction and z_i's are the components of the magnetic moment unit vector along the three cartesian axes. We select $\hat{\mathbf{a}}^*$, $\hat{\mathbf{b}}$ and $\hat{\mathbf{c}}^*$ as the three unit vectors along the three orthogonal cartesian axes. $f_{E1}^{(1)}$

is the dipole scattering matrix element which is generally proportional to the magnitude of the magnetic moment (see for example Ref. [80]). We will assume for both R sites

$$F_{E1}^{(1)} = C\mu, \tag{2.31}$$

where C is a scaling factor. With the help of Eq. 2.29 and 2.31, $|F_m|^2$ can be written in the following forms for $(h\ 0\ l)$ reflections with l odd:

Γ_1: $R(4b)$ in Γ_1

$$|F_m|^2 = 16C^2\mu_{4b}^2 \sin^2(\theta+\alpha)\sin^2\frac{2\pi h}{3} \tag{2.32}$$

Γ_2: $R(2a)$ and $R(4b)$ in Γ_2

$$|F_m|^2 = 0 \tag{2.33}$$

Γ_3: $R(2a)$ and $R(4b)$ in Γ_3

$$\begin{aligned} |F_m|^2 = 4C^2\sin^2(\theta+\alpha)[\mu_{2a}^2 + 4\mu_{4b}^2\cos^2\frac{2\pi h}{3} \\ + 4\mu_{2a}\mu_{4b}\cos\frac{2\pi h}{3}\cos 2\pi(z_{2a}-z_{4b})l] \end{aligned} \tag{2.34}$$

Γ_4:

$$|F_m|^2 = 0 \tag{2.35}$$

Γ_5: $R(2a)$ and $R(4b)$ in Γ_5

For the Γ_5 magnetic representation and for the given orientations of magnetic moments in Table 2.8 we can write:

$$|F_m|^2 = 3C^2(p-r)^2\cos^2(\theta+\alpha)\sin^2\frac{2\pi h}{3} \tag{2.36}$$

However, the Γ_5 magnetic representation allows 120° orientational domains which yield different $|F_m|^2$. Assuming equal population of magnetic domains we can write:

$$\begin{aligned} |F_m|^2 = 3C^2\frac{1}{3}[(p-r)^2 + (q-s)^2 + \{(p-r)-(q-s)\}^2] \\ \cos^2(\theta+\alpha)\sin^2\frac{2\pi h}{3} \end{aligned} \tag{2.37}$$

Again,

$$\begin{aligned}\boldsymbol{\mu}_{4b}^{(1)} &= [p\ q\ 0] = \frac{\sqrt{3}}{2}p\hat{\mathbf{a}}^* + (q - \frac{1}{2}p)\hat{\mathbf{b}} \\ \boldsymbol{\mu}_{4b}^{(2)} &= [r\ s\ 0] = \frac{\sqrt{3}}{2}r\hat{\mathbf{a}}^* + (s - \frac{1}{2}r)\hat{\mathbf{b}}\end{aligned} \tag{2.38}$$

Also,

$$\begin{aligned}\boldsymbol{\mu}_{4b}^{(1)} - \boldsymbol{\mu}_{4b}^{(2)} &= \frac{\sqrt{3}}{2}(p-r)\hat{\mathbf{a}}^* + \{(q-s) - \frac{1}{2}(p-r)\}\hat{\mathbf{b}} \\ (\boldsymbol{\mu}_{4b}^{(1)} - \boldsymbol{\mu}_{4b}^{(2)}) \cdot (\boldsymbol{\mu}_{4b}^{(1)} - \boldsymbol{\mu}_{4b}^{(2)}) &= \frac{1}{2}[(p-r)^2 + (q-s)^2 \\ &\quad + \{(p-r) - (q-s)\}^2]\end{aligned} \tag{2.39}$$

Therefore, using Eq. 2.39, we can simplify Eq. 2.37 as follows:

$$|F_m|^2 = 2C^2\cos^2(\theta+\alpha)\sin^2\frac{2\pi h}{3}(\boldsymbol{\mu}_{4b}^{(1)} - \boldsymbol{\mu}_{4b}^{(2)})^2 \tag{2.40}$$

again assuming equal population of domains.

Γ_6: $R(2a)$ and $R(4b)$ in Γ_6

For the Γ_6 magnetic representation and for the orientation of magnetic moments in Table 2.8, we can write:

$$\begin{aligned}|F_m|^2 = 3C^2\cos^2(\theta+\alpha)[u^2 + (p+r)^2\cos^2\frac{2\pi h}{3} \\ + 2u(p+r)\cos\frac{2\pi h}{3}\cos 2\pi(z_{2a} - z_{4b})l]\end{aligned} \tag{2.41}$$

When the magnetic moments at the two sites are coupled, averaging over all possible domains yields:

$$\begin{aligned}|F_m|^2 = 2C^2\cos^2(\theta+\alpha)[\mu_{2a}^2 + (\boldsymbol{\mu}_{4b}^{(1)} + \boldsymbol{\mu}_{4b}^{(2)})^2\cos^2\frac{2\pi h}{3} \\ + \boldsymbol{\mu}_{2a}\cdot(\boldsymbol{\mu}_{4b}^{(1)} + \boldsymbol{\mu}_{4b}^{(2)})\cos\frac{2\pi h}{3}\cos 2\pi(z_{2a} - z_{4b})l]\end{aligned} \tag{2.42}$$

Case B In case B, both sites belong to the same magnetic representation but are decoupled i.e. the two sites order independently. For Γ_1, Γ_2 Γ_4 and Γ_5 magnetic representations $|F_m|^2$ is the same as that of case A because $|F_m|^2$ is either zero (Γ_2 and Γ_4) or contains only squared terms of magnetic moments(Γ_1 and Γ_5)

Γ_3:

If the moments in the $R(2a)$ site are in the same orientation as in Table 2.8, reversing the

moments at the $R(4b)$ site introduces a " $-$ " before the term $\mu_{2a}\mu_{4b}\cos\frac{2\pi h}{3}\cos 2\pi(z_{2a}-z_{4b})l$ (*interference term*) in Eq. 2.34. Therefore, averaging over such domains yields:

$$|F_m|^2 = 4C^2\sin^2(\theta+\alpha)[\mu_{2a}^2 + 4\mu_{4b}^2\cos^2\frac{2\pi h}{3}] \tag{2.43}$$

Similarly for Γ_6:

$$|F_m|^2 = 2C^2\cos^2(\theta+\alpha)[\mu_{2a}^2 + (\boldsymbol{\mu}_{4b}^{(1)} + \boldsymbol{\mu}_{4b}^{(2)})^2\cos^2\frac{2\pi h}{3}] \tag{2.44}$$

Case C As discussed later in Chapter 3, in the intermediate temperature phase (ITP) of $HoMnO_3$, we concluded that one of the R site must be in the Γ_3 representation. The other site can be in the same magnetic representation or may be found in one of the other five magnetic representations. We will calculate $|F_m|^2$ for all of these combinations. As we have measured $(0\ 0\ l)$ reflections with l odd to distinguish between all possible combinations, we will outline the calculations for these reflections only. For $R(2a)$ in Γ_3, the other site may be in Γ_2, Γ_4, or Γ_5. Then,

$$|F_m|^2 = 4C^2\mu_{2a}^2\sin^2\theta \tag{2.45}$$

In the above case, the $R(4b)$ site does not contribute to $(0\ 0\ l)$ reflections. On the other hand if $R(4b)$ is in Γ_3 and the $R(2a)$ is in Γ_2, Γ_4, or Γ_5, then:

$$|F_m|^2 = 16C^2\mu_{4b}^2\sin^2\theta \tag{2.46}$$

In this case the $R(2a)$ site does not contribute to $(0\ 0\ l)$ reflections. If $R(2a)$ is in Γ_6 and $R(4b)$ is in Γ_3 then for the configuration given in Table 2.8 we can write:

$$\begin{aligned} |F_m|^2 = C^2[&3u^2\cos^2\theta + 16\mu_{4b}^2\sin^2\theta \\ &+ 8\sqrt{3}u\mu_{4b}\cos\theta\sin\theta\cos 2\pi(z_{2a}-z_{4b})l] \end{aligned} \tag{2.47}$$

However, a 180° rotation of the moments at the $R(2a)$ site, while keeping the $R(4b)$ moments in the above configuration, introduces a " $-$ " sign before the *interference term* i.e. the term containing contributions from both sites. Therefore, averaging over such domains and 120° orientation domains yield:

$$|F_m|^2 = 2C^2(\mu_{2a}^2\cos^2\theta + 8\mu_{4b}^2\sin^2\theta) \tag{2.48}$$

In the similar way, $|F_m|^2$ for the opposite combination i.e. $R(2a)$ in Γ_3 and $R(4b)$ in Γ_6 can be calculated and yields:

$$|F_m|^2 = 2C^2[2\mu_{2a}^2 \sin^2\theta + (\boldsymbol{\mu}_{4b}^{(1)} + \boldsymbol{\mu}_{4b}^{(2)})^2 \cos^2\theta] \tag{2.49}$$

We have assumed equal population of all possible domains to derive the above two equations.

Now, in the LTP for $HoMnO_3$, the $R(4b)$ site was determined to be in the Γ_1 representation (See Chapter 3). We will consider all combinations with $R(4b)$ in Γ_1 and $R(2a)$ in an other representation. For $(h\ 0\ l)$ reflections with l odd.

(a) $R(2a)$ is in any of the following representations Γ_2, Γ_4, Γ_5 then:$|F_m|^2$ is same as Eq. 2.32.

(b) $R(2a)$ is in Γ_3:

$$|F_m|^2 = 4C^2 \sin^2(\theta+\alpha)(\mu_{2a}^2 + 4\mu_{4b}^2 \sin^2\frac{2\pi h}{3}) \tag{2.50}$$

(c)$R(2a)$ is in Γ_6:

$$|F_m|^2 = C^2[2\mu_{2a}^2 \cos^2(\theta+\alpha) + 16\mu_{4b}^2 \sin^2(\theta+\alpha)\sin^2\frac{2\pi h}{3}) \tag{2.51}$$

Calculation of $|F_m|^2$ for quadrupole resonance We have also measured the angular dependence for the quadrupole resonance. For the moments in the **c** direction and for specular reflections in $\sigma \rightarrow \pi^{'}$ geometry we can write (See, Eq. 2.13)

$$\begin{aligned} f_{E2}^{\mathrm{XRMS}} &= -i\cos 2\theta \sin\theta F_{E2}^{(1)} + i(F_{E2}^{(3)} - F_{E2}^{(1)}) z_3^3 \sin^3\theta \\ &\quad - iF_{E2}^{(3)} z_3^3 \cos^2\theta \sin\theta \end{aligned} \tag{2.52}$$

For moments in the **c** direction, $z_3^3 = z_3$ and hence the above equation can be simplified as follows:

$$f_{E2}^{\mathrm{XRMS}} = -iF_{E2}^{(1)} z_3 \sin\theta[1 + B - \sin^2\theta(1+2B)] \tag{2.53}$$

where $B = \frac{F_{E2}^{(3)}}{F_{E2}^{(1)}}$ as $\sin^2\theta = \frac{\lambda^2 l^2}{4c^2}$. The above equation becomes:

$$f_{E2}^{\mathrm{XRMS}} = -iF_{E2}^{(1)} z_3 \sin\theta[1 + B - \frac{\lambda^2 l^2}{4c^2}(1+2B)] \tag{2.54}$$

Again assuming $F_{E2}^{(1)}$ is proportional to the magnetic moment, we can write:

$$|F_m|^2_{quadrupole} = C^2|F_m|^2_{dipole}[1 + B - \frac{\lambda^2 l^2}{4c^2}(1 + 2B)]^2 \tag{2.55}$$

where C is an arbitrary positive constant. For moments in the **a-b** plane and in an arbitrary direction (as in Γ_5 and Γ_6), the algebra for $|F_m|^2_{quadrupole}$ becomes complex because $z_1^n \neq z_1$ (n integer) and can not be put into a simple form.

2.2 X-Ray Magnetic Circular Dichroism

X-ray magnetic circular dichroism (XMCD) is a measure of the difference between absorption coefficient (μ_c=$\mu^+ - \mu^-$), with the helicity of the incident circularly polarized x-rays parallel (μ^+) or anti-parallel (μ^-) to the local magnetization direction of the absorbing material.[81] The dichroic signal is proportional to the projection of magnetic moment along the beam direction. Similar to XRMS, XMCD measurements are also performed at the absorption edges of a element of interest, and therefore, this technique is also element specific. XMCD can be used to determine element specific magnetization of ferrimagnetic and ferromagnetic materials. Compared to conventional magnetization techniques such as SQUID measurements where the signal is proportional to the bulk magnetization, XMCD signal is proportional to the magnetization of a particular element (determined by the element's absorption edge) within the bulk. XMCD can also be used to separate orbital $\langle L_z \rangle$ and spin $\langle S_z \rangle$ contribution of a magnetic moment through magneto-optical sum rules in some cases.[82, 83] It is primarily the elemental and orbital specificity that makes XMCD a useful tool for study of magnetic materials.

2.2.1 Basic Theory of XMCD

The theory of XMCD and XRMS is very similar, given that the absorption is determined by the imaginary part of the forward scattering. To leading order, the magnetization-sensitive absorption is determined by the coupling:[84, 85]

$$H_{int} = -\sum_j \frac{e}{mc}\vec{p}_j \cdot \vec{A} \tag{2.56}$$

Given a magnetic ion, the absorption coefficient for an 2^L pole electric (e) transition is proportional to

$$W^e_{EL} = \frac{4\pi}{k} \sum_{M=-L}^{L} |\hat{e} \cdot Y^e_{LM}(\hat{k})|^2 w^e_{LM}(k) \tag{2.57}$$

where $\hat{k}$ and $\hat{e}$ stands for the unit vector in the direction of photon momentum and the unit polarization, respectively. Similar to XRMS, polarization properties depend on $\hat{e} \cdot Y^e_{LM}(\hat{k})$ term in the above equation 2.57.

Since, XMCD is a measure of the difference between absorption coefficient (μ_c=$\mu^+ - \mu^-$), with the helicity of the incident circularly polarized x-rays parallel (μ^+) or anti-parallel (μ^-) to the local magnetization direction of the absorbing material, the XMCD signal for dipole and quadrupole can be written as:

$$\begin{aligned} \mu_c^{E_1} &= W_{E_1}(k, \hat{e}^+) - W_{E_1}(k, \hat{e}^-) \\ &= \frac{6\pi N}{k}[w^e_{11} - w^e_{1-1}] \cos\theta \end{aligned} \tag{2.58}$$

$$\begin{aligned} \mu_c^{E_2} &= W_{E_2}(k, \hat{e}^+) - W_{E_2}(k, \hat{e}^-) \\ &= \frac{6\pi\ N}{k}[\{w^e_{22} - w^e_{2-2}\} \sin^2\theta + \{w^e_{21} - w^e_{2-1}\} \cos 2\theta] \cos\theta \end{aligned} \tag{2.59}$$

where $\cos\theta = \hat{k} \cdot \hat{z}$, with $\hat{k}$ and $\hat{z}$ are the unit vectors in the direction of photon momentum and local magnetization, respectively. N represents the number of atoms per unit volume and $\hat{e}^+$, $\hat{e}^-$ are the right and left handed circular polarization vectors, respectively. The contribution of the local magnetization to the XMCD signal can be understood from the expression for w^e_{LM} given below:

$$w^{(e)}_{LM} = 4\pi^2 e^2 \sum_n \left[\frac{L+1}{L[(2L+1)!!]^2}\right] k^{2L} \times \left| \langle n | \sum_j r_j^L Y_{LM} | a \rangle \right|^2 \delta(E_a - E_n - \hbar\omega) \tag{2.60}$$

Considering an excited state with a finite width i.e. $\delta \rightarrow 2/\pi\Gamma(x^2+1)$ where $x = (E_n - E_a - \hbar\omega)/(\Gamma/2)$ and assuming an exchange splitting Δ ($<< \Gamma$) of the outer levels, described by $x_\pm = x \pm \Delta/\Gamma$, the substitution $w^e_{LM} = v^{(e)}_{LM} 2/\Gamma(x_+^2 + 1)$, yields:

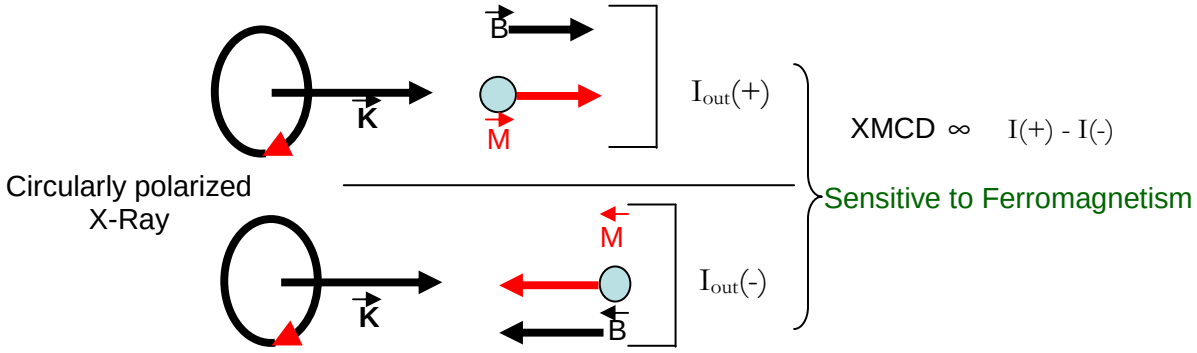

Figure 2.7 Schematic illustration of the XMCD measurement. The figure shows measurement of XMCD by changing the magnetic field direction. XMCD can also be measured by changing the helicity of circularly polarized x-rays.

$$w^e_{LM} - w^e_{L-M} = \frac{\frac{2}{\Gamma}}{x^2+1}\left((v^e_{LM} - v^e_{L-M}) - \frac{\Delta}{\Gamma}\frac{2x}{x^2+1}\right)(v^e_{LM} - v^e_{L-M}) \tag{2.61}$$

The first term in Eq. 2.61 describes dependence of XMCD on the spin polarization of the final state and the second term on the exchange splitting and is therefore sensitive to magnetism. The sensitivity to ferromagnetism comes from the term $\cos\theta = \hat{k}\cdot\hat{z}$ term in Eq. 2.58 with $\hat{k}$ and $\hat{z}$ are the unit vectors in the direction of photon momentum and local magnetization.

2.2.2 Measurement Procedure

The most common method to obtain XMCD spectra is to measure the absorption by monitoring the incoming I_0 and transmitted (I) fluxes. The absorption in the sample is then given by:

$$\mu_0 t = \ln\left(\frac{I_0}{I}\right) \tag{2.62}$$

The dichroism measurement is obtained by reversing the helicity or magnetization of the sample and taking the difference between two measurements ($\mu_c = \mu^+ - \mu^-$). The schematic of detecting XMCD is shown in Fig. 2.7. The thickness, t, is a proportionality factor in μ_c and can be removed by expressing dichroism as a ratio μ_c/μ_0 where μ_0 is the normal absorption. A typical XMCD spectra for a thin layer of metallic Fe is shown in Fig. 2.8.[86]

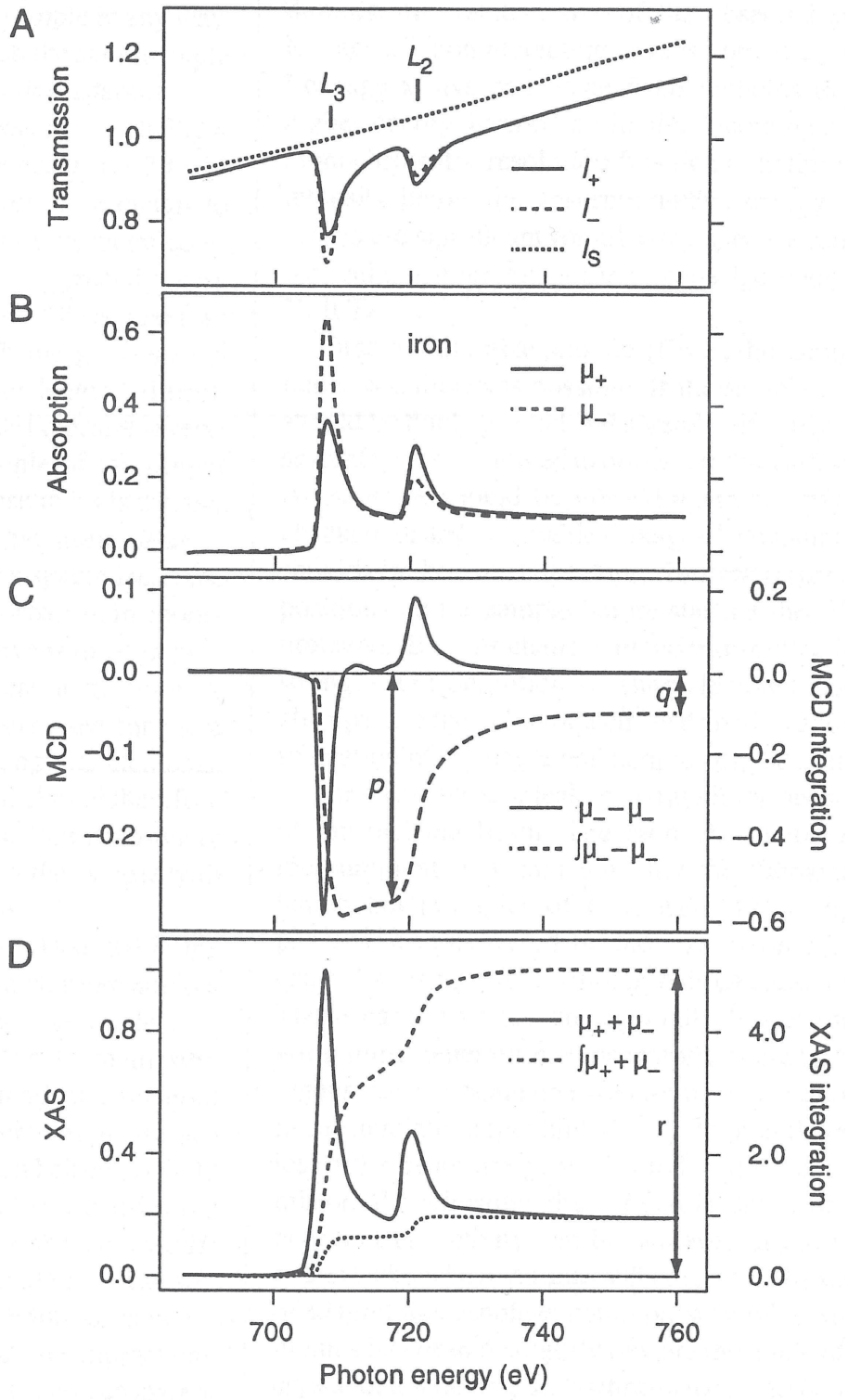

Figure 2.8 XMCD spectra demonstrated for a thin layer of metallic iron. (A) Transmitted intensity of parylene substrate and substrate with deposited sample. (B) Calculated absorption with background subtracted. (C) Absorption spectra and edge-jump model curve along with integrated signal. After Ref. [86]

Table 2.2 Symmetry elements of the little group $G_{\vec{k}}$. The notations used are of the International Tables, where the elements are separated into rotation and translation components, and the *Jones faithful representations*. After Refs. [75, 76]

Element g_n	Rotation matrix R	IT notation $g_n = \{R \mid \tau\}$	Kovalev notation $g_n = \{h_n \mid \tau\}$	Jones symbol
g_1	$\begin{pmatrix} 1 & 0 & 0 \\ 0 & 1 & 0 \\ 0 & 0 & 1 \end{pmatrix}$	$\{E\mid 0\ 0\ 0\}$	$\{h_1 \mid 0\ 0\ 0\}$	x, y, z
g_6	$\begin{pmatrix} 1 & \bar{1} & 0 \\ 1 & 0 & 0 \\ 0 & 0 & 1 \end{pmatrix}$	$\{C_6^+\mid 0\ 0\ .5\}$	$\{h_2 \mid 0\ 0\ .5\}$	$x-y, x, z+\frac{1}{2}$
g_2	$\begin{pmatrix} 0 & \bar{1} & 0 \\ 1 & \bar{1} & 0 \\ 0 & 0 & 1 \end{pmatrix}$	$\{C_3^+\mid 0\ 0\ 0\}$	$\{h_3 \mid 0\ 0\ 0\}$	$-y, x-y, z$
g_4	$\begin{pmatrix} \bar{1} & 0 & 0 \\ 0 & \bar{1} & 0 \\ 0 & 0 & 1 \end{pmatrix}$	$\{C_2\mid 0\ 0\ .5\}$	$\{h_4 \mid 0\ 0\ .5\}$	$-x, -y, z+\frac{1}{2}$
g_3	$\begin{pmatrix} \bar{1} & 1 & 0 \\ \bar{1} & 0 & 0 \\ 0 & 0 & 1 \end{pmatrix}$	$\{C_3^-\mid 0\ 0\ 0\}$	$\{h_5 \mid 0\ 0\ 0\}$	$-x+y, -x, z$
g_5	$\begin{pmatrix} 0 & 1 & 0 \\ \bar{1} & 1 & 0 \\ 0 & 0 & 1 \end{pmatrix}$	$\{C_6^-\mid 0\ 0\ .5\}$	$\{h_6 \mid 0\ 0\ .5\}$	$y, -x+y, z+\frac{1}{2}$
g_9	$\begin{pmatrix} 1 & 0 & 0 \\ 1 & \bar{1} & 0 \\ 0 & 0 & 1 \end{pmatrix}$	$\{\sigma_{v2}\mid 0\ 0\ .5\}$	$\{h_{19} \mid 0\ 0\ .5\}$	$x, x-y, z+\frac{1}{2}$
g_{10}	$\begin{pmatrix} 0 & 1 & 0 \\ 1 & 0 & 0 \\ 0 & 0 & 1 \end{pmatrix}$	$\{\sigma_{d3}\mid 0\ 0\ 1\}$	$\{h_{20} \mid 0\ 0\ 1\}$	$y, x, z+\frac{1}{1}$
g_8	$\begin{pmatrix} \bar{1} & 1 & 0 \\ 0 & 1 & 0 \\ 0 & 0 & 1 \end{pmatrix}$	$\{\sigma_{v1}\mid 0\ 0\ .5\}$	$\{h_{21} \mid 0\ 0\ .5\}$	$-x+y, y, z+\frac{1}{2}$
g_{12}	$\begin{pmatrix} \bar{1} & 0 & 0 \\ \bar{1} & 1 & 0 \\ 0 & 0 & 1 \end{pmatrix}$	$\{\sigma_{d2}\mid 0\ 0\ 1\}$	$\{h_{22} \mid 0\ 0\ 1\}$	$-x, -x+y, z+\frac{1}{1}$
g_7	$\begin{pmatrix} 0 & \bar{1} & 0 \\ \bar{1} & 0 & 0 \\ 0 & 0 & 1 \end{pmatrix}$	$\{\sigma_{v3}\mid 0\ 0\ .5\}$	$\{h_{23} \mid 0\ 0\ .5\}$	$-y, -x, z+\frac{1}{2}$
g_{11}	$\begin{pmatrix} 1 & \bar{1} & 0 \\ 0 & \bar{1} & 0 \\ 0 & 0 & 1 \end{pmatrix}$	$\{\sigma_{d1}\mid 0\ 0\ 1\}$	$\{h_{24} \mid 0\ 0\ 1\}$	$x-y, -y, z+\frac{1}{1}$

Table 2.3 Characters of the permutation, axial and magnetic representations

Character	h_1	h_2	h_3	h_4	h_5	h_6	h_{19}	h_{20}	h_{21}	h_{22}	h_{23}	h_{24}
χ_{perm}	2	0	2	0	2	0	0	2	0	2	0	2
χ_{axial}	3	2	0	-1	0	2	-1	-1	-1	-1	-1	-1
χ_{mag}	6	0	0	0	0	0	0	-2	0	-2	0	-2
$det(g)$	1	1	1	1	1	1	-1	-1	-1	-1	-1	-1

Table 2.4 Irreducible representations of the space group $G_k = P6_3cm$ for $\vec{k} = 0$ in Kovalev's notation.

KV	h_1	h_2	h_3	h_4	h_5	h_6	h_{19}	h_{20}	h_{21}	h_{22}	h_{23}	h_{24}
Γ_1	1	1	1	1	1	1	1	1	1	1	1	1
Γ_2	1	1	1	1	1	1	-1	-1	-1	-1	-1	-1
Γ_3	1	-1	1	-1	1	-1	1	-1	1	-1	1	-1
Γ_4	1	-1	1	-1	1	-1	-1	1	-1	1	-1	1
Γ_5	I	B_1	-B_2	-I	-B_1	B_2	A	C_1	-C_2	-A	-C_1	C_2
Γ_5	I	-B_1	-B_2	I	-B_1	-B_2	A	-C_1	-C_2	A	-C_1	-C_2
I=$\begin{pmatrix} 1 & 0 \\ 0 & 1 \end{pmatrix}$	A=$\begin{pmatrix} 0 & 1 \\ 1 & 0 \end{pmatrix}$	B_1=$\begin{pmatrix} \omega & 0 \\ 0 & \omega^\star \end{pmatrix}$	B_2=$\begin{pmatrix} \omega^\star & 0 \\ 0 & \omega \end{pmatrix}$	C_1=$\begin{pmatrix} 0 & \omega \\ \omega^\star & 0 \end{pmatrix}$	C_2=$\begin{pmatrix} 0 & \omega^\star \\ \omega & 0 \end{pmatrix}$							

Table 2.5 Projection of basis vectors along (1 0 0) from Γ_3 for the $R(2a)$ site with $X_1 = (0\ 0\ z)$ and $X_2 = (0\ 0\ z{+}1/2)$. The last column is the final result of the projection which shows that for $R(2a)$ site, and for Γ_3, there is no component along the hexagonal **a** direction.

R_n	R	$\vec{\phi_1}$	$D_3^{1\star}$	det(R)	$D_3^{1\star} \times R_n \times det(R) \times \vec{\phi_1}$	$g_n X_1$	Sum of Basis Vectors for Each Atom Type
R_1	$\begin{pmatrix} 1 & 0 & 0 \\ 0 & 1 & 0 \\ 0 & 0 & 1 \end{pmatrix}$	$\begin{pmatrix} 1 \\ 0 \\ 0 \end{pmatrix}$	1	1	$\begin{pmatrix} 1 \\ 0 \\ 0 \end{pmatrix}$	X_1	For Atom TypeX_1
R_2	$\begin{pmatrix} 1 & \bar{1} & 0 \\ 1 & 0 & 0 \\ 0 & 0 & 1 \end{pmatrix}$	$\begin{pmatrix} 1 \\ 0 \\ 0 \end{pmatrix}$	-1	1	$\begin{pmatrix} -1 \\ -1 \\ 0 \end{pmatrix}$	X_2	$\begin{pmatrix} 0 \\ 0 \\ 0 \end{pmatrix}$
R_3	$\begin{pmatrix} 0 & \bar{1} & 0 \\ 1 & \bar{1} & 0 \\ 0 & 0 & 1 \end{pmatrix}$	$\begin{pmatrix} 1 \\ 0 \\ 0 \end{pmatrix}$	1	1	$\begin{pmatrix} 0 \\ 1 \\ 0 \end{pmatrix}$	X_1	For Atom TypeX_2
R_4	$\begin{pmatrix} \bar{1} & 0 & 0 \\ 0 & \bar{1} & 0 \\ 0 & 0 & 1 \end{pmatrix}$	$\begin{pmatrix} 1 \\ 0 \\ 0 \end{pmatrix}$	-1	1	$\begin{pmatrix} 1 \\ 0 \\ 0 \end{pmatrix}$	X_2	$\begin{pmatrix} 0 \\ 0 \\ 0 \end{pmatrix}$
R_5	$\begin{pmatrix} \bar{1} & 1 & 0 \\ \bar{1} & 0 & 0 \\ 0 & 0 & 1 \end{pmatrix}$	$\begin{pmatrix} 1 \\ 0 \\ 0 \end{pmatrix}$	1	1	$\begin{pmatrix} -1 \\ -1 \\ 0 \end{pmatrix}$	X_1	
R_6	$\begin{pmatrix} 0 & 1 & 0 \\ \bar{1} & 1 & 0 \\ 0 & 0 & 1 \end{pmatrix}$	$\begin{pmatrix} 1 \\ 0 \\ 0 \end{pmatrix}$	-1	1	$\begin{pmatrix} 0 \\ 1 \\ 0 \end{pmatrix}$	X_2	
R_7	$\begin{pmatrix} 1 & 0 & 0 \\ 1 & \bar{1} & 0 \\ 0 & 0 & 1 \end{pmatrix}$	$\begin{pmatrix} 1 \\ 0 \\ 0 \end{pmatrix}$	1	-1	$\begin{pmatrix} -1 \\ -1 \\ 0 \end{pmatrix}$	X_2	
R_8	$\begin{pmatrix} 0 & 1 & 0 \\ 1 & 0 & 0 \\ 0 & 0 & 1 \end{pmatrix}$	$\begin{pmatrix} 1 \\ 0 \\ 0 \end{pmatrix}$	-1	-1	$\begin{pmatrix} 0 \\ 1 \\ 0 \end{pmatrix}$	X_1	
R_9	$\begin{pmatrix} \bar{1} & 1 & 0 \\ 0 & 1 & 0 \\ 0 & 0 & 1 \end{pmatrix}$	$\begin{pmatrix} 1 \\ 0 \\ 0 \end{pmatrix}$	1	-1	$\begin{pmatrix} 1 \\ 0 \\ 0 \end{pmatrix}$	X_2	
R_{10}	$\begin{pmatrix} \bar{1} & 0 & 0 \\ \bar{1} & 1 & 0 \\ 0 & 0 & 1 \end{pmatrix}$	$\begin{pmatrix} 1 \\ 0 \\ 0 \end{pmatrix}$	-1	-1	$\begin{pmatrix} -1 \\ -1 \\ 0 \end{pmatrix}$	X_1	
R_{11}	$\begin{pmatrix} 0 & \bar{1} & 0 \\ \bar{1} & 0 & 0 \\ 0 & 0 & 1 \end{pmatrix}$	$\begin{pmatrix} 1 \\ 0 \\ 0 \end{pmatrix}$	1	-1	$\begin{pmatrix} 0 \\ 1 \\ 0 \end{pmatrix}$	X_2	
R_{12}	$\begin{pmatrix} 1 & \bar{1} & 0 \\ 0 & \bar{1} & 0 \\ 0 & 0 & 1 \end{pmatrix}$	$\begin{pmatrix} 1 \\ 0 \\ 0 \end{pmatrix}$	-1	-1	$\begin{pmatrix} 1 \\ 0 \\ 0 \end{pmatrix}$	X_1	

Table 2.6 Projection of basis vectors along (0 1 0) from Γ_3 for the $R(2a)$ site with $X_1 = (0\ 0\ z)$ and $X_2 = (0\ 0\ z{+}1/2)$. The last column is the final result of the projection which shows that for $R(2a)$ site, and for Γ_3, there is no component along the hexagonal **b** direction.

R_n	R	$\vec{\phi}_2$	$D_3^{1\star}$	det(R)	$D_3^{1\star} \times R_n \times det(R) \times \vec{\phi}_2$	$g_n X_1$	Sum of Basis Vectors for Each Atom Type
R_1	$\begin{pmatrix} 1 & 0 & 0 \\ 0 & 1 & 0 \\ 0 & 0 & 1 \end{pmatrix}$	$\begin{pmatrix} 0 \\ 1 \\ 0 \end{pmatrix}$	1	1	$\begin{pmatrix} 0 \\ 1 \\ 0 \end{pmatrix}$	X_1	For Atom TypeX_1
R_2	$\begin{pmatrix} 1 & \bar{1} & 0 \\ 1 & 0 & 0 \\ 0 & 0 & 1 \end{pmatrix}$	$\begin{pmatrix} 0 \\ 1 \\ 0 \end{pmatrix}$	-1	1	$\begin{pmatrix} 1 \\ 0 \\ 0 \end{pmatrix}$	X_2	$\begin{pmatrix} 0 \\ 0 \\ 0 \end{pmatrix}$
R_3	$\begin{pmatrix} 0 & \bar{1} & 0 \\ 1 & \bar{1} & 0 \\ 0 & 0 & 1 \end{pmatrix}$	$\begin{pmatrix} 0 \\ 1 \\ 0 \end{pmatrix}$	1	1	$\begin{pmatrix} -1 \\ -1 \\ 0 \end{pmatrix}$	X_1	For Atom TypeX_2
R_4	$\begin{pmatrix} \bar{1} & 0 & 0 \\ 0 & \bar{1} & 0 \\ 0 & 0 & 1 \end{pmatrix}$	$\begin{pmatrix} 0 \\ 1 \\ 0 \end{pmatrix}$	-1	1	$\begin{pmatrix} 0 \\ 1 \\ 0 \end{pmatrix}$	X_2	$\begin{pmatrix} 0 \\ 0 \\ 0 \end{pmatrix}$
R_5	$\begin{pmatrix} \bar{1} & 1 & 0 \\ \bar{1} & 0 & 0 \\ 0 & 0 & 1 \end{pmatrix}$	$\begin{pmatrix} 0 \\ 1 \\ 0 \end{pmatrix}$	1	1	$\begin{pmatrix} 1 \\ 0 \\ 0 \end{pmatrix}$	X_1	
R_6	$\begin{pmatrix} 0 & 1 & 0 \\ \bar{1} & 1 & 0 \\ 0 & 0 & 1 \end{pmatrix}$	$\begin{pmatrix} 0 \\ 1 \\ 0 \end{pmatrix}$	-1	1	$\begin{pmatrix} -1 \\ -1 \\ 0 \end{pmatrix}$	X_2	
R_7	$\begin{pmatrix} 1 & 0 & 0 \\ 1 & \bar{1} & 0 \\ 0 & 0 & 1 \end{pmatrix}$	$\begin{pmatrix} 0 \\ 1 \\ 0 \end{pmatrix}$	1	-1	$\begin{pmatrix} 0 \\ 1 \\ 0 \end{pmatrix}$	X_2	
R_8	$\begin{pmatrix} 0 & 1 & 0 \\ 1 & 0 & 0 \\ 0 & 0 & 1 \end{pmatrix}$	$\begin{pmatrix} 0 \\ 1 \\ 0 \end{pmatrix}$	-1	-1	$\begin{pmatrix} 1 \\ 0 \\ 0 \end{pmatrix}$	X_1	
R_9	$\begin{pmatrix} \bar{1} & 1 & 0 \\ 0 & 1 & 0 \\ 0 & 0 & 1 \end{pmatrix}$	$\begin{pmatrix} 0 \\ 1 \\ 0 \end{pmatrix}$	1	-1	$\begin{pmatrix} -1 \\ -1 \\ 0 \end{pmatrix}$	X_2	
R_{10}	$\begin{pmatrix} \bar{1} & 0 & 0 \\ \bar{1} & 1 & 0 \\ 0 & 0 & 1 \end{pmatrix}$	$\begin{pmatrix} 0 \\ 1 \\ 0 \end{pmatrix}$	-1	-1	$\begin{pmatrix} 0 \\ 1 \\ 0 \end{pmatrix}$	X_1	
R_{11}	$\begin{pmatrix} 0 & \bar{1} & 0 \\ \bar{1} & 0 & 0 \\ 0 & 0 & 1 \end{pmatrix}$	$\begin{pmatrix} 0 \\ 1 \\ 0 \end{pmatrix}$	1	-1	$\begin{pmatrix} 1 \\ 0 \\ 0 \end{pmatrix}$	X_2	
R_{12}	$\begin{pmatrix} 1 & \bar{1} & 0 \\ 0 & \bar{1} & 0 \\ 0 & 0 & 1 \end{pmatrix}$	$\begin{pmatrix} 1 \\ 0 \\ 0 \end{pmatrix}$	-1	-1	$\begin{pmatrix} -1 \\ -1 \\ 0 \end{pmatrix}$	X_1	

Table 2.7 Projection of basis vectors along (0 0 1) from Γ_3 for the $R(2a)$ site with $X_1 = (0\ 0\ z)$ and $X_2 = (0\ 0\ z{+}1/2)$. The last column is the final result of the projection which shows that for $R(2a)$ site, and for Γ_3, there is component along the hexagonal **c** direction and the moments are aligned in antiparallel direction.

R_n	R	$\vec{\phi}_3$	$D_3^{1\star}$	det(R)	$D_3^{1\star} \times R_n \times det(R) \times \vec{\phi}_3$	$g_n X_1$	Sum of Basis Vectors for Each Atom Type
R_1	$\begin{pmatrix} 1 & 0 & 0 \\ 0 & 1 & 0 \\ 0 & 0 & 1 \end{pmatrix}$	$\begin{pmatrix} 0 \\ 0 \\ 1 \end{pmatrix}$	1	1	$\begin{pmatrix} 0 \\ 0 \\ 1 \end{pmatrix}$	X_1	For Atom TypeX_1
R_2	$\begin{pmatrix} 1 & \bar{1} & 0 \\ 1 & 0 & 0 \\ 0 & 0 & 1 \end{pmatrix}$	$\begin{pmatrix} 0 \\ 0 \\ 1 \end{pmatrix}$	-1	1	$\begin{pmatrix} 0 \\ 0 \\ -1 \end{pmatrix}$	X_2	$\begin{pmatrix} 0 \\ 0 \\ 6 \end{pmatrix}$
R_3	$\begin{pmatrix} 0 & \bar{1} & 0 \\ 1 & \bar{1} & 0 \\ 0 & 0 & 1 \end{pmatrix}$	$\begin{pmatrix} 0 \\ 0 \\ 1 \end{pmatrix}$	1	1	$\begin{pmatrix} 0 \\ 0 \\ 1 \end{pmatrix}$	X_1	For Atom TypeX_2
R_4	$\begin{pmatrix} \bar{1} & 0 & 0 \\ 0 & \bar{1} & 0 \\ 0 & 0 & 1 \end{pmatrix}$	$\begin{pmatrix} 0 \\ 0 \\ 1 \end{pmatrix}$	-1	1	$\begin{pmatrix} 0 \\ 0 \\ -1 \end{pmatrix}$	X_2	$\begin{pmatrix} 0 \\ 0 \\ -6 \end{pmatrix}$
R_5	$\begin{pmatrix} \bar{1} & 1 & 0 \\ \bar{1} & 0 & 0 \\ 0 & 0 & 1 \end{pmatrix}$	$\begin{pmatrix} 0 \\ 0 \\ 1 \end{pmatrix}$	1	1	$\begin{pmatrix} 0 \\ 0 \\ 1 \end{pmatrix}$	X_1	
R_6	$\begin{pmatrix} 0 & 1 & 0 \\ \bar{1} & 1 & 0 \\ 0 & 0 & 1 \end{pmatrix}$	$\begin{pmatrix} 0 \\ 0 \\ 1 \end{pmatrix}$	-1	1	$\begin{pmatrix} 0 \\ 0 \\ -1 \end{pmatrix}$	X_2	
R_7	$\begin{pmatrix} 1 & 0 & 0 \\ 1 & \bar{1} & 0 \\ 0 & 0 & 1 \end{pmatrix}$	$\begin{pmatrix} 0 \\ 0 \\ 1 \end{pmatrix}$	1	-1	$\begin{pmatrix} 0 \\ 0 \\ -1 \end{pmatrix}$	X_2	
R_8	$\begin{pmatrix} 0 & 1 & 0 \\ 1 & 0 & 0 \\ 0 & 0 & 1 \end{pmatrix}$	$\begin{pmatrix} 0 \\ 0 \\ 1 \end{pmatrix}$	-1	-1	$\begin{pmatrix} 1 \\ 0 \\ 0 \end{pmatrix}$	X_1	
R_9	$\begin{pmatrix} \bar{1} & 1 & 0 \\ 0 & 1 & 0 \\ 0 & 0 & 1 \end{pmatrix}$	$\begin{pmatrix} 0 \\ 0 \\ 1 \end{pmatrix}$	1	-1	$\begin{pmatrix} 0 \\ 0 \\ -1 \end{pmatrix}$	X_2	
R_{10}	$\begin{pmatrix} \bar{1} & 0 & 0 \\ \bar{1} & 1 & 0 \\ 0 & 0 & 1 \end{pmatrix}$	$\begin{pmatrix} 0 \\ 0 \\ 1 \end{pmatrix}$	-1	-1	$\begin{pmatrix} 0 \\ 0 \\ 1 \end{pmatrix}$	X_1	
R_{11}	$\begin{pmatrix} 0 & \bar{1} & 0 \\ \bar{1} & 0 & 0 \\ 0 & 0 & 1 \end{pmatrix}$	$\begin{pmatrix} 0 \\ 0 \\ 1 \end{pmatrix}$	1	-1	$\begin{pmatrix} 0 \\ 0 \\ -1 \end{pmatrix}$	X_2	
R_{12}	$\begin{pmatrix} 1 & \bar{1} & 0 \\ 0 & \bar{1} & 0 \\ 0 & 0 & 1 \end{pmatrix}$	$\begin{pmatrix} 1 \\ 0 \\ 0 \end{pmatrix}$	-1	-1	$\begin{pmatrix} 0 \\ 0 \\ 1 \end{pmatrix}$	X_1	

Table 2.8 The six possible magnetic representations and the corresponding basis vectors of the crystallographic space group $P6_3cm$ associated with a magnetic unit cell same as the crystallographic unit cell. The atomic positions for rare-earths are given in brackets. $[z,+,-]$ depict z_{2a}, $+\mu^c_{2a}$, $-\mu^c_{2a}$, and z_{4b}, $+\mu^c_{4b}$, $-\mu^c_{4b}$ for the Wyckoff sites $R(2a)$ and $R(4b)$, respectively. $z_{2a} = 0.273$ and $z_{4b} = 0.231$ for Ho($2a$) and Ho($4b$), respectively. The symbol [0] labels no ordered magnetic moment at this site. The directions of magnetic moments for the Γ_5 and Γ_6 magnetic representations are denoted by [$\mathbf{e}_x$,$\mathbf{e}_y$,$\mathbf{e}_z$], where $\mathbf{e}_x$ and $\mathbf{e}_y$ are in the basal plane forming a 120 degree angle between them and the $\mathbf{e}_z$ vector is parallel to the 6-fold axis. The condition for a particular reflection is determined for the present experimental geometry and a dipole XRMS signal.

Magnetic representation	$R(2a)$		$R(4b)$				Magnetic Reflection	
	$\begin{pmatrix} 0 \\ 0 \\ z \end{pmatrix}$	$\begin{pmatrix} 0 \\ 0 \\ z+\frac{1}{2} \end{pmatrix}$	$\begin{pmatrix} \frac{1}{3} \\ \frac{2}{3} \\ z \end{pmatrix}$	$\begin{pmatrix} \frac{2}{3} \\ \frac{1}{3} \\ z \end{pmatrix}$	$\begin{pmatrix} \frac{1}{3} \\ \frac{2}{3} \\ z+\frac{1}{2} \end{pmatrix}$	$\begin{pmatrix} \frac{2}{3} \\ \frac{1}{3} \\ z+\frac{1}{2} \end{pmatrix}$	$(0\ 0\ l)$ l odd	$(h\ 0\ l)$ l odd
			moments in **c** direction					
$\Gamma_1 \equiv P6_3cm$	0	0	+	−	−	+	No	Yes
$\Gamma_2 \equiv P6_3c'm'$	+	+	+	+	+	+	No	No
$\Gamma_3 \equiv P6_3'cm'$	+	−	+	+	−	−	Yes	Yes
$\Gamma_4 \equiv P6_3'c'm$	0	0	+	−	+	−	No	No
			moments in **a-b** plane					
Γ_5 ($P6_3'$)	$[u\ v\ 0]$	$[u\ v\ 0]$	$[p\ q\ 0]$	$[r\ s\ 0]$	$[r\ s\ 0]$	$[p\ q\ 0]$	No	No iff p=r and q=s
Γ_6 ($P6_3$)	$[u\ v\ 0]$	$[\overline{u}\ \overline{v}\ 0]$	$[p\ q\ 0]$	$[r\ s\ 0]$	$[\overline{r}\ \overline{s}\ 0]$	$[\overline{p}\ \overline{q}\ 0]$	Yes	Yes

CHAPTER 3. X-RAY RESONANT MAGNETIC SCATTERING OF $R\mathrm{MnO_3}$ COMPOUNDS IN ZERO FIELD

3.1 Magnetic Ordering in $\mathrm{HoMnO_3}$ in Zero Field

3.1.1 Introduction

The last few years have seen a flurry of research activity in the field of multiferroic magnetoelectrics, compounds which are both magnetic and ferroelectric within the same phase. The physics behind the coupling between ferroelectricity and magnetism is of fundamental interest [9] and this phenomenon has been observed in several rare-earth (R) manganites including hexagonal $R\mathrm{MnO_3}$[9, 51] and orthorhombic $R\mathrm{MnO_3}$ and $R\mathrm{Mn_2O_5}$[20, 22]. Hexagonal $\mathrm{HoMnO_3}$ has been recently re-discovered as a multiferroic material. Below $T = 875$ K[31], $\mathrm{HoMnO_3}$ is ferroelectric with $P6_3cm$ symmetry and a polarization of $P_\mathrm{C} = 5.6\mu\mathrm{C}cm^{-2}$ along the hexagonal **c** axis.[31] The variation of P_C with temperature is small.[31] The Mn^{3+} moments order antiferromagnetically below the Néel temperature, $T_\mathrm{N} \sim 76$ K.[9, 49] Additionally, it has been proposed that the Ho^{3+} moments order antiferromagnetically below $T_\mathrm{SR} \sim 40$ K, coincident with a spin re-orientation of the Mn^{3+} moments within the **a-b** plane.[9, 47] Below 4.5 K there is a re-arrangement of the Ho^{3+} order and second spin re-orientation of the Mn^{3+} moments.[9, 47] Different types of magnetic ordering for Ho^{3+} have been proposed and different transition temperatures have been claimed based on magnetoelectric measurements,[44] optical second harmonic generation (SHG)[46, 87] and neutron diffraction experiments[41, 47, 48].

To resolve the controversies regarding the nature of magnetic ordering of Ho^{3+} below 40 K, we performed x-ray resonant magnetic scattering (XRMS) studies of this compound. XRMS is element specific allowing a direct determination of the magnetic order of the rare-earth R^{3+}

component, and is complementary to neutron scattering measurements. More specifically, in neutron scattering experiments on a multicomponent magnetic system, a magnetic structure must first be assumed and the ordered moments of the two sublattices are extracted from intensities of a number of reflections. In the case of $HoMnO_3$, the neutron magnetic signal is dominated by Mn^{3+} moments since the Mn^{3+} carries a fully ordered moment and the Ho^{3+} contribution must be determined from a careful fitting process together with the Mn^{3+} contribution. In this sense, an XRMS study of $HoMnO_3$ is more reliable in determining the magnetic structure of Ho^{3+} and the magnetic order parameter.

Magnetic structure determination is a pre-requisite to the understanding of any coupling between ferroelectricity and magnetism. Lorenz *et al.*[51], for example, pointed out that the coupling between the in plane magnetization of Mn^{3+} moments and the **c** axis polarization is not allowed by symmetry. In contrast **c** axis magnetic moments can directly couple to the polarization. Therefore, it is very important to know the moment direction of Ho^{3+} and the magnetic symmetry in the ordered phase in order to understand any coupling between ferroelectricity and magnetism.

3.1.2 Experimental Details

Single crystals of hexagonal $R\mathrm{MnO_3}$ (R = Ho, Er, and Dy) were grown at Ames Laboratory by floating zone technique with the aid of an optical image furnace (Model FZ-T-4000-H-VI-VPM-PC from Crystal Systems INC). High pure R_2O_3 oxides were dried at 950°C in air for 12 hours before weighing. The starting materials (R_2O_3 and Mn_2O_3) were weighted after pretreatment and mixed in an agate mortar. Then the mixture was fired at 900°C, 1000°C, 1100°C, and 1150°C, respectively, with intermediate grinding. The well fired powder was then compressed hydrostatically in a rubber tube into rods with 5 mm diameter and 80 mm length. The rods were then heated in air at 1250°C for 24 hours. The crystal growths of $HoMnO_3$ and $ErMnO_3$ were performed in flowing air. The growth rate was optimized to be 3 mm/h while the lower and upper shafts of image furnace rotate in opposite direction during the growth. The growth of $DyMnO_3$ was performed in flowing argon. The growth rate was chosen to be 4

mm/h. A lower growth rate leads to the crystallization of orthorhombic phase, while a faster growth leads to poor crystallinity of grown crystals. Growth of $DyMnO_3$ in flowing air always results in orthorhombic $DyMnO_3$ regardless of the growth rate.

For the XRMS measurements, a single crystal of approximate dimension of $8\times4\times1$ mm^3 was selected with a surface polished perpendicular to the **c** axis for $HoMnO_3$. The XRMS experiments were performed on the 6ID-B beamline in the MUCAT sector at the Advanced Photon Source at the Ho L_{III} resonance ($E = 8.071$ keV for Ho). The incident radiation was linearly polarized perpendicular to the vertical scattering plane (σ-polarized) with a spatial cross-section of 1 mm (horizontal) $\times$ 0.2 mm (vertical). In this configuration, the resonant magnetic scattering rotates the plane of linear polarization into the scattering plane ($\pi^{'}$-polarization). In contrast, charge scattering does not change the polarization of the scattered photons (σ-$\sigma^{'}$ scattering). A Pyrolytic graphite PG (0 0 6) analyzer was used as a polarization and energy analyzer to suppress the charge as well as fluorescence background relative to the magnetic scattering signal.

For the hexagonal $R\text{MnO}_3$ compounds with space group $P6_3cm$, and lattice constants $a \approx 6.12$ Å and $c \approx 11.4$ Å, reciprocal lattice points (h 0 l) with l even are allowed charge reflections. Based on our calculations (see Table 2.8), we searched for (0 0 l) and (h 0 l)[1] magnetic reflections with l odd to distinguish between the different proposed models for the magnetic order of Ho^{3+}. Thus, the sample was mounted at the end of the cold-finger of a displex cryogenic refrigerator with the $\mathbf{a}^\star$-$\mathbf{c}^\star$ reciprocal lattice plane coincident with the scattering plane. Although these reflections are forbidden for charge reflections they can be strongly contaminated by multiple charge scattering. However, the intensity of the multiple scattering is highly sensitive to both the incident beam energy and the azimuth angle ψ. We were able to minimize multiple scattering contribution at the resonant energy through a judicious choice of the azimuth angle.[88]

[1]For off-specular reflections, positive (negative) h in (h 0 l) reflections implies outgoing angle (the angle between the outgoing x-rays and sample surface) is greater (less) than that of the incident angle (the angle between incoming x-rays and sample surface).

3.1.3 Proposed Magnetic Structures

Since the magnetic unit cell is the same as the chemical unit cell[41] we can describe the different magnetic structures with magnetic representations assuming dominant second order terms in the Hamiltonian.[73] The different magnetic representations allowed for the crystallographic space group $P6_3cm$ are shown Table 2.8 and the resulting magnetic structure factors (related to the measured intensities) are detailed in the section 2.1.3.3. Prior to this work, there were three proposed models for the Ho^{3+} order. We will briefly discuss the different models and their consequences for our XRMS measurements:

Model 1: Sugie *et al.*[44] proposed the magnetic representation Γ_6 from symmetry consideration of magnetoelectric measurements. The magnetic ordering temperature of Ho^{3+} is below 5 K and the Ho^{3+} moments are non-collinearly aligned in the **a-b** plane. For this case, the structure factor analysis in Chapter 2 concludes that we should observe less intensity for $(h\ 0\ l)$ reflections compared to $(\overline{h}\ 0\ l)$ with l odd.

Model 2: Muñoz *et al.*[41] proposed the magnetic representation Γ_2 for the Mn^{3+} order in the temperature range 76K>T>44.6 K from their neutron powder diffraction study. They proposed a spin reorientation of Mn^{3+} at 44.6 K and the representation Γ_1 for the Mn^{3+} order in the temperature range 44.6 K>T>1.7 K. Furthermore, they proposed the same magnetic representation Γ_1 for the Ho^{3+} order in the temperature range 24.6 K>T>1.7 K. According to this model, at low temperature ($T \leq 24.6$ K), only Ho^{3+} moments at the $(4b)$ Wyckoff site are ordered collinearly along the **c** direction, and the Ho^{3+} moments at the $(2a)$ Wyckoff site are in a paramagnetic state. In this representation, the Ho$(4b)$ moments are antiferromagnetically correlated in **c** direction as well as in the **a-b** plane. If this model for the Ho^{3+} order is correct, then we should observe zero intensity for $(0\ 0\ l)$ reflections with l odd and non-zero intensity for $(h\ 0\ l)$ reflections with l odd and $h \neq 3n$, n integer (see Table 2.8).

Model 3: Lonkai *et al.*[9, 46, 47, 87] proposed the magnetic representation Γ_4 for the Mn^{3+} order between $T_N = 76$ K and $T_{SR} = 37$ K based on neutron powder diffraction and optical second harmonic generation (SHG). For 37 K>T>5 K they proposed the magnetic representation Γ_3 for both the Mn^{3+} and Ho^{3+} moments. According to their measurements, Mn^{3+} undergoes

another spin reorientation below 5 K and Ho^{3+} re-orders according to the representation Γ_1. Recently, Brown and Chatterji[48] also proposed the magnetic representation Γ_4 for Mn^{3+} order above the spin reorientation at T_{SR} from their neutron diffraction and polarimetric study. In the temperature range 37K>T>2 K, they proposed the magnetic representation Γ_3 for both the Mn^{3+} and the Ho^{3+} order and concluded that the Ho($2a$) and the Ho($4b$) sites carry unequal moments below 37 K and there is no phase transition below 5 K. However, their results do not show clearly the transition temperature for the Ho^{3+} order and the developing order parameter over the full temperature range. If the model proposed by Lonkai *et al.*[9, 46, 47, 87] and by Brown and Chatterji[48] is correct, then below $T_{SR} = 37$ K, we should observe non-zero magnetic intensity for (0 0 l) reflections with l odd.

As mentioned above, neutron diffraction is not particularly sensitive to the Ho^{3+} sublattice as the magnetic signal is dominated by Mn^{3+} moments. The ordered component of Ho^{3+} moments is small compared to the Mn^{3+} moments although the saturated moment of Ho^{3+} is quite large ($\sim 10\ \mu_B$). Further, SHG is unable to distinguish between different magnetic sublattices. This motivated an element specific x-ray resonant magnetic scattering (XRMS) to find the correct magnetic representation for the Ho^{3+} order.

3.1.4 Experimental Results and Discussion

Observation of magnetic resonant scattering and characterization of the transition temperatures

Figure 3.1 shows the magnetic susceptibility of a $HoMnO_3$ single crystal, measured using a quantum design superconducting quantum interference device (SQUID) magnetometer. The inset to Fig. 3.1 shows kinks in the magnetic susceptibility at 40 and 4.5 K, respectively. Magnetic susceptibility measured by Lorenz *et al.*[51] on a flux grown sample shows kink at 33 and 4.5 K, respectively. Although the shape of the kink is very similar, the transition temperatures are slightly different between flux grown and floating zone grown samples. The samples grown using floating zone by Vajk *et al.*[89] show very similar transition temperatures with the samples used in the present work. The difference observed in transition temperatures may

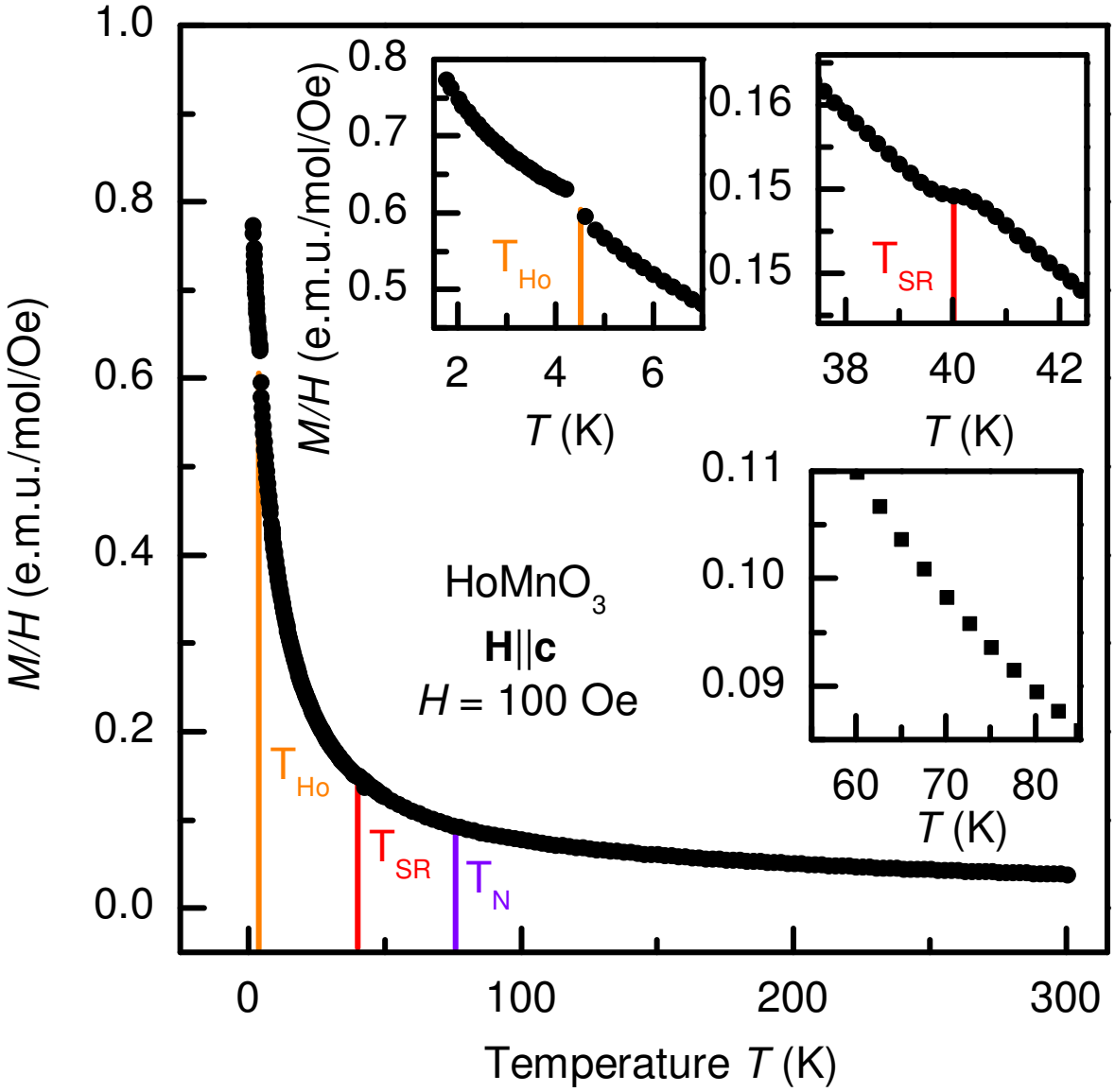

Figure 3.1 Magnetic susceptibility M/H of the $HoMnO_3$ single crystal. The temperature dependence of the susceptibility was measured on heating the zero-field cooled sample in a field of 100 Oe applied parallel to the **c** axes. Inset shows details of the magnetic susceptibility near the transition temperatures of the Ho^{3+} order (upper two insets) and the Mn^{3+} order (lower inset). No signature in the M/H data could be found at the ordering temperature of Mn^{3+}.

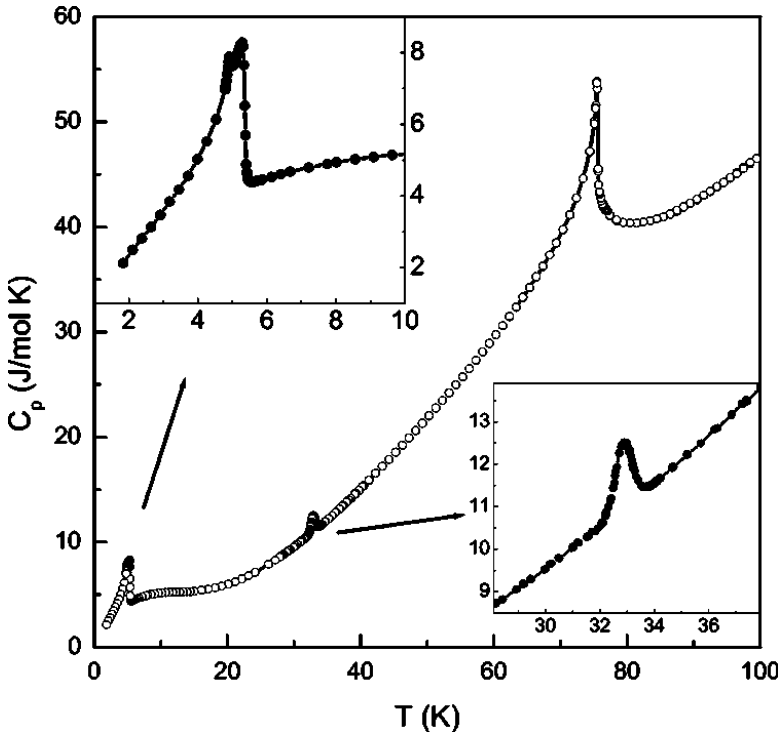

Figure 3.2 Specific heat of $HoMnO_3$ at zero magnetic field. The λ-type anomaly at T_N is followed by two additional peaks at T_{SR} and T_{Ho}, enlarged in the lower right and upper left insets, respectively. After Ref. [90]

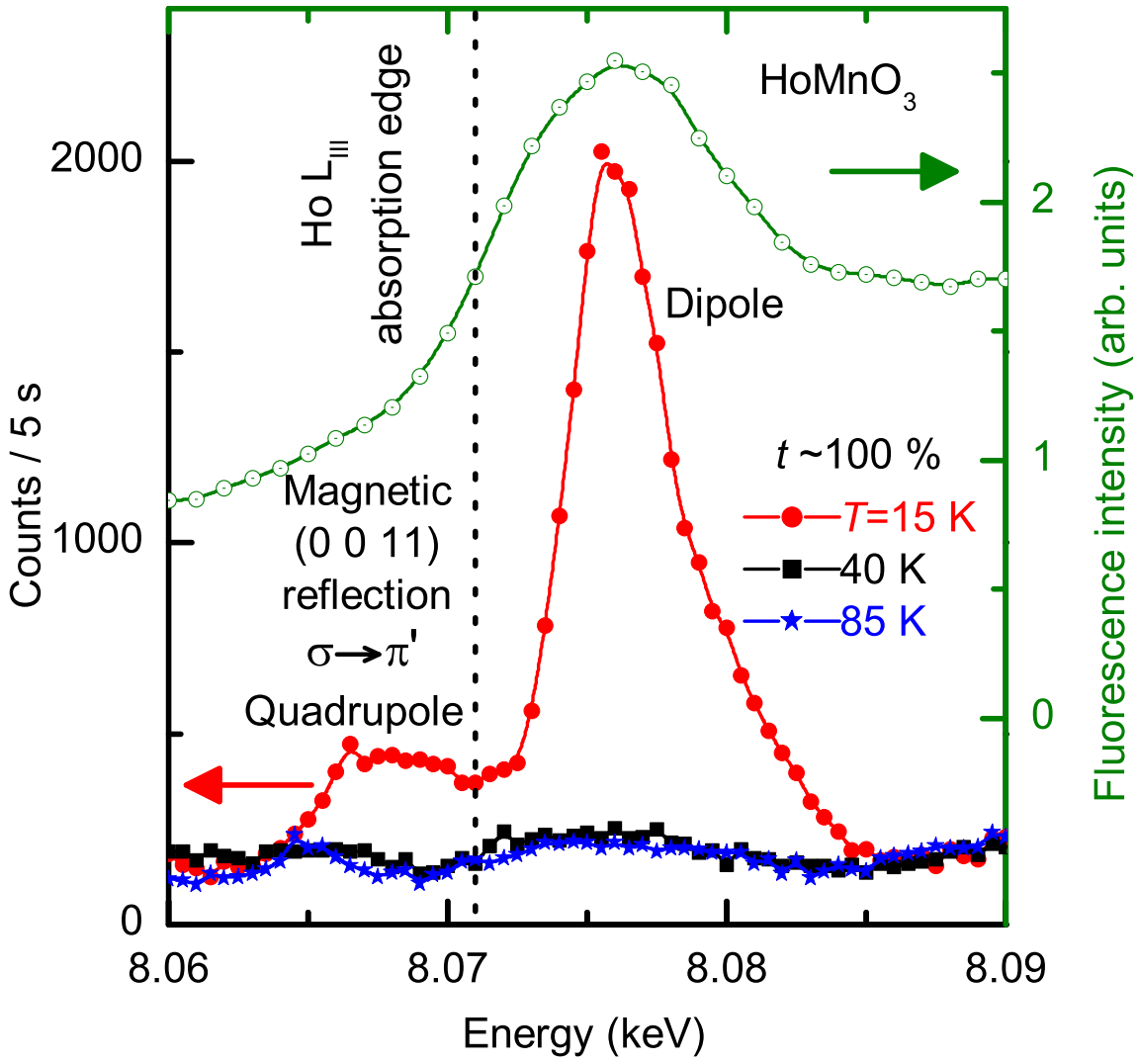

Figure 3.3 Energy scans of the magnetic (0 0 11) reflection and of the fluorescence signal through the Ho L_{III} absorption edge. The energy scan of the (0 0 11) was measured with 100 % beam transmission ($t = 100\%$). The dashed line indicates the Ho L_{III} absorption edge as determined from the inflection point of the observed fluorescence intensity measured at $T = 15$ K.

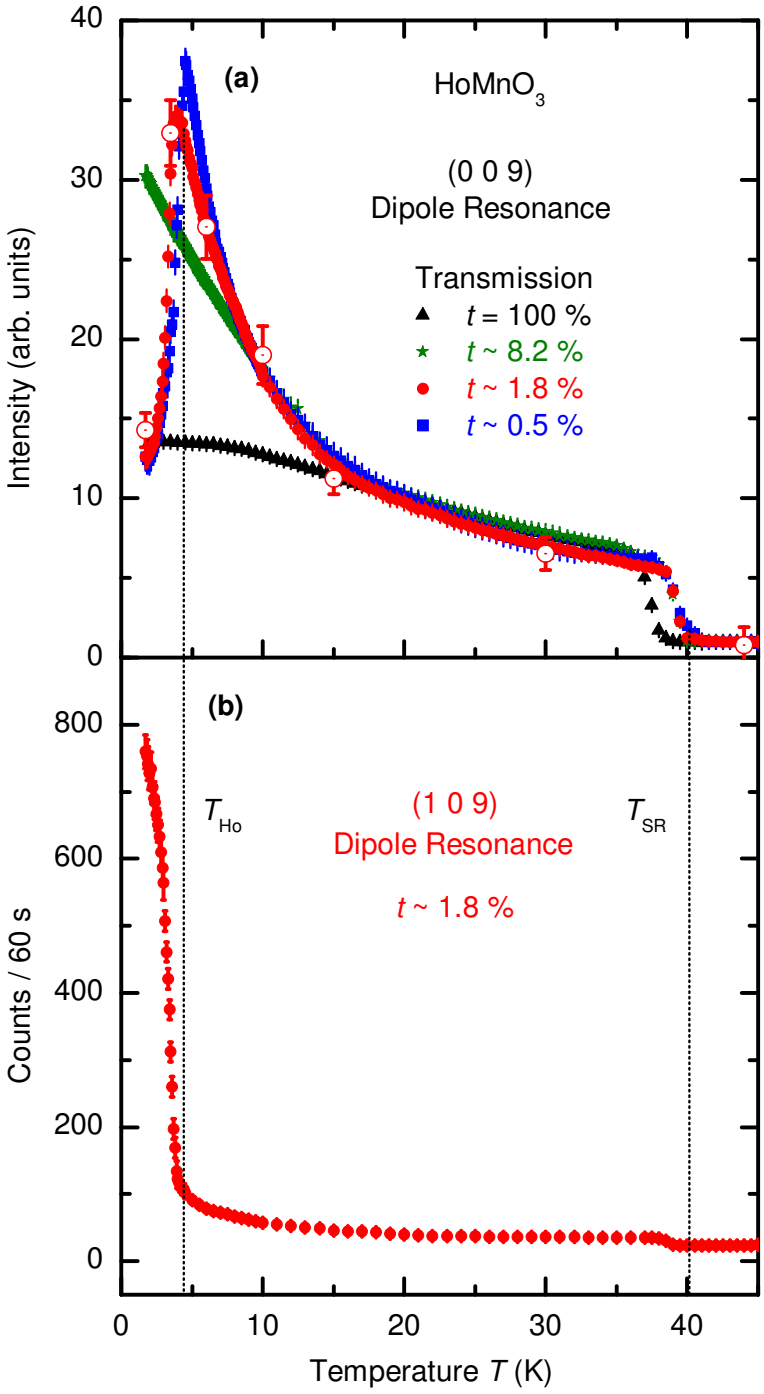

Figure 3.4 (a) Temperature dependence of the peak intensity of the dipole resonance for the (0 0 9) reflection with different attenuation of the incident beam. The open symbols are the measured integrated intensities at selected temperatures using an attenuator with a transmission of t∼1.8%. (b) Temperature dependence of the peak intensity of the dipole resonance for the (1 0 9) reflection. In both panels (a) and (b), we show the peak intensity after binning for clarity.

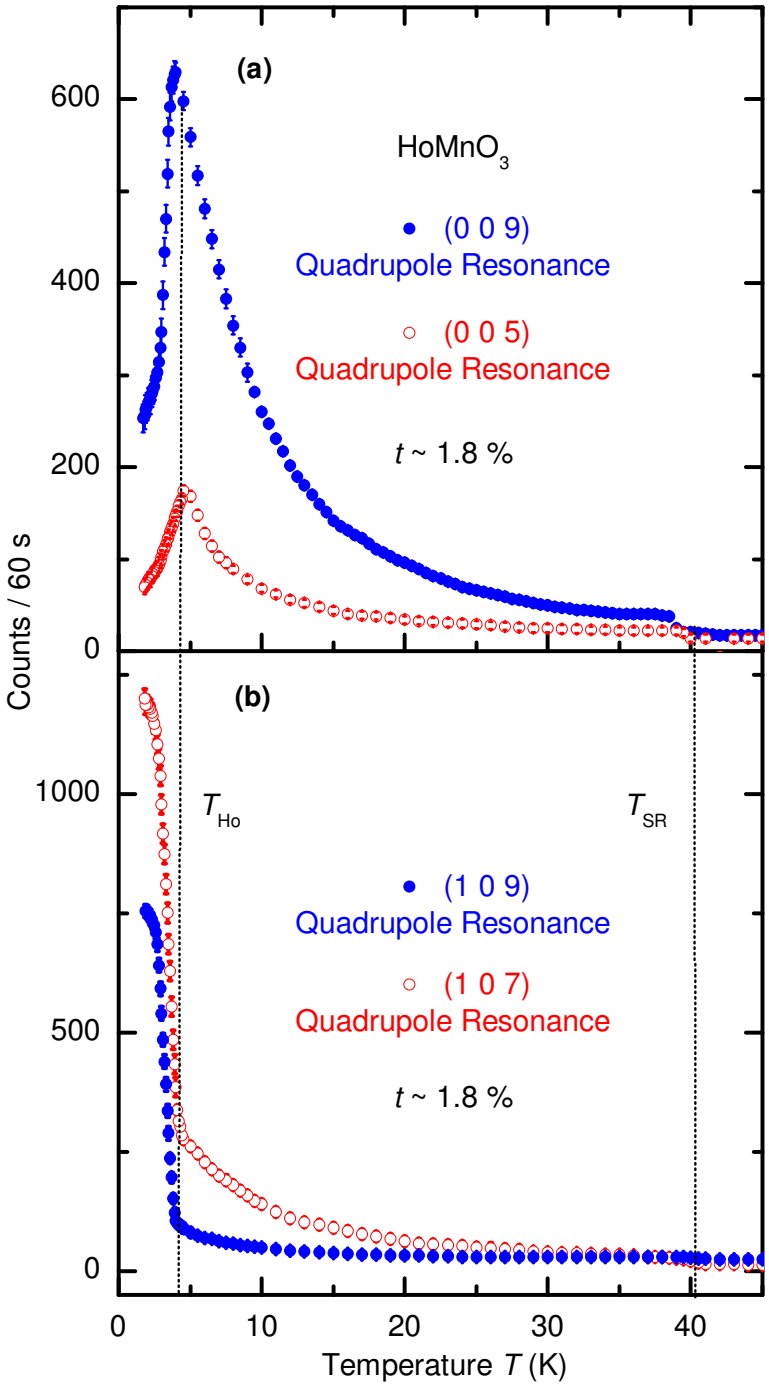

Figure 3.5 (a) Temperature dependence of the quadrupole resonance intensity for the specular (0 0 9) and (0 0 5) reflections and (b) off-specular (1 0 9) and (1 0 7) reflections. Binned data with appropriate error bars have been shown in both panels for clarity.

be due internal stress and/or nonstoichiometric oxygen content mentioned by Vajk *et al.*[89] Specific heat data measured by Lorenz *et al.* [90] on a flux grown sample shown in Fig. 3.2 show phase transitions at 76, 33 and 4.5 K respectively. In the following, we specify the high temperature phase (HTP) between $40 \leq T \leq 76$ K, intermediate temperature phase (ITP) between $40 \geq T \geq 4.5$ K and low temperature phase (LTP) below 4.5 K, respectively.

With the sample oriented so that the $\mathbf{a}^\star$-$\mathbf{c}^\star$ reciprocal plane was coincident with the scattering plane, magnetic intensity was found at the position (0 0 11) which is nominally forbidden for charge scattering. To confirm the resonant behavior of this feature, we performed energy scans through the Ho L_{III} absorption from 6 K to 85 K (which is above the Néel temperature of the Mn^{3+} order) and observed two resonance peaks, one below the absorption edge and one above the absorption edge as shown in Fig. 3.3. We interpret these peaks as quadrupole and dipole resonances because the quadrupole resonance ($E2$, from the $2p$-to-$4f$ states) generally appears below the absorption edge whereas the dipole resonance ($E1$, from the $2p$-to-$5d$ states) appears above the absorption edge.[60] No resonant signal could be found above T_{SR}.

Generally, sample heating by the intense incident x-ray beam is very strong for insulating materials like $HoMnO_3$, particularly at low temperatures. Therefore, to characterize the beam heating effect and to determine the transition temperatures of the Ho^{3+} order, we measured the peak intensity of dipole resonance for the (0 0 9) reflection with different attenuators as shown in Fig. 3.4(a). It is clear from Fig. 3.4(a) that significant beam heating ($\sim$ 2 K) is present even at $T = 40$ K with transmission $t = 100\%$. The beam heating effect becomes severe at temperature below 15 K and significant attenuation of the incident beam is necessary to reduce the beam heating. Since the normalized peak intensity and characteristic temperatures (40 K and 4.5 K) remain almost same using attenuators with transmissions t of $\sim$1.8% and $\sim$ 0.5%, other temperature dependent measurements were performed using t $\sim$1.8%.[2]

Generally, the integrated intensity of the scattering should be measured for this study. However, in this instance, measurements of the peak intensity suffice since both the peak position and full width half maximum remain constant over the investigated temperature

[2]Since the energy scan shown in Fig. 3.3 was measured with t=100%, the actual sample temperature could be slightly higher

range. Nevertheless, we did measure θ-scans (rocking curves) at selected temperatures and determined the integrated intensity for both the dipole and quadrupole resonances by fitting these θ-scans with a Lorentzian function. The measurement of the dipole resonance intensity using an attenuator with a transmission of $\sim$1.8%, as shown in Fig. 3.4(a), clearly indicates that the integrated intensity and peak intensity differ simply by a scale factor and, therefore, justifies measuring the peak intensity for temperature dependent studies. Figure 3.4(b) shows the temperature dependence of the dipole resonance for another characteristic reflection (1 0 9) showing the same transition temperatures.

The temperature dependence of the quadrupole resonance for both the (0 0 9) and (1 0 9) reflections is shown in Fig. 3.5 and is similar to that found for the dipole resonant intensity in Fig. 3.4. Below 40 K, both the dipole and quadrupole intensities increase gradually with decreasing temperature. The observation of the quadrupole intensity below 40 K clearly proves that the Ho^{3+} moments order magnetically just below 40 K because the quadrupole resonance is directly related to the ordered $4f$ magnetic moment of Ho^{3+}.[60] Furthermore, the temperature of the onset of magnetic Ho^{3+} order agrees well with the kink in magnetization data as shown in Fig. 3.1 and the Mn^{3+} spin re-orientation transition as found by Vajk *et al.*[49] Below 4.5 K the intensities of specular reflections (0 0 9) and (0 0 5) decrease but the intensities of the off-specular reflections, (1 0 9) and (1 0 7), increase dramatically. Therefore, the temperature dependent measurements indicate that the Ho^{3+} moments order antiferromagnetically below 40 K and signal a change of the magnetic structure below 4.5 K.

Magnetic structure in the intermediate temperature phase (40 K $\geq T \geq$ 4.5 K)

We now turn to the analysis of the magnetic structure in the intermediate temperature range from 40 K down to 4.5 K (intermediate temperature phase, ITP). In order to determine the magnetic representation we must look into the details of six magnetic representations that are possible for the crystallographic space group $P6_3cm$ that are listed in the Table 2.8. The moment directions are denoted by $+/-$ for moments aligned along the hexagonal **c** direction, and with the basis vectors for moments lying in the **a-b** plane.

We see from Table 2.8 that the magnetic moments are aligned either along the hexagonal

c direction (Γ_1, Γ_2, Γ_3, Γ_4) or in the **a-b** plane (Γ_5, Γ_6). It should be noted that from the anisotropic magnetic susceptibility[90, 91] data, the moment direction of Ho^{3+} is not clear. As a first attempt to determine the moment direction, we measured the off-specular (3 0 9) and ($\overline{3}$ 0 9) reflections. Except for the angular factors, the expression for the magnetic structure factor ($|F_m|^2$) is same for these two reflections (see section 2.1.3.3). It is the angular dependence in the structure factor that provides strong sensitivity to the moment direction. For the dipole resonance $f_{E1}^{\mathrm{XRMS}} \propto \mathbf{k_f} \cdot \boldsymbol{\mu}$,[64, 80] in the $\sigma \rightarrow \pi^{'}$ channel, where $\mathbf{k_f}$ and $\boldsymbol{\mu}$ are the wave vector of the scattered photons and the magnetic moment, respectively. Therefore, for moments aligned along the **c** direction the magnetic intensity $I \propto |F_m|^2 \propto \sin^2(\theta + \alpha)$ whereas for the moments in the **a-b** plane $I \propto |F_m|^2 \propto \cos^2(\theta + \alpha)$. Here, α is the angle that the scattering vector $\mathbf{Q}(=\mathbf{k_f} - \mathbf{k_i})$ makes with the crystallographic **c** direction perpendicular to the surface of the sample. α is positive (negative) for larger (smaller) angles for the outgoing beam with respect to the sample surface. The calculated ratio is $\frac{I(3\ 0\ 9)}{I(\overline{3}\ 0\ 9)} = 86.3$ and 0.32, for moments along the **c** direction and in the **a-b** plane, respectively. The experimentally observed ratio is 76 ± 14. Therefore, the magnetic moments are primarily aligned in the hexagonal **c** direction.

One should note that both Ho sites may not be in the same magnetic representation. However, one of the sites must be in the Γ_3 representation because only this representation yields non-zero intensity for (0 0 l) reflections with l odd and carries moments in **c** direction (see Table 2.8). Therefore, either both Ho sites are ordered magnetically according to the representation Γ_3 or according to a combination of magnetic representations Γ_3 and any of the other magnetic representations.

We will first discuss the possibility that both Ho sites are in the magnetic representation Γ_3. The intensity for a particular reflection can be written as:

$$I = SAL|F_m|^2 \tag{3.1}$$

where S is arbitrary scaling factor, $A = \frac{\sin(\theta+\alpha)}{\sin\theta\cos\alpha}$ is the absorption correction and $L = \frac{1}{\sin 2\theta}$ is the Lorentz factor. $|F_m|$ is the modulus of the magnetic structure factor, calculated for the different magnetic representations in section 2.1.3.3. For specular (0 0 l) reflections, $\alpha = 0$ and Eq. 3.1 becomes,

$$I_{dipole} = S \tan\theta[\mu_{2a}^2 + 4\mu_{4b}^2 + 4\mu_{2a}\mu_{4b}\cos\{2\pi(z_{2a} - z_{4b})l\}] \tag{3.2}$$

Additionally,

$$\frac{\sin^2\theta}{\sin 2\theta} = \frac{1}{2}\tan\theta = \frac{\lambda}{2}\frac{l}{\sqrt{4c^2 - \lambda^2 l^2}} \tag{3.3}$$

So, Eq. (2) can be re-written as:

$$I_{dipole} = \frac{S'l}{\sqrt{4c^2 - \lambda^2 l^2}}[r^2 + 4 + 4r\cos\{2\pi(z_{2a} - z_{4b})l\}] \tag{3.4}$$

where S' is the arbitrary scaling factor, λ is the x-ray wavelength, $z_{2a} = 0.273$, $z_{4b} = 0.231$[41] are the z positions of the Ho^{3+} ions, and r $(= \frac{\mu_{2a}}{\mu_{4b}})$ is the ratio between the Ho^{3+} moments at the $(2a)$ and $(4b)$ Wyckoff sites. We note that there are two free parameters in Eq. 3.4, S' and r. Similarly, for the quadrupole resonance we can write (see Eq. 2.55)

$$I_{quadrupole} = S'' I_{dipole}[1 + B - \frac{\lambda^2 l^2}{4c^2}(1 + 2B)]^2 \tag{3.5}$$

S'' is again an arbitrary scaling factor and B $(=\frac{F_{E2}^{(3)}}{F_{E2}^{(1)}})$ is the ratio of the coefficients in the quadrupole resonance amplitude.[64] In addition to the parameters S'' and r, Eq. 3.5 has one more free parameter B.

The dipolar and quadrupolar angular dependence at 12 K was fit with Eqs. 3.4 & 3.5, and are shown in Figs. 3.6 & 3.7, respectively. The best fit of the data correspond to $r = -2 \pm 0.5$ for both the dipole and quadrupole resonance at 12 K, which is consistent with recent neutron data.[48] We obtained $B = -0.06(5)$ for the quadrupole resonance, at 12 K. We note here that the value of the parameter B differs by an order of magnitude from the expected one-electron calculations and the sign is also different.[69] Gibbs *et al.*[61] also concluded that one electron calculations are not sufficient for quantitative comparison with the experimentally fit parameter values obtained from the resonance enhancements in Ho metal. More sophisticated calculations of the electronic structures are required for comparison.

Though the fits are not sensitive to small changes in the ratio r, we can conclude that both the Ho$(2a)$ and Ho$(4b)$ sites carry an ordered magnetic moment (the curve with r=0 corresponds to a moment carried by either Ho$(2a)$ or Ho$(4b)$) and the moment size at the

two sites are unequal (e. g. r=−1, corresponds to equal moment size but antiferromagnetic correlations within the plane).

If one of the Ho^{3+} sites belongs to Γ_3 and the *other* site is in one of the *other* representations (Γ_1, Γ_2, Γ_4, Γ_5), then the Ho^{3+} moments in the *other* site do not contribute to the intensity of (0 0 l) reflections according to Table 2.8. Thus,

$$I_{dipole} = \frac{Sl}{\sqrt{4c^2 - \lambda^2 l^2}} \tag{3.6}$$

which corresponds to Eq. 3.4 with r=0 and can not reproduce the observed intensity for small angles for dipolar angular dependence. For the quadrupole resonance Eq. 3.5 becomes,

$$I_{quadrupole} = I_{dipole}(r = 0)[1 + B - \frac{\lambda^2 l^2}{4c^2}(1 + 2B)]^2 \tag{3.7}$$

The quadrupolar angular dependence was fit with the above equation with two free parameters, S and B. The best fit curve, shown in Fig. 3.7 with $B = -0.4$, does not reproduce the observed angular dependence of the intensity. Therefore, the combination of Γ_3 with any of the representations (Γ_1, Γ_2, Γ_4, Γ_5) can not explain the observed angular dependence.

On the other hand if one of the Ho^{3+} sites is in Γ_3, and the other is in Γ_6, then the calculated intensity for dipolar resonance is proportional to $D\tan\theta + E\cot\theta$ where D and E are two arbitrary positive constants (we assume an equal population of possible magnetic domains[48]). While the $\tan\theta$ term comes from the product of the Lorentz factor (L=$\frac{1}{\sin 2\theta}$) and the angular form factor ($\sin^2\theta$) for moments along the **c** direction (as in the magnetic representation Γ_3), the $\cot\theta$ term comes from the product of L and the angular form factor ($\cos^2\theta$) for moments in the **a-b** plane (as in the magnetic representation Γ_6)[see Eqs. 2.48 & 2.49]. Since the $E\cot\theta$ term would add even more intensity for small angles to the $r = 0$ curve ($S\tan\theta$), we can not reproduce the observed intensity for small angles. For the quadrupole resonance and for such a combination of magnetic representations, the equation for calculated intensity is much more complex and contains more than two free parameters. Therefore, we will rely on the angular dependence of dipole resonance to exclude the combination of Γ_3 and Γ_6 in the ITP.

In summary, measurements of off-specular reflections confirm that magnetic moments are primarily along the **c** direction. The observed angular dependence ensures that the both Ho

sites are in the same magnetic representation Γ_3 in the ITP. At 12 K, the ratio between the magnetic moments of the Ho($2a$) and Ho($4b$) Wyckoff site is ~ -2. The '$-$' implies that moments on the Ho($2a$) site are antiferromagnetically aligned with the moments on the Ho($4b$) site in the **a-b** plane. The resulting magnetic structure is shown in Fig. 3.8(b).

Temperature dependence of the magnetic moment in the intermediate temperature phase

Although, the dipole intensity vanishes above 40 K, there is a discontinuity in the dipole resonance intensity and a small, but observable, discontinuity in the quadrupole intensity near 40 K, as evident from Figs. 3.4 (a) & 3.5 (a). Below 40 K, we see a gradual increase with decreasing temperatures in the ITP.

The temperature dependence of magnetic moments at both Ho sites can be derived from the temperature dependence of a pair of reflections, (0 0 9) and (1 0 9). We will first briefly outline the procedure for obtaining the temperature dependence of magnetic moments. For the magnetic representation Γ_3, we can write:

$$\frac{I_{(0\ 0\ 9)}(T)}{I_{(1\ 0\ 9)}(T)} = Sf[r(T)] \tag{3.8}$$

where S is a scaling factor and r is the ratio of magnetic moments at the two Ho sites. The scaling factor, S, can be determined since r is known at 6 K from our angular dependent measurements. Hence, the temperature dependence of the ratio of magnetic moments [*r(T)*] can be determined. Again,

$$I_{(0\ 0\ 9)}(T) = K\mu_{4b}^2 f[r(T)] \tag{3.9}$$

Therefore,

$$\begin{aligned} \mu_{4b}(T) &= Cf[r(T), I_{(0\ 0\ 9)}(T)] \\ \mu_{2a}(T) &= r(T)\mu_{4b}(T) \end{aligned} \tag{3.10}$$

where K and C are constants that can not be determined because the absolute value of the magnetic moment is unknown at any temperature. However, the normalized temperature dependence $[\frac{\mu_{4b}(T)}{\mu_{4b}(6K)}]$ and $[\frac{\mu_{2a}(T)}{\mu_{4b}(6K)}]$ can be determined since *r(T)* is known at 6 K.

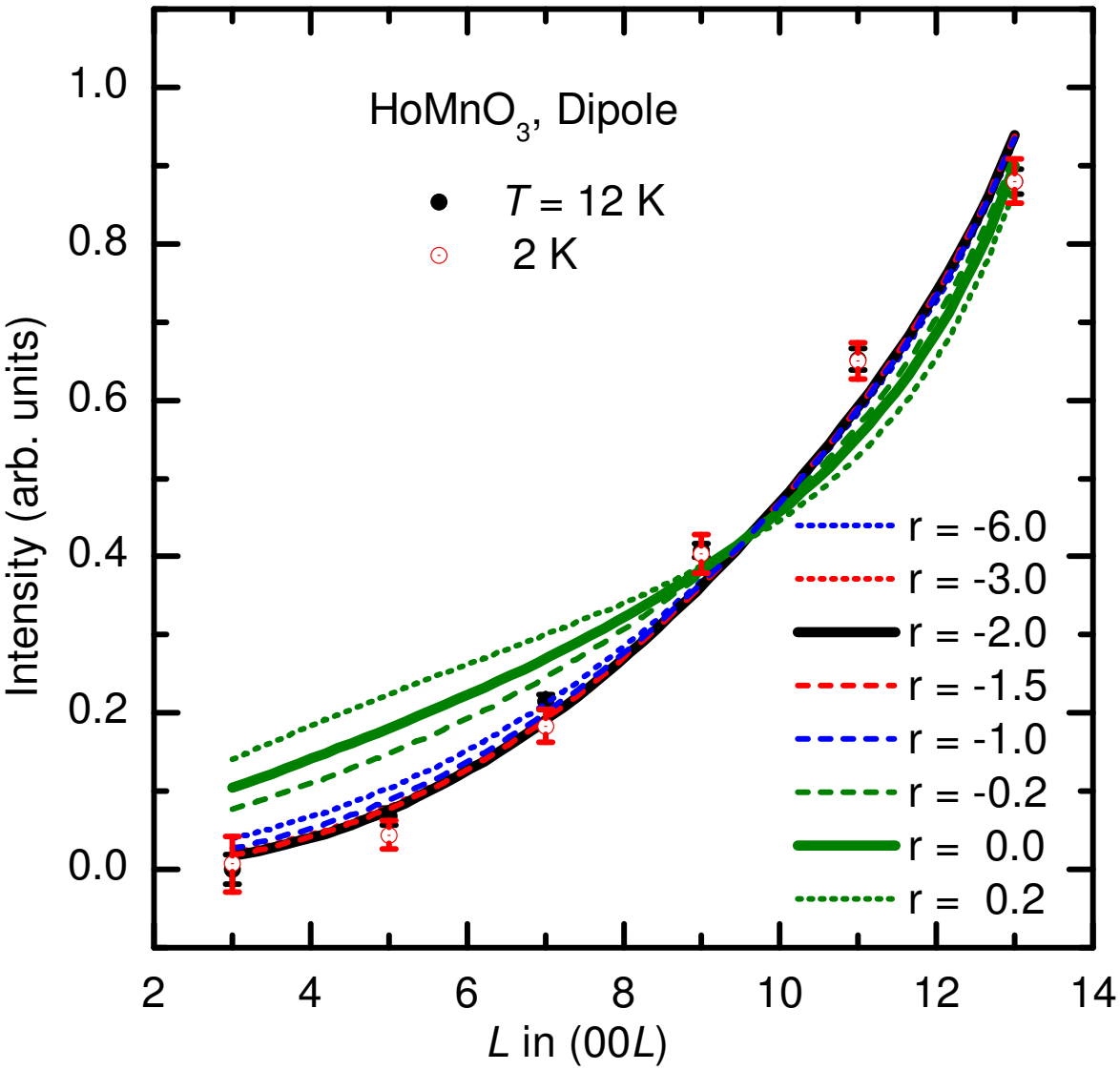

Figure 3.6 Observed intensity for the dipole resonance for $(0\,0\,l)$ reflections at 12 K and 2 K. The intensities at 2 K have been scaled by a factor of 1.1 to compare with the intensities at 12 K. Solid and dashed lines represent fits based on Eq. 3.4 with different r $(= \frac{\mu_{2a}}{\mu_{4b}})$ values assuming the magnetic representation Γ_3.

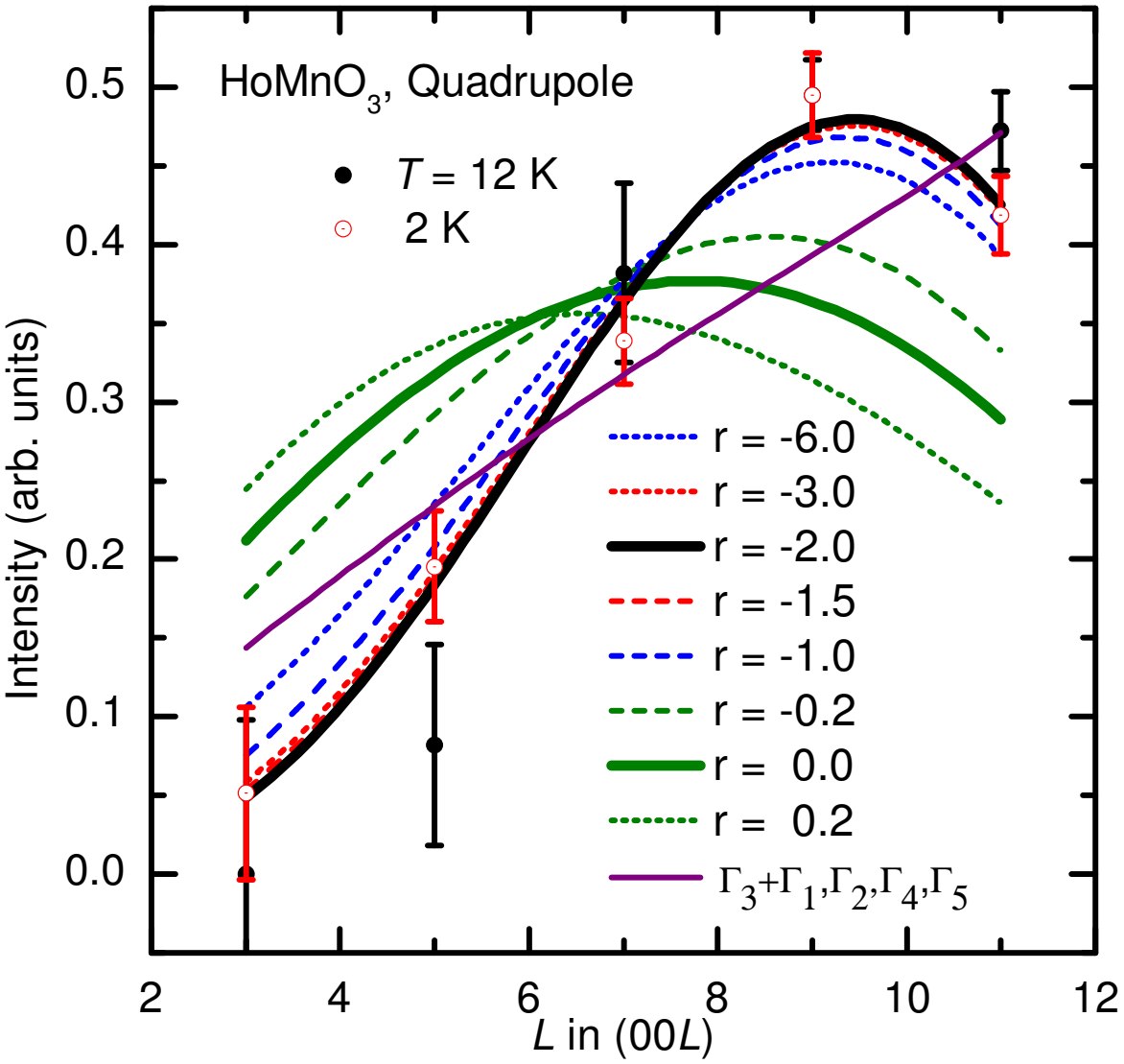

Figure 3.7 Observed intensity for quadrupole resonance for the (0 0 l) reflections at 12 K and 2 K. The intensities at 2 K have been scaled by a factor of 0.9 to compare with the intensities at 12 K. Solid and dashed lines represent fits based on Eq. 3.5 with different r ($= \frac{\mu_{2a}}{\mu_{4b}}$) values assuming the magnetic representation Γ_3. We also show the fitting results for the combination of magnetic representations as described in the text.

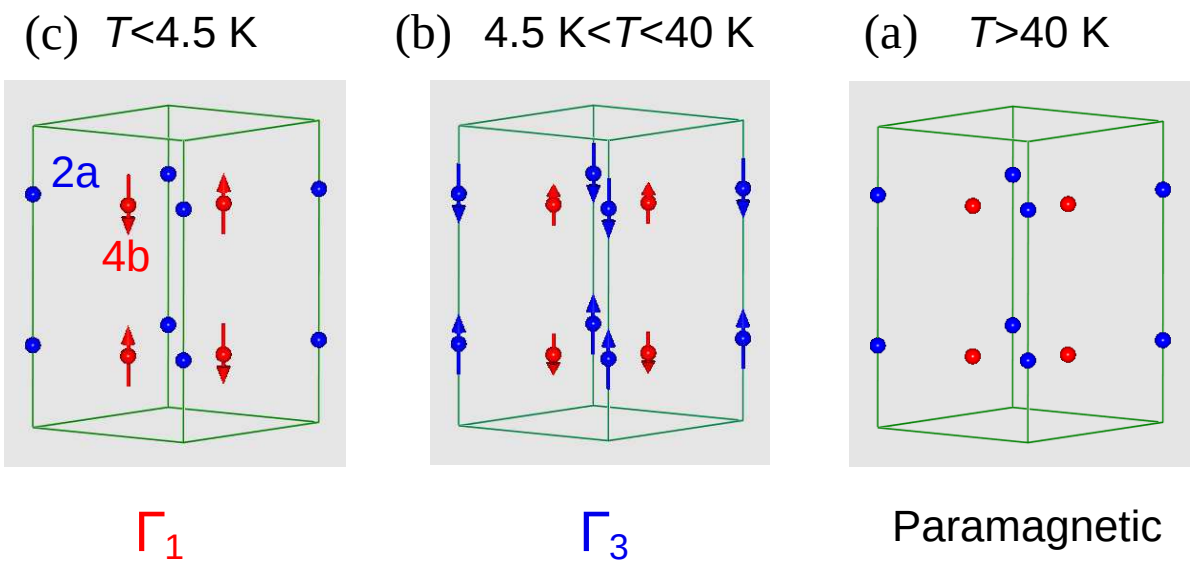

Figure 3.8 Magnetic structure of Ho^{3+} moments at different temperature range. (a) Above $T > 40$ K, the Ho^{3+} moments are in a paramagnetic state. (b) and (c) Magnetic structure of Ho^{3+} moments in the intermediate temperature phase (ITP) and in the low temperature phase (LTP), respectively.

The temperature dependence of Ho^{3+} moments in the ITP shown in Fig. 3.9 is unusual, but can be explained with reference to other systems such as Nd_2BaNiO_5 and Nd_2CuO_4, with ground state quasidoublet crystal field levels, split by an exchange field.[92, 93, 94] The non-Kramers Ho^{3+} ions in $HoMnO_3$ are at positions of trigonal symmetry which typically leads to singlets with very small zero-field splitting, forming a quasidoublet.[95, 96] Indeed, crystal field excitations in neutron scattering experiments below 40 K [49, 97] indicate a splitting of this quasidoublet which likely originates from the exchange interaction between Mn^{3+} and Ho^{3+}. Since the observed ordered magnetic moment of Mn^{3+} remains almost constant below 40 K [47], we can assume the crystal field splitting of the ground state, Δ_{eff}, is constant with temperature as well. If we assume an effective two level system with a splitting Δ_{eff}, we can write[92, 94]:

$$\mu(T) = \mu(0) \tanh \frac{\Delta_{\text{eff}}}{2kT} \tag{3.11}$$

where $\mu(T)$ and $\mu(0)$ are the magnetic moments at the temperature T and 0 K, respectively. The fitting of the temperature dependence of the magnetic moments shown in Fig. 3.9 yields $\Delta_{\text{eff}}^{(2a)} = (1.4 \pm 0.2)$ meV and $\Delta_{\text{eff}}^{(4b)} = (1.2 \pm 0.2)$ meV for the Ho $(2a)$ and $(4b)$ sites, respectively, consistent with the reported low-energy crystal electric field transition of 1.5 meV observed in inelastic neutron measurements.[49, 97] In the neutron scattering measurements, this excitation appears at temperatures below the reorientation of the Mn^{3+} moments and appearance of the ITP.[98] One possible origin of the exchange field from Mn^{3+}, and the consequent splitting of quasidoublet ground state by ~ 1.5 meV, is the anisotropic exchange interaction between Ho^{3+} and Mn^{3+}.[99] Since, no magnetic ordering of Ho^{3+} could be found above the ITP, we speculate that the exchange interaction becomes finite only below the reorientation of the Mn^{3+} moments with the change of magnetic symmetry of Mn^{3+} from Γ_4 to Γ_3.

The Magnetic structure of Ho^{3+} in the low temperature magnetic phase ($T \leq 4.5$ K)

We now turn to our investigation of the magnetic structure below 4.5 K (low temperature phase, LTP), which is considerably more complex. Similar to our approach for the intermediate temperature phase (ITP), we measured the off-specular reflections (2 0 9) and ($\overline{2}$ 0 9)

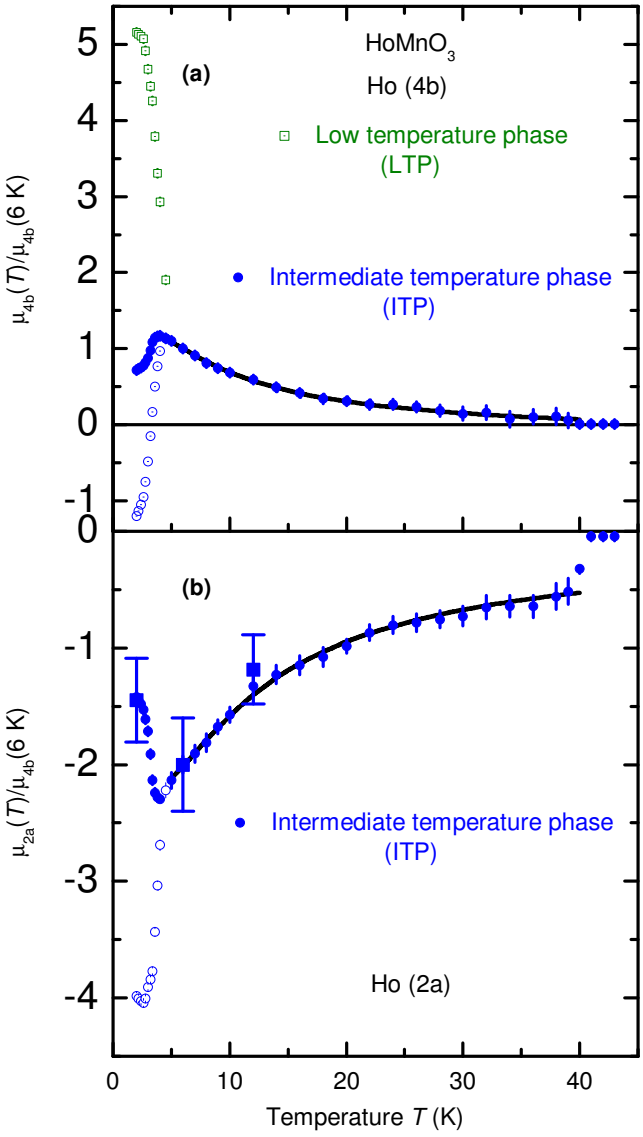

Figure 3.9 Temperature dependence of the magnetic moments derived from the quadrupole intensities of (0 0 9) and (1 0 9) reflections. Solid circles (blue) represent the moment size in the ITP according to representation Γ_3. The solid lines (black) in the ITP are fits using Eq. 3.11. (a) The open squares (olive) represent the Ho($4b$) moment in the LTP (Γ_1). Below 4.5 K the open circles (blue) in (a) and (b) represent the magnetic moment at the Ho($2a$) and (4b) sites if the low temperature phase would consist only of Γ_3 (same as ITP). The solid squares (blue) in (b) are the moment size according to angular dependent measurements at selected temperatures.

at 2 K to determine the moment direction. The calculated ratio $\frac{I(2\ 0\ 9)}{I(\overline{2}\ 0\ 9)} = 15.5$ and 0.4 for the moments along the **c** direction and in the **a-b** plane, respectively. The experimentally observed ratio is 22 ± 7. The relatively large error bar in the experimentally observed ratio is due to the much smaller integrated intensity of the ($\overline{2}$ 0 9) reflection compared to the (2 0 9) reflection. Therefore, the magnetic moments are, again, primarily aligned along the hexagonal **c** direction allowing only magnetic representations Γ_1 and Γ_3 (see Table 2.8) in the LTP. From Fig. 3.4 & 3.5, we notice that, below 4.5 K, the intensity of the (0 0 9) magnetic reflection rapidly decreases while the intensity of (1 0 9) increases strongly signalling a transition from Γ_3 to Γ_1. An interesting consequence of this transition is that Ho($2a$) site cannot order magnetically according to the representation Γ_1. The magnetic structure in this LTP is shown in Fig. 3.8(c). The finite intensity of the (0 0 9) reflection below 4.5 K is likely due to residual beam heating effects although we can not exclude a mixed Γ_3/Γ_1 phase, as discussed in detail below.

The magnetic representation Γ_3 can contributes to both (0 0 l) and (h 0 l) reflections whereas Γ_1 allows intensity only for the (h 0 l) reflections with l odd. Therefore, a non-zero intensity for (0 0 l) reflections with l odd implies that at least some portion of the sample remains in Γ_3. The angular dependent measurement on a series of (0 0 l) reflections at 2 K (see Fig. 3.6 & 3.7) yields the same moment ratio ($r \sim -2$) as that of ITP at 12 K. With the same moment ratio as that of ITP, the decreasing intensity of (0 0 9) and (0 0 5) reflections implies a decreasing 'ordered moment'[3] in Γ_3. However, if the magnetic phase consists only of Γ_3, we also expect a decrease in the intensity of the (1 0 9) and (1 0 7) reflections, similar to the (0 0 9) reflection below 4.5 K (see Eq. 2.34). Instead, we see a rapid increase of intensity. As we mentioned before, other than Γ_3, only Γ_1 can yield intensity at the (1 0 9) reflection. Therefore, the increase of intensity for the (1 0 9) and (1 0 7) reflections can only be explained by the co-existence of a new low temperature magnetic phase (LTP) in the magnetic representation Γ_1 with the remaining ITP in the magnetic representation Γ_3. Inspections of the low-temperature regions of Figs. 3.4(a) & 3.5(a) show that while the intensity of (0 0 9) reflection rapidly

[3]The term 'ordered moment' implies a product of volume fraction and the size of ordered magnetic moment for a particular representation.

decreases below 4.5 K, it does not disappear. This opens the possibility of a mixed phase with both Γ_3 and Γ_1 representations below 4.5 K. Phase co-existence between different magnetic phases has been observed in perovskite manganites, $R\mathrm{MnO_3}$[100] but only over a temperature range of ~ 1 K and was attributed to internal stress due to lattice mismatch between magnetic phases. A similar mechanism is possible for $\mathrm{HoMnO_3}$. However, measurements of the intensity of the (0 0 9) reflection in this low temperature region, while varying the incident beam attenuation, reveals the presence of residual beam heating effects, and it is likely that the saturation of the scattering signals and hence, the phase co-existence arises from this local beam heating effect.

Temperature dependence of the magnetic moment in the low temperature phase

The temperature dependence of magnetic moments at both Ho sites can also be derived from the (0 0 9) and (1 0 9) reflections, or from a single reflection, assuming one of the possible magnetic representations mentioned above. Through the temperature dependence of magnetic moments, we will justify that a phase transition from the Γ_3 to the Γ_1 magnetic representation is necessary to explain the temperature dependence of both (0 0 9) and (1 0 9) reflections as well as the angular dependent measurements.

For the time being we assume that, below 4.5 K, the magnetic representation remains Γ_3 for moments at both Ho sites. The normalized values of μ_{4b} and μ_{2a} can be obtained from the intensity of (0 0 9) and (1 0 9) reflections using the same procedure as for the ITP. The results are illustrated in Fig. 3.9 by the open circles (blue). However, the ratio r between the magnetic moments on both Ho sites would have to change dramatically from negative to positive values as indicated by a change of sign for the magnetic moment at the μ_{4b} site in Fig. 3.9(a). The change of sign of r corresponds to a change in the correlation between two sites in the **a-b** plane from antiferromagnetic to ferromagnetic. This is in contradiction to the value of $r \sim -2$ obtained from a series of (0 0 l) reflections. Figures 3.6 & 3.7 show the angular dependent measurements for both dipole and quadrupole resonances. It can be easily seen that the ratio of magnetic moments, $r = -2$ at 2 K, is the same as that found at 6 K and 12 K. Hence, the

presumption that the magnetic phase consists only of Γ_3 can not be correct.

In the following, we will analyze the data by assuming a phase co-existence between ITP with magnetic representation Γ_3 and a new LTP with magnetic representation Γ_1. Magnetic representation Γ_1 does not allow an ordered magnetic moment at the Ho($2a$) site (see Table 2.8). The temperature dependence of the magnetic moments in the Γ_3 magnetic representation below 4.5 K can be obtained from the temperature dependence of (0 0 9) reflection and, using the constant value of r, (see Eq. 3.10) it is shown by the solid circles (blue) in Fig. 3.9. The decreasing ordered moment merely reflects the decreasing intensity of the (0 0 9) reflection and is consistent with the result for the ordered moment determined from the series of (0 0 l) reflections as shown by the solid (blue) squares.

The open (olive) squares in Fig. 3.9(a) represent the calculated temperature dependence of the Ho($4b$) magnetic moments in the Γ_1 magnetic representation extracted from the intensity of (1 0 9) reflection after subtracting the contribution to this reflection from the moments ordered in the Γ_3 magnetic representation. The intensity of (1 0 9) reflection after subtraction is directly proportional to μ_{4b}^2 (see Eq. 2.32) for the Γ_1 magnetic representation and, thus, the temperature dependence of the magnetic moment can be obtained.

In summary, below 4.5 K the ordered magnetic moment in the ITP (magnetic representation Γ_3) decreases strongly with decreasing temperatures whereas the ordered moment at the Ho($4b$) site increases rapidly in the LTP (magnetic representation Γ_1).

3.1.5 Discussion

The different magnetic structures for Ho^{3+} moments, together with their characteristic temperatures, are summarized in Fig. 3.8. As we mentioned above, the Ho($4b$) moments are ordered according to Γ_1 in the LTP and the Ho($2a$) moments can not order according to the magnetic representation Γ_1 (see Table 2.8). An intriguing question is what happens to the Ho($2a$) moments? Are the Ho($2a$) moments (a) disordered due to frustration, for example,(b) suppressed due to the formation of a singlet ground state or (c) decoupled from the Ho($4b$) moments and order according to some different magnetic representation? We can exclude the

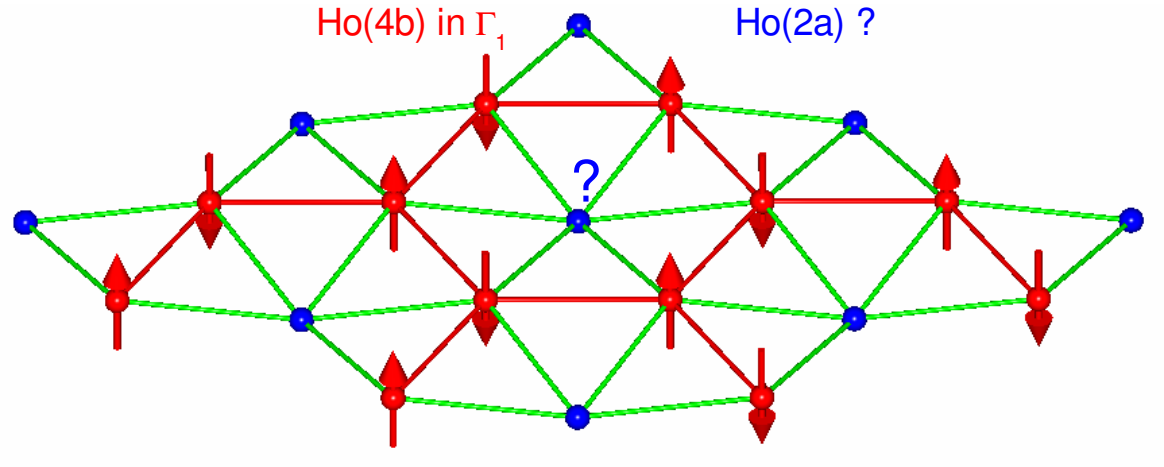

Figure 3.10 Arrangement of Ho^{3+} moments in the **a-b** plane for the low-temperature phase (LTP). The Ho($4b$) moments are ordered according to the magnetic representation Γ_1. Ho($2a$) moments are frustrated in this LTP assuming a finite size of magnetic moment. The green (Ho(2a)-Ho(4b)) and red (Ho(4b)-Ho(4b)) lines indicate two different bond lengths.

ordering of Ho($2a$) moments in the Γ_2, Γ_3, Γ_5 and Γ_6 magnetic representations for the following reasons. If the Ho($2a$) moments are ordered according to Γ_3 or Γ_6 magnetic representations, then the temperature dependence of the (0 0 9) and (1 0 9) reflections should be similar i.e. either both will increase or decrease, as can be easily seen from Eq.'s 2.50 and 2.51. On the other hand if the Ho($2a$) moments are ordered according to Γ_2 or Γ_5, then there should be a net ferromagnetic response along the hexagonal **c** direction or in the **a-b** plane (see Table 2.8) which has not been observed.[9, 44, 91] Similar to Γ_1, symmetry precludes magnetic order at the Ho($2a$) site according to Γ_4 (see Table 2.8). The remaining possibilities are: The Ho($2a$) moments order with another propagation vector or (a) remain disordered down to 2 K or (b) the moment size decreased to zero due to a singlet ground state. The first possibility can be safely excluded from the neutron powder diffraction measurements by Muñoz *et al.*[41], since only reflections corresponding to a magnetic unit cell which is the same as the chemical unit were observed. Therefore, the possibilities (a) and (b) are most likely. From the XRMS data,

separation between (a) and (b) is not possible. The decrease in entropy at 4.5 K, as concluded from the specific heat data in Fig. 3.2, points to a singlet ground state since a transition from a quasi-doublet ground state (as in the ITP) to a singlet ground state costs no entropy. On the other hand, disordered moments at the Ho(2a) site can not be completely excluded from the specific heat data since the increase of entropy due to disorder at the Ho(2a) site is overcompensated by the rapid increase of ordered moment at the Ho(4b) site (see Fig. 3.9) as well as 2:1 ratio of the Ho(4b) and Ho(2a) atoms in the unit cell, resulting in an overall decrease in entropy. Indeed, a degree of frustration at the positions of the Ho($2a$) moments is possible from Fig. 3.10 considering nearest neighbor interactions between the Ho($2a$) and Ho($4b$) moments. The Ho($2a$) moments are surrounded by an equal number of up and down Ho($4b$) moments and all the bond lengths (indicated by green lines) are the same. Therefore, the net interaction at the Ho($2a$) position vanishes and thereby, the possibility (b) remains open. Therefore, to separate between (a) and (b), further measurements such as inelastic neutron scattering searching for a singlet ground state as well as a detailed measurement of specific heat down to much lower temperature are necessary.

3.1.6 Conclusions

In conclusion, we have determined unequivocally the magnetic structure of Ho^{3+} in $HoMnO_3$ to be Γ_3 in the intermediate temperature magnetic phase ITP (between 40 K and 4.5 K). The magnetic Ho^{3+} moments are aligned along the **c** axis and, at 12 K, the ratio between the magnetic moments of the Ho($2a$) and Ho($4b$) Wyckoff site is ~ -2. The moments at the Ho($2a$) site are antiferromagnetically aligned to the moments at the Ho($4b$) site in the **a-b** plane. The moments at the both sites are antiferromagnetically correlated along the **c** direction. The determined magnetic structure in the ITP is consistent with the results of Lonkai *et al.*[9, 46, 47, 87] as well as Brown and Chatterji,[48] discussed in model 3 in the introduction. The temperature dependence of magnetic moments in the ITP can be explained by assuming low lying crystal field levels. We also conclude that there is a change of the magnetic structure of Ho^{3+} at 4.5 K. Below 4.5 K, the magnetic phase can be well described by the co-existence of

the ITP (Γ_3) with a decreasing 'ordered moment' and a new magnetic phase LTP with magnetic representation Γ_1 with a rapidly increasing Ho ($4b$) moment for decreasing temperatures. The phase co-existence most likely arises from the local beam heating effects. One consequence of this transition is that the Ho($2a$) moments can not order according to the representation Γ_1. Therefore, it is likely that either the Ho($2a$) moments are disordered down to the lowest achievable temperature of 2 K due to the frustration in the hexagonal lattice or the moments at the Ho(2a) site are suppressed due to the formation of a singlet ground state. The magnetic structure found in the LTP is consistent with Lonkai *et al.*[9, 46, 47, 87] but in contradiction with Brown and Chatterji.[48]

3.1.7 The Magnetic Order of Mn^{3+}

Introduction

The magnetic structures of Mn^{3+} moments in $HoMnO_3$ in the three different magnetic phases, the HTP (high temperature phase), ITP (intermediate temperature phase), and LTP (low temperature phase), have been studied by second harmonic generation as well as neutron diffraction experiments.[47, 48, 87] Specifically, Lonkai *et al.*[47] reported the magnetic representations Γ_4, Γ_3 and Γ_1 for the HTP, ITP and LTP, respectively. Despite careful study, however, there are still some unresolved issues regarding the magnetic structure of the Mn^{3+} moments. For example, in the ITP, the magnetic representation Γ_3 consists of two basis vectors $\vec{\psi_4}$ and $\vec{\psi_5}$ (see Table 3.1). According to representation theory, any linear combination of the basis vectors associated with an irreducible representation will have the symmetry of that irreducible representation. Therefore, in the case of Γ_3 representation, magnetic moment $\vec{\mu}$ should be properly described as:

$$\vec{\mu} = C_4\vec{\psi_4} + C_5\vec{\psi_5} \tag{3.12}$$

where C_4 and C_5 are two parameters. In neutron diffraction experiments, one has to properly refine these two parameters, to obtain the magnetic moment direction for the magnetic representation Γ_3. However, in the reports of Lonkai *et al.*[47] and Brown *et al.*[48] there is no

mention of the parameter C_5 associated with the component of magnetic moment along the **c** direction. For neutron scattering, detection of this **c** component is difficult due to the fact that Ho^{3+} moments also carries magnetic moment along the **c** direction and both **c** components will contribute to the same antiferromagnetic Bragg peaks. Nevertheless, the **c** component is important for our understanding of the magnetoelectric coupling in $HoMnO_3$ since it can directly couple to the **c** axis polarization.[50] Separation of the **c** component of Mn^{3+} moments from the **c** component of Ho^{3+} moments is possible in an XRMS experiment because of the elemental specificity of this technique. Further, the **c** component and planer components of the Mn^{3+} moments can be easily distinguished, as shown below, by a calculation of magnetic structure factor. For the Γ_3 representation, in the $\sigma \rightarrow \pi^{'}$ geometry, the structure factor for $(h\ 0\ l)$ reflections, with l = odd, for dipole resonant scattering can be written as:

$$F_m = [C\mu_c\{1 + 2\cos 2\pi hx\}\sin\theta + iD\mu_{ab}\sin 2\pi hx\cos\theta] \tag{3.13}$$

where C and D are two constants, and μ_c and μ_{ab} are the magnitudes of the magnetic moment along the **c** direction and in the **a-b** plane, respectively. From Eq. 3.13 we see that the reflections of the type $(h\ 0\ l)$ with $h \neq 0$ and l = odd will be sensitive to both **c** and in-plane (**a-b**) magnetic moment components, whereas $(0\ 0\ l)$ with l = odd will be sensitive only to the **c** component of the magnetic moment. Therefore, the existence of such a **c** component is accessible through an XRMS experiment.

The magnetic representation in the LTP is Γ_1 for both the magnetic sublattices, Ho^{3+} and Mn^{3+}. However, the phase transition from ITP to the LTP occurs in two steps since specific heat data show[90] a split transition with a temperature difference of $\Delta T = 0.4$ K at 4.5 K. It is not known at this point, which magnetic sublattice re-orders first and drives the phase transition for the other magnetic sublattice.

To resolve the above issues we performed an XRMS experiment at the Mn K-edge where the scattering process involves an intermediate state which arises from either dipole (E1) allowed ($1s$ – $4p$) or quadrupole (E2) allowed ($1p$ – $3d$) electronic excitations. In ordered materials then, XRMS is sensitive to the magnetization density through either the $3d$ electronic states

directly (E2) or indirectly through the spin polarization of the $4p$ states (E1).

Experimental Details

The experimental procedure is very similar to the resonant scattering experiment at the Ho L_{III} edge ($E = 8.071$ keV for Ho) except for the energy and the corresponding analyzer crystal. For the measurement at the Mn K absorption edge ($E = 6.553$ keV), a Cu (2 2 0) analyzer was used as a polarization and energy analyzer to suppress the charge as well as fluorescence background relative to the magnetic scattering signal.

Table 3.1 Basis vectors (BV) for the space group $P6_3cm$ with $\vec{k} = (0\ 0\ 0)$ for the Mn^{3+} moments at the Wyckoff position $6c$. The decomposition of the magnetic representation for the Mn $6c$ site is $\Gamma_{Mag} = 1\Gamma_1^1 + 2\Gamma_2^1 + 2\Gamma_3^1 + 1\Gamma_4^1 + 3\Gamma_5^2 + 3\Gamma_6^2$. Only the magnetic representation reported for the magnetic ordering of Mn^{3+} moments are listed in the table.[74] The directions of magnetic moments are denoted by [$\mathbf{e}_x$,$\mathbf{e}_y$,$\mathbf{e}_z$], where $\mathbf{e}_x$ and $\mathbf{e}_y$ are in the basal plane forming a 120 degree angle between them and the $\mathbf{e}_z$ vector is parallel to the 6-fold axis. The condition for a particular reflection is determined for the present experimental geometry and a dipole XRMS signal.

IR	BV	Atomic Positions						Magnetic Reflection	
		$(x,0,0)$	$(0,x,0)$	$(\bar{x},\bar{x},0)$	$(\bar{x},0,0.5)$	$(0,\bar{x},0.5)$	$(x,x,0.5)$	$(h\ 0\ l)$ l odd	$(0\ 0\ l)$ l odd
Γ_1	ψ_1	[1 2 0]	[$\bar{2}$ $\bar{1}$ 0]	[1 $\bar{1}$ 0]	[1 $\bar{2}$ 0]	[2 1 0]	[$\bar{1}$ 1 0]	Yes	Yes
Γ_2	ψ_2	[1 0 0]	[0 1 0]	[$\bar{1}$ $\bar{1}$ 0]	[$\bar{1}$ 0 0]	[0 $\bar{1}$ 0]	[1 1 0]	No	No
	ψ_3	[0 0 1]	[0 0 1]	[0 0 1]	[0 0 1]	[0 0 1]	[0 0 1]		
Γ_3	ψ_4	[1 0 0]	[0 1 0]	[$\bar{1}$ $\bar{1}$ 0]	[1 0 0]	[0 1 0]	[$\bar{1}$ $\bar{1}$ 0]	Yes	Yes
	ψ_5	[0 0 1]	[0 0 1]	[0 0 1]	[0 0 $\bar{1}$]	[0 0 $\bar{1}$]	[0 0 $\bar{1}$]		
Γ_4	ψ_6	[1 2 0]	[$\bar{2}$ $\bar{1}$ 0]	[1 $\bar{1}$ 0]	[1 2 0]	[$\bar{2}$ $\bar{1}$ 0]	[1 $\bar{1}$ 0]	No	No

Results and Discussions

As we mentioned above, $(h\ 0\ l)$ reflections with $h \neq 0$ and $l =$ odd will be sensitive to both **c** and **a-b** components. Since the magnetic moment in the **a-b** plane is the dominant component, we first measured $(h\ 0\ l)$ reflections with $l =$ odd. We observed two predominant resonance features above the Mn K-edge shown in Fig. 3.11(b). However, the observed resonance enhance-

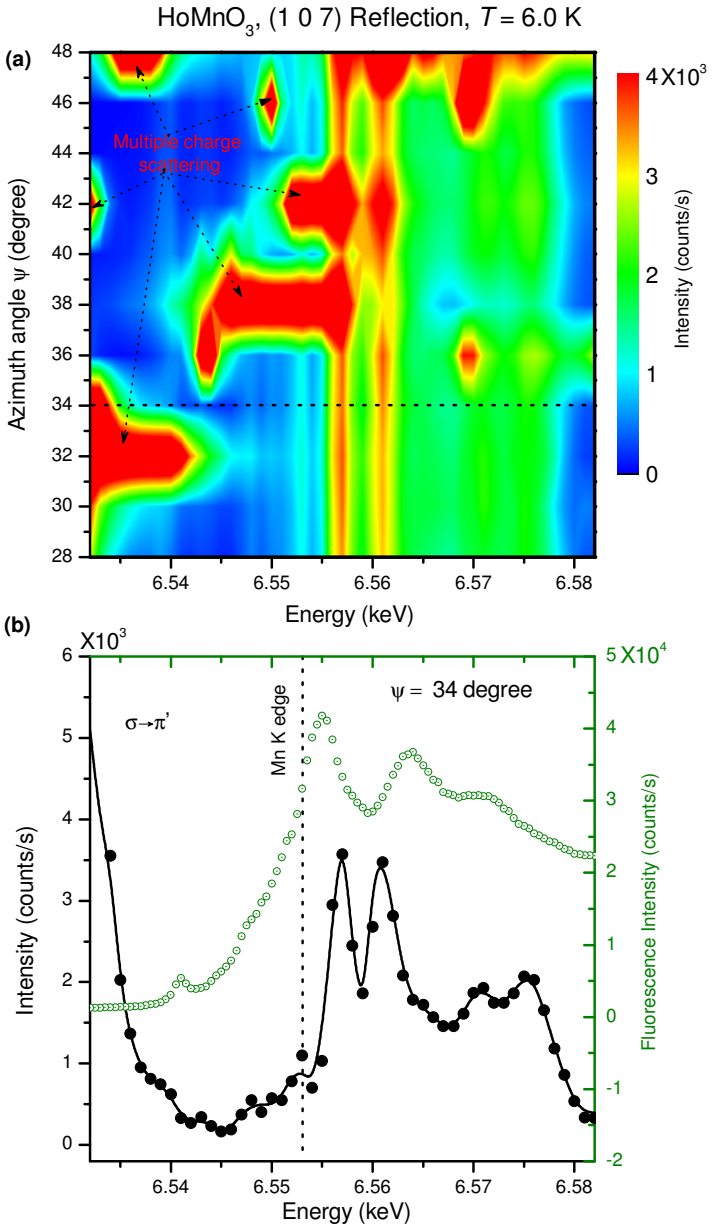

Figure 3.11 (a) Contour map of the intensity as a function of energy and azimuth angle ψ at the (1 0 9) position and $T = 6$ K. Arrows indicate a few of the multiple charge scattering positions. (b) Single energy scan at the azimuth angle $\psi = 34$ degree, which is depicted as a horizontal dashed line in (a). The vertical dashed line in (b) represents the position of the Mn K-edge as determined from the inflection point of the observed fluorescence signal in (b).

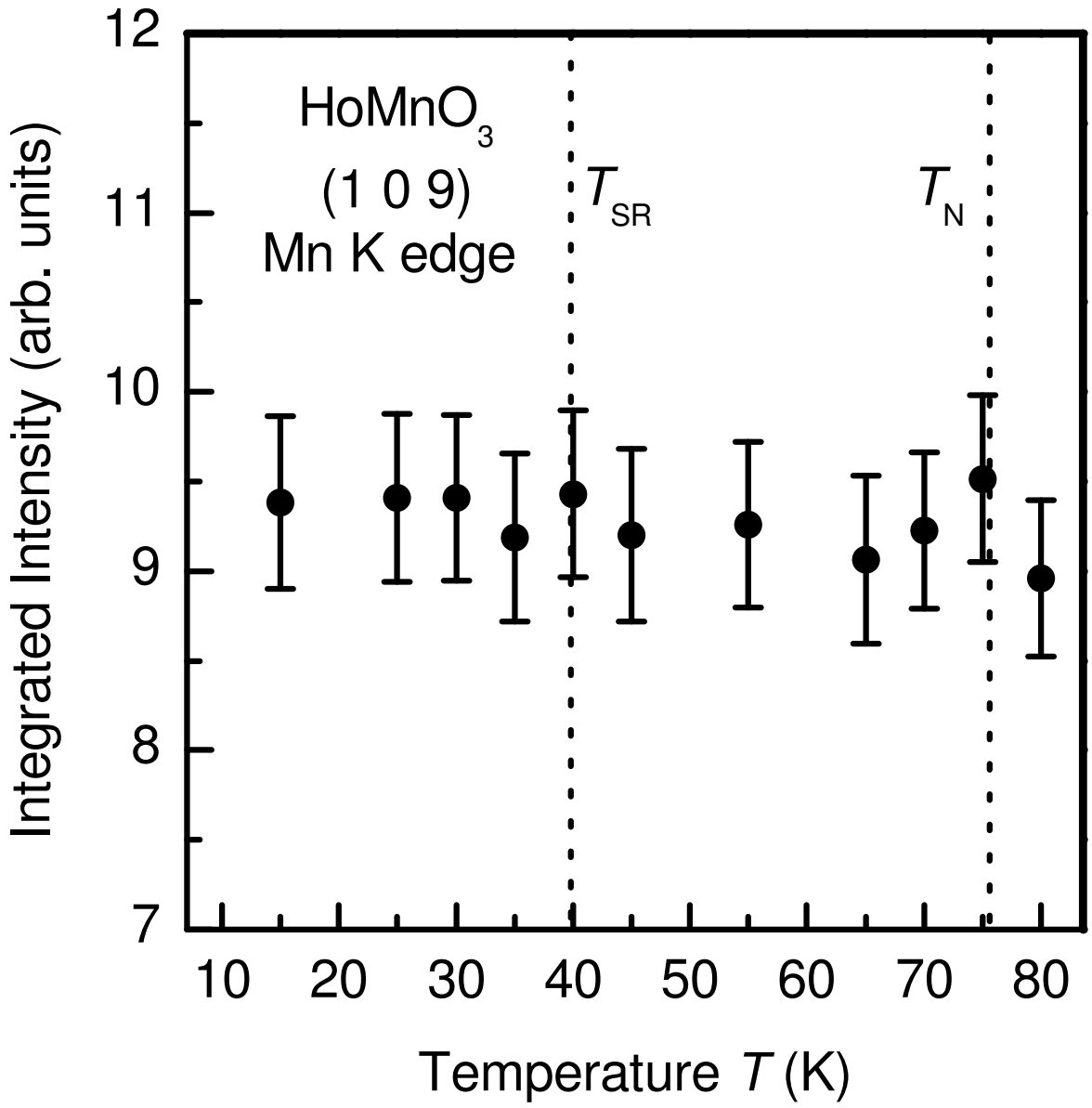

Figure 3.12 Temperature dependence of the integrated intensity of the (1 0 9) reflection measured at $E = 6.557$ keV. The vertical dashed lines mark the transition temperatures for the magnetic ordering of Mn^{3+} (T_N) and Ho^{3+} (T_{SR})

ments were too large to be magnetic since Mn K-edge magnetic resonance is known to be weak compared to the rare-earth L edges because of the absence of spin orbit splitting in the ground state as well as small overlap between 4p and 1s states.[4] We first verified that the resonance features are not contaminated by the multiple charge scattering by varying the azimuth angle (rotation of the sample around the scattering vector). We observed that the resonance features at E= 6.557 and 6.561 keV are almost independent of azimuth angle while multiple charge scattering depends sensitively on the azimuth angle, as expected.[102, 103] Therefore, from the contour plot, we conclude that the sharp features above the Mn K-edge arise from some sort of resonance enhancement. Nevertheless, the resonance enhancement is non-magnetic since the intensity of these features are temperature independent, in the temperature range of magnetic ordering, shown in Fig. 3.12. Furthermore, the temperature dependence of the integrated intensity shows no correlations with the magnetic transition temperatures at T = 40 K and 76 K. The temperature and energy dependence of other reflections such as (1 0 7), (-1 0 9), (2 0 9), (-2 0 9) and (0 0 5) were also measured. However, only temperature independent contributions were found. Therefore, we conclude that the magnetic resonance, if present, at the Mn K-edge is too weak to observe experimentally due to the presence of this dominant non-magnetic resonant signal.

The non-magnetic signal may be best described in terms of anisotropic tensor scattering which has been observed at the charge forbidden Bragg positions. For example, resonant scattering at the Fe K-edge of antiferromagnetic hematite, Fe_2O_3 has been studied and described by the anomalous tensor scattering (ATS).[104, 105] The basic formalism for the resonant magnetic scattering (XRMS) cross-section, presented in Chapter 2 and anisotropic tensor scattering are quite similar. In deducing the cross-section for XRMS, we have assumed that the symmetry is broken by a magnetic atom in an isotropic chemical environment. However, if the chemical environment itself is not isotropic, for example, an atom in an uniaxial environment, terms other than the resonant magnetic scattering become important at the absorption edges of the

[4] In the Ho L_{III} edge we have observed maximum of 800 counts/s for the (1 0 9) reflection at 2 K. Here, the intensity at the (1 0 9) peak at the Mn K-edge is $\sim$ 4000 counts/s. In the orthorhombic multiferroic compound, $TbMbO_3$, Mn K edge resonance has been observed[101] and the resonance enhancement is one order of magnitude less than the Tb L_{II} edge.

element of interest. If the atom carries a magnetic moment as well, both terms contribute to the resonant scattering amplitude. For the simplest case of an atom without a magnetic moment in an uniaxial environment, with $\hat{z}_s$ as an unit vector along that axis for the s^{th} atom in the unit cell, anomalous tensor scattering amplitude can be written as:[106]

$$f_{dipole}^{ATS} = [C_{0s}(\hat{\epsilon}^{'} \cdot \hat{\epsilon}) + C_{2s}\{(\hat{\epsilon}^{'} \cdot \hat{z}_s)(\hat{\epsilon} \cdot \hat{z}_s) - \frac{1}{3}\hat{\epsilon}^{'} \cdot \hat{\epsilon}\}] \tag{3.14}$$

where C_{0s} and C_{2s} are constants containing resonant denominator of the form $(E_n - E_a - \hbar\omega - i\Gamma/2)$. E_n and E_a are the energies corresponding to the excited state $|n\rangle$ and initial state $|a\rangle$, respectively. $\hat{\epsilon}$ and $\hat{\epsilon}^{'}$ are the polarization vectors for the incident and scattered x-rays, respectively.

From the above equation, we note the following important features of the ATS scattering:

1. The first and third term containing $\hat{\epsilon}^{'} \cdot \hat{\epsilon}$ contribute to the resonance enhancement of normal charge scattering, appears at the allowed Bragg position and can be used for contrast variation to enhance the scattering contrast between neighboring elements. This type of resonance enhancement is commonly known as *anomalous charge scattering*, mentioned briefly in Chapter 1. These terms do not change the polarization of incident x-rays and also do not depend on anisotropic environment of the resonant ion.

2. The term, $(\hat{\epsilon}^{'} \cdot \hat{z}_s)(\hat{\epsilon} \cdot \hat{z}_s)$, is responsible for observing ATS scattering as well as polarization properties of the scattered x-rays. A similar term, $(\hat{\epsilon}^{'} \cdot \hat{z}_n)(\hat{\epsilon} \cdot \hat{z}_n)$, where $\hat{z}_n$ is the unit vector in the direction of magnetic moment, was also present in the XRMS amplitude for the dipole scattering. Due to this close similarity, resonant magnetic scattering and ATS scattering appear in the same polarization channel.

3. ATS scattering appears at forbidden reflections, due to the fact that f_{dipole}^{ATS} depends on the direction of the scattering vector as well as on the orientation of the dyadic $\hat{z}_s^{\alpha}\hat{z}_s^{\beta}$. These two together will not necessarily have the full symmetry of the space group and, therefore, can excite forbidden reflections.

Though, in the above example, polarization properties as well as appearance of the ATS scattering in forbidden positions can be understood, for the case of Mn^{3+} ions in $HoMnO_3$,

the form of f_{dipole}^{ATS} depends on the local symmetry of the Mn^{3+} ions and can be evaluated following the procedure mentioned in Refs. [107, 108, 109, 110]. However, the observation of multiple resonance features in Fig. 3.11 indicate the presence of higher order terms beside the dipole and possible interference between them. Calculation of these higher order terms in ATS scattering as well as verification by experiment (measuring intensity for a number of reciprocal lattice points as well recording intensity as a function of azimuth angle) require a heroic effort due the presence of multiple charge scattering and therefore, we have not pursued this line of experiments further.

Summarizing, the XRMS experiment at the Mn K edge, no magnetic signal could be detected possibly due the presence of nonmagnetic ATS scattering. Therefore, we could not address the importance of the **c** component of Mn^{3+} in the magnetoelectric coupling.

3.2 Magnetic Ordering in $DyMnO_3$ and $ErMnO_3$ in Zero Field

3.2.1 Introduction

Among all the hexagonal $R\mathrm{MnO_3}$ compounds studied so far (rare earths Ho to Lu), only for $HoMnO_3$ was a spin reorientation of Mn^{3+} moments around 40 K reported. In the previous section, we have shown that this spin-reorientation transition is associated with the magnetic ordering of Ho^{3+} moments induced by the Mn^{3+} moments. The question naturally arises is what is so unique about the rare-earth element Ho in the rare-earth series? Is there any other hexagonal $R\mathrm{MnO_3}$, where a spin reorientation of the Mn^{3+} moments and associated induced order of rare-earth moments can be found? Or, are conventional techniques blind to the induced component of magnetic moment at the rare-earth site, for example, for the magnetic order of Er^{3+} moments in $ErMnO_3$? This motivated us to study systematics of $R\mathrm{MnO_3}$ compounds with rare-earth elements Dy and Er. One obvious difference between Ho^{3+} with Er^{3+} and Dy^{3+} is that while Ho^{3+} is a non-Kramer's ion, the later two are Kramer's ions. Fortunately, under special conditions the hexagonal phase of $DyMnO_3$ can be stabilized[39, 111] (generally found in orthorhombic form) and makes this systematic study possible.

Both hexagonal $DyMnO_3$ and $ErMnO_3$ exhibit ferroelectricity at room temperature.[31,

111] It was concluded from magnetization measurements that the Dy^{3+} moments order ferrimagnetically below 7 K. Nevertheless, the magnetic structure and the corresponding magnetic symmetry remained unknown.[39] Similar to the situation described for $HoMnO_3$, previous studies of $ErMnO_3$ have presented inconsistent pictures of the magnetic ordering of Er^{3+}. For example, employing magnetoelectric measurements, Sugie *et al.*[44] proposed that Er^{3+} moments order non-collinearly in the hexagonal **a-b** plane according to the magnetic representation Γ_6 below 6 K. Fiebig *et al.*[99], however, using optical second harmonic generation and Faraday rotation experiments, proposed that the Mn^{3+} moments order according to the magnetic representation Γ_4 below 78 K and transform to another magnetic structure with magnetic representation Γ_2 at around 6 K. According to Fiebig *et al.*[99] Er^{3+} remains paramagnetic in the temperature range 78 K down to 6 K and becomes ferrimagnetic below 6 K. Yen *et el.*[112] have also observed a steep increase in magnetization at low fields but without the hysteresis observed by Fiebig *et al.*[99] and Sugie *et al.*[44]

Since the naturally occurring isotope of Dy is neutron absorbing, the magnetic structure determination by neutron diffraction is challenging but possible, and has not, to date, been done. In addition, discriminating between the two magnetic sublattices, R^{3+} and Mn^{3+}, as discussed above for $HoMnO_3$, is very difficult. An x-ray resonant magnetic scattering (XRMS) study of $DyMnO_3$ and $ErMnO_3$ is complementary to neutron measurements, but more direct in determining the magnetic structure associated with, and the order parameter of, the R^{3+} moments.

3.2.2 Experimental Details

Single crystals of $DyMnO_3$ and $ErMnO_3$ were grown using a floating zone method described previously.[39] For the XRMS measurements, single crystals of approximate dimensions $4 \times 3 \times 1$ mm^3 and $3{\times}2{\times}2$ mm^3 were selected with a surface perpendicular to the **c** axis for $DyMnO_3$, and $ErMnO_3$, respectively. The experimental details for the XRMS experiments are very similar to that described for $HoMnO_3$. The XRMS experiment was performed on the 6ID-B beamline at the Advanced Photon Source at the Dy and Er L_{III} absorption edges ($E = 7.790$ keV

and 8.355 keV, respectively). The incident radiation was linearly polarized perpendicular to the vertical scattering plane (σ-polarized) with a spatial cross-section of 0.6 mm (horizontal) $\times$ 0.2 mm (vertical). In this configuration, resonant magnetic scattering rotates the plane of linear polarization into the scattering plane (π-polarization). In contrast, charge scattering does not change the polarization of the scattered photons (σ-$\sigma^{'}$ scattering). In addition to the σ-$\pi^{'}$ scattering geometry we have also used π-$\pi^{'}$ and π-$\sigma^{'}$ scattering geometries. In both geometries, a Pyrolytic graphite PG (0 0 6) analyzer was used as a polarization analyzer to suppress the charge and fluorescence background relative to the magnetic scattering signal. For the $P6_3cm$ crystallographic space group, (h 0 l) with l = odd are the allowed charge reflections. Therefore, for measurements of the antiferromagnetic (0 0 l) and (h 0 l) reflections, with l odd, the sample was mounted at the end of the cold-finger of a displex cryogenic refrigerator with the reciprocal $\mathbf{b}^{\star}$ - $\mathbf{c}^{\star}$ plane coincident with the scattering plane. Though these reflections are forbidden for charge reflections they can be strongly contaminated by multiple charge scattering. However, we were able to minimize multiple scattering contribution at the resonant energy through a judicious choice of the azimuth angle.

3.2.3 Magnetic Structure of Dy^{3+} in $DyMnO_3$

Observation of magnetic resonant scattering and characterization of the transition temperatures

Fig. 3.13 shows the magnetization curves and magnetic susceptibility of a $DyMnO_3$ single crystal, measured using a Quantum Design SQUID magnetometer. In the inset to Fig. 3.13(c), we see a kink in magnetic susceptibility at 68 K, suggesting the possibility of a magnetic order. At approximately 8 K, there is a dramatic change of the magnetic susceptibility, indicating a phase transition from the intermediate temperature phase, ITP (68$-$8 K) to the low temperature phase, LTP (below 8 K).

In the ITP, magnetic intensity was found at the (0 0 9) reciprocal lattice point which is nominally forbidden for charge scattering. To confirm the resonant behavior of this feature, we performed energy scans (as shown in Fig. 3.14) through the Dy L_{III} absorption from 3 K to

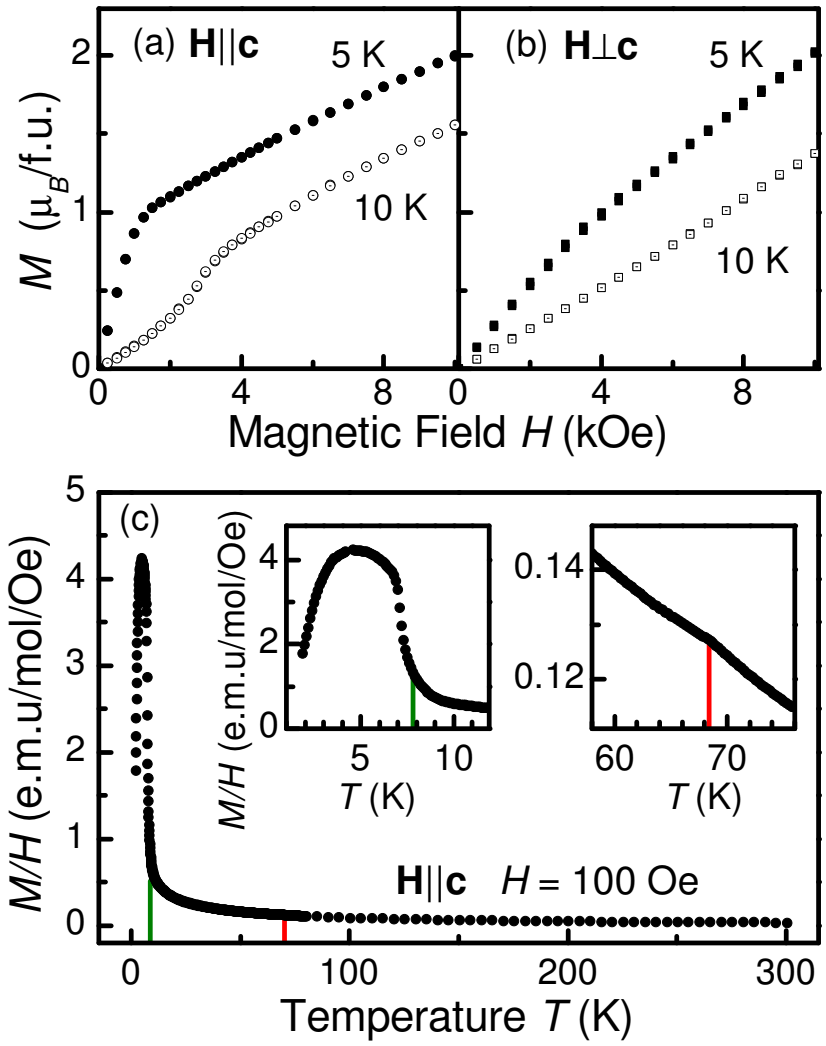

Figure 3.13 (a-b) Magnetization curves of the $DyMnO_3$ single crystal measured along and perpendicular to the **c** direction at 5 and 10 K. (c) Temperature dependence of magnetic susceptibility was measured on heating the zero-field cooled sample in a field of 100 Oe applied parallel to the **c** axes. The insets show details of the magnetic susceptibility near the transition temperatures of the order of Dy^{3+} moments. Marked vertical lines are the transition temperatures determined from the XRMS measurements.

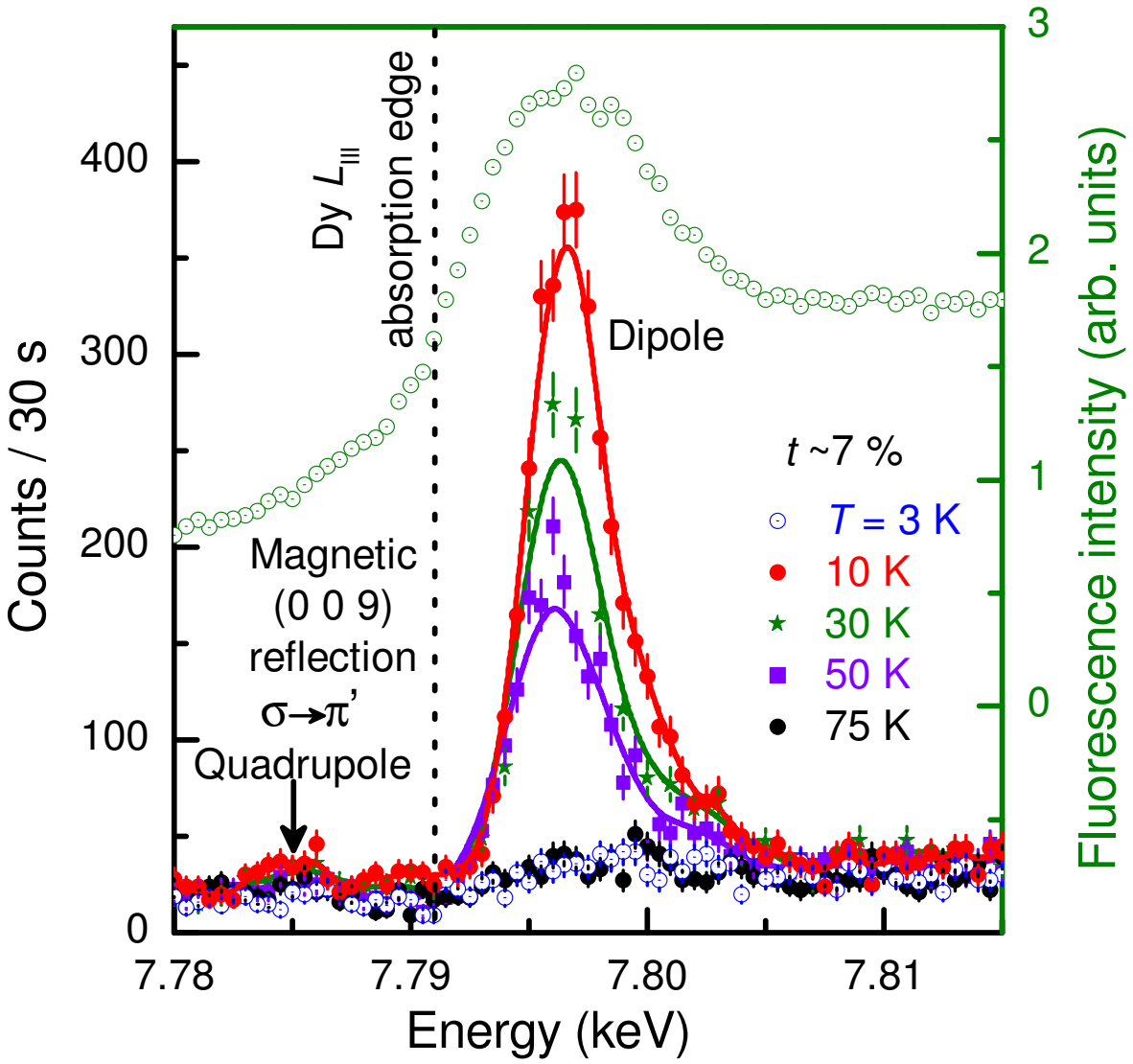

Figure 3.14 Energy scans of the (0 0 9) reflection and of the fluorescence signal. The small peak marked by the vertical arrow indicates weak quadrupole resonance. The dashed line depicts the Dy L_{III} absorption edge as determined from the inflection point of the fluorescence signal. The solid lines are guide to the eye.

75 K, and observed one predominant resonance peak approximately 6 eV above the absorption edge. This peak arises from dipole resonant scattering involving an intermediate state transition between the core $2p$ and the empty $5d$ states.[60] We also note the presence of a weak quadrupole resonance ($2p$-to-$4f$ states) at approximately 5 eV below the absorption edge. In the energy scans, no resonance intensity was observed above the ITP. Further, from Fig. 3.14, we see that the dipole resonance intensity increases with decreasing temperatures in the ITP. However, this signal disappears abruptly below 8 K.

Generally, local sample heating by the intense incident undulator beam is very strong for insulating materials like $DyMnO_3$, particularly at low temperatures. Therefore, to characterize the beam heating effect and to determine the transition temperature for magnetic ordering of Dy^{3+}, we measured the dipole resonance intensity of the (0 0 9) reflection with different attenuators as shown in the inset to Fig. 3.15. Since the normalized peak intensity and transition temperature remained nearly the same using attenuators with transmissions of $t{\sim}7\%$ and $t{\sim}1\%$, temperature dependent measurements were performed with the former. It should be noted that measurements at the Dy L_{III} edge was performed with slightly less attenuatation ($t{\sim}7\%$) compared to the Ho L_{III} ($t{\sim}1.8\%$) and this difference could be due to the differences in the surface conditions. For $HoMnO_3$ the surface was polished whereas for $DyMnO_3$ an as-grown sample surface was used. Fig. 3.15 shows the temperature dependence of the integrated intensity for the (0 0 9) reflection, determined by fitting θ-scans (rocking curves) with a Lorentzian function. Below 68 K, the dipole intensity increases gradually with decreasing temperature. The temperature of the onset of the magnetic order of Dy^{3+} agrees well with the kink in magnetization data from the same sample as shown in Fig. 3.13. Again from Fig. 3.15, we see that the magnetic intensity of the (0 0 9) reflection decreases rapidly and goes to zero below 8 K, signifying the phase transition to the LTP.

Magnetic structure in the intermediate temperature phase

We now turn to the analysis of the magnetic structure in the ITP. In order to determine the magnetic representation we must look into the details of six magnetic representations that are possible for the crystallographic space group $P6_3cm$, and are listed in the Table 2.8.

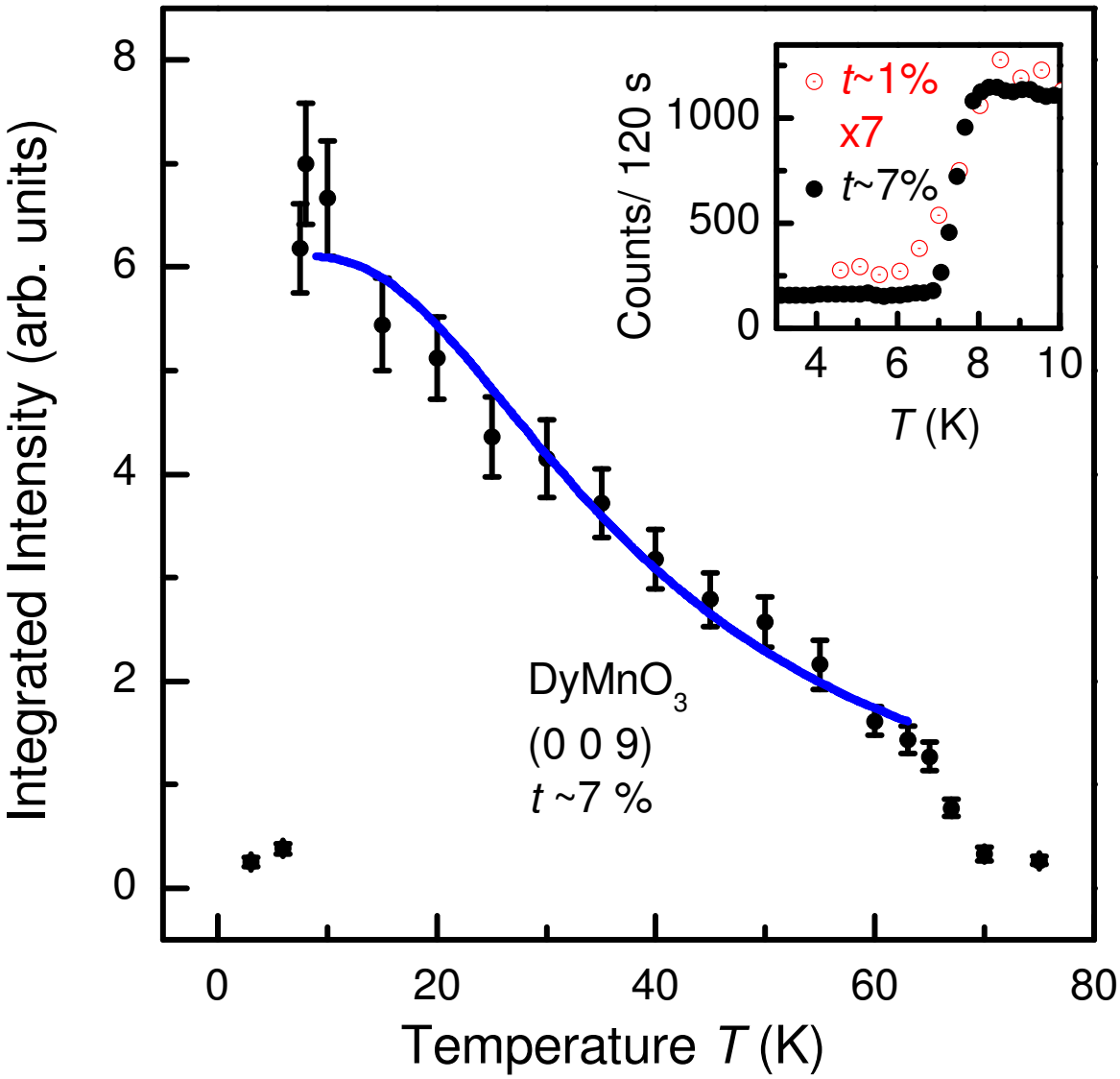

Figure 3.15 Temperature dependence of the integrated intensity of the dipole resonance for the (0 0 9) reflection. The inset shows details of the low temperature phase transition. The solid blue line is a fit to the data in the intermediate magnetic phase by a model as described in the text.

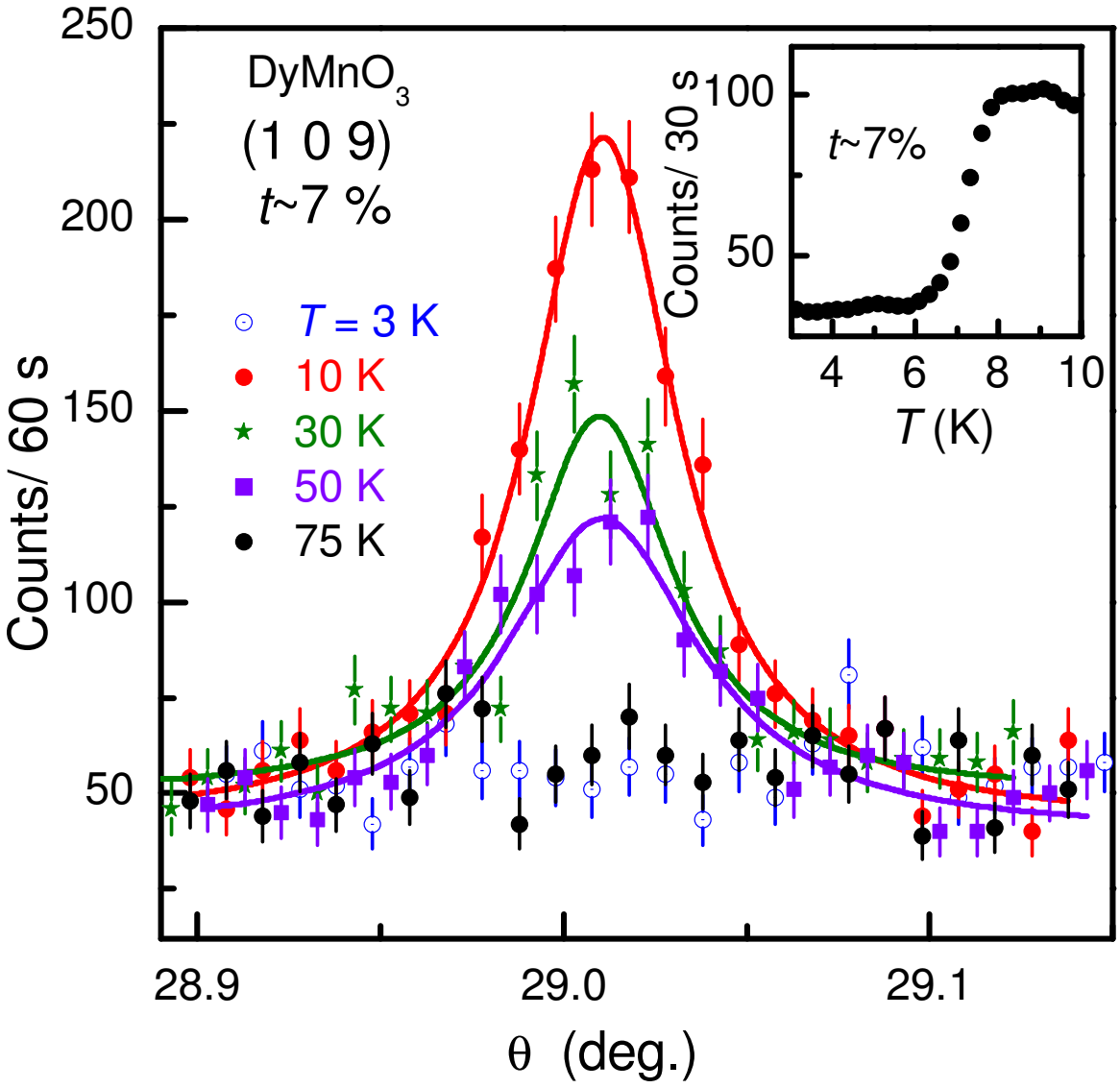

Figure 3.16 Representative rocking scans for an off-specular reflection (1 0 9). The inset shows the details of the low temperature phase transition. The peak intensity was measured to characterize the transition temperature. Lines are guide to the eye.

The observation of nonzero intensity for the (0 0 9) reflection clearly excludes the magnetic representations Γ_1, Γ_2, Γ_4 and Γ_5 for the magnetic order of Dy^{3+} (see Table 2.8) because only the representations Γ_3 and Γ_6 yield nonzero intensity for (0 0 l) reflections with l odd. The Dy^{3+} moments are aligned in the hexagonal **c** direction according to representation Γ_3 whereas they are aligned in the **a-b** plane in representation Γ_6.

We measured the off-specular reflections (3 0 9) and ($\overline{3}$ 0 9) to determine the moment direction. As discussed before for $HoMnO_3$, the structure factor is the same for both reflections, but the dipole scattering cross-section is different providing strong sensitivity to the moment direction. For our scattering geometry, the dipole scattering amplitude $f \propto \vec{k}' \cdot \vec{\mu}$,[64] where $\vec{k}'$ and $\vec{\mu}$ are the wave vector of the scattered photons and the magnetic moment, respectively. For moments aligned along the **c** direction (Γ_3), the magnetic intensity $I \propto \sin^2(\theta \pm \alpha)$; for moments in the **a-b** plane (Γ_6) $I \propto \cos^2(\theta \pm \alpha)$, where θ is the Bragg angle and α is the angle that the scattering vector **Q** makes with the crystallographic **c** direction perpendicular to the surface of the sample. The '+'/'−' signs are for larger/smaller angles of the outgoing beam with respect to the sample surface. The calculated ratio I(3 0 9) / I($\overline{3}$ 0 9) = 65 and 0.02 are for moments along the **c** direction and in the **a-b** plane, respectively. Since the absorption is different for these two off-specular reflections, proper normalization using the closest charge reflections was performed to determine the experimental ratio of 80 ± 20. Thus, within experimental error, the magnetic moments are primarily aligned in the hexagonal **c** direction. We can confirm that the magnetic moments are aligned only along the **c** direction by measuring (0 0 7) reflection in both polarization geometries, π-π' and π-σ', as shown in Fig. 3.17. As discussed in Chapter 2, for the π-σ' scattering geometry, the intensity for the antiferromagnetic Bragg peak for E1 resonant scattering is sensitive to the components of magnetic moment within the scattering plane (z_1 and z_3) whereas for π-π' scattering it is sensitive only to the component of magnetic moment perpendicular to the scattering plane (z_2). Therefore, the observation of non-zero intensity in the π-σ' geometry and zero intensity in π-π' geometry is only possible if the magnetic moments lie along the **c** direction.[5] We

[5]For quadrupole scattering, the scattering amplitude is complex, and the above observation is only possible if and only if the in-plane component of magnetic moment is zero.

conclude that the Dy^{3+} moments order according to the magnetic representation Γ_3 in the ITP.

Temperature dependence magnetic intensity in the intermediate temperature phase

Fig. 3.15 shows a gradual increase of the observed intensity as the temperature is decreased in the ITP. With reference to other systems, such as Nd_2BaNiO_5 and Nd_2CuO_4, the temperature dependence of the integrated intensity in the ITP can be explained with a ground state doublet crystal field level, split by an exchange field.[92, 93, 94] The Kramer's Dy^{3+} ions in $DyMnO_3$ are at positions of trigonal symmetry and, therefore, must have a doublet ground state.[113, 114] We recall that in the case of $HoMnO_3$, Ho^{3+} being a non-Kramer's ion, the ground state is different and is a quasi-doublet. At low temperatures only the ground state doublet is appreciably populated because the energy difference between the ground state and the next crystal electric field levels, in general, is large.[114] As we did for $HoMnO_3$, taking into account only the ground state doublet and a splitting, $\Delta(T)$, we can write [92, 94]

$$I(T) = I(0)[\tanh \frac{\Delta(T)}{2kT}]^2 \tag{3.15}$$

where $I(\mathrm{T})$ and $I(0)$ are the intensities at the temperature T and 0 K, respectively. For an exchange field produced by the ordering of the Mn^{3+} sublattice, the doublet splitting, $\Delta(T)$, is proportional to the ordered magnetic moment of Mn^{3+}.[92] In the case of $DyMnO_3$, however, the ordering temperature and the temperature dependence of Mn^{3+} moments have not been determined. For the nearest hexagonal compound, $HoMnO_3$, the Mn^{3+} moments order below 76 K and saturate within a few Kelvin.[47] Anticipating similar behavior for the Mn^{3+} moments in $DyMnO_3$, we assumed $\Delta(T)$ to be constant in the temperature range of fitting, 10−62 K. The fitting yields $\Delta = (5.8 \pm 0.8)\ meV$. Thus, the temperature dependence of integrated intensity in the ITP can be modeled using a simplified picture of the crystal field splitting and suggests an induced magnetic order of Dy^{3+} in this ITP. From the close similarity between the induced order of rare-earth moments in $HoMnO_3$ and $DyMnO_3$ by the Mn^{3+}, we predict that the Mn^{3+} moments in $DyMnO_3$ also order according to Γ_3 representation (same as that

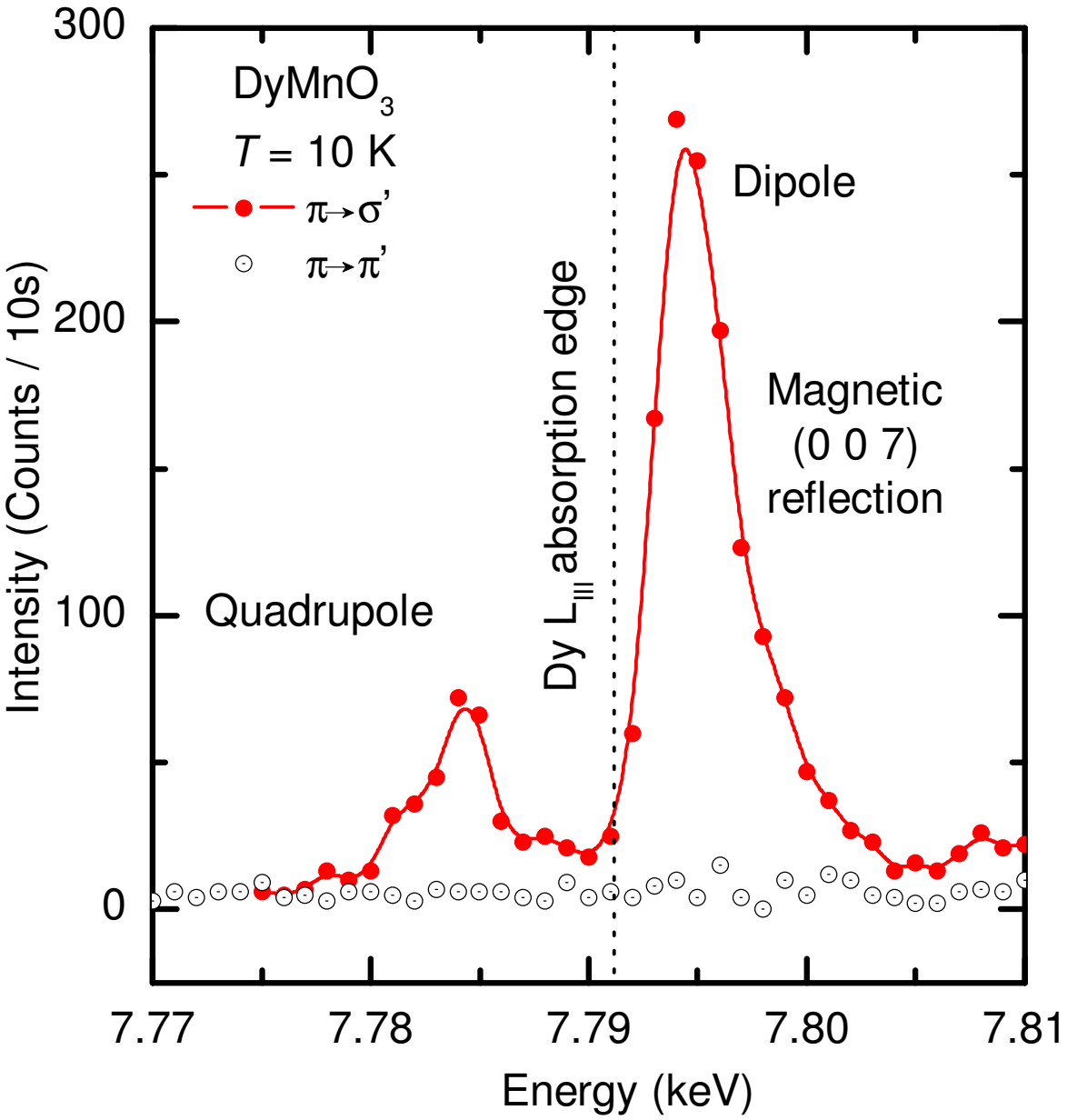

Figure 3.17 Energy scans of the magnetic (0 0 7) reflection through the Dy L_{III} absorption edge for the two polarization channels $\pi \rightarrow \sigma^{'}$ and $\pi \rightarrow \pi^{'}$.

of Mn^{3+} in $HoMnO_3$) in the ITP.

The magnetic structure in the low temperature phase

We now turn to the investigation of the magnetic structure in the LTP where the magnetic intensity of the (0 0 9) reflection goes to zero (see Fig. 3.15). Referring again to Table 2.8, we can readily exclude the magnetic representations Γ_3 and Γ_6 as these reflections should yield finite intensity. The intensity of the (1 0 9) reflection also goes to zero, as shown in Fig. 3.16. This excludes the magnetic representation Γ_1 (the structure found for the LTP phase of $HoMnO_3$) for the LTP as the intensity of this reflection should be finite but large compared to ITP.[53] Therefore, the remaining possible magnetic representations are Γ_2, Γ_4 and Γ_5. These representations yield intensity at the charge allowed reciprocal lattice points (l even). Since the magnetic signal is weak compared to the charge scattering, separation of a magnetic signal from the charge signal is extremely difficult in an XRMS experiment.[70] However, we note that while Γ_4 is antiferromagnetic along the **c** direction, the representations Γ_2 and Γ_5 correspond to ferromagnetic moments along the **c** direction and in the **a-b** plane, respectively. Fig. 3.13(a) and (b) shows the magnetization measurement along and perpendicular to the **c** direction at 5 K (LTP) and 10 K (ITP). A steep rise to a sharp kink in the magnetization in the LTP for small fields ($\leq$ 1 kOe) along the **c** direction indicates a ferromagnetic moment along this direction, consistent with the reported results of Ivanov *et. al.*[39] Therefore, magnetization measurements together with XRMS measurements suggest that Γ_2 is the magnetic representation in the LTP. According to this representation the Dy^{3+} moments at each site are ferromagnetically aligned but the correlation between them can be parallel (ferromagnetic) or antiparallel (ferrimagnetic). Since the uncompensated magnetic moment along the **c** direction, determined from the extrapolation of high field magnetization data to zero field, is only $\sim 1\mu_B$ per formula unit, much less than the free magnetic moment (10.6 μ_B) of Dy^{3+}, a ferrimagnetic alignment of Dy^{3+} moments is expected. The magnetic structures corresponding to the ITP and LTP are shown in Fig. 3.18.

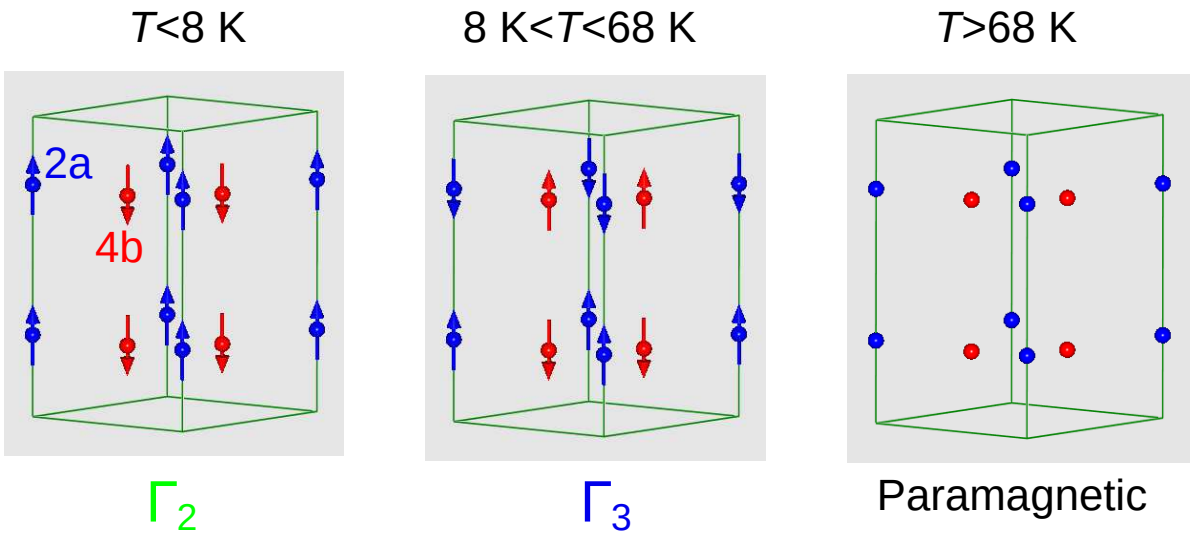

Figure 3.18 Magnetic structures of Dy^{3+} moments at different temperature range. (a) Above $T > 68$ K, the Dy^{3+} moments are in a paramagnetic state. (b) and (c) Magnetic structures of Dy^{3+} moments in the intermediate temperature phase (ITP) and in the low temperature phase (LTP), respectively.

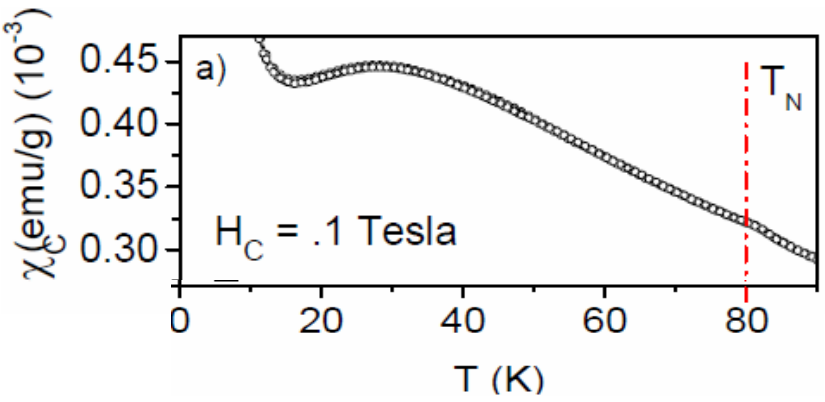

Figure 3.19 Magnetic susceptibility of $ErMnO_3$ measured with a magnetic filed along the **c** axis. After Ref. [91]

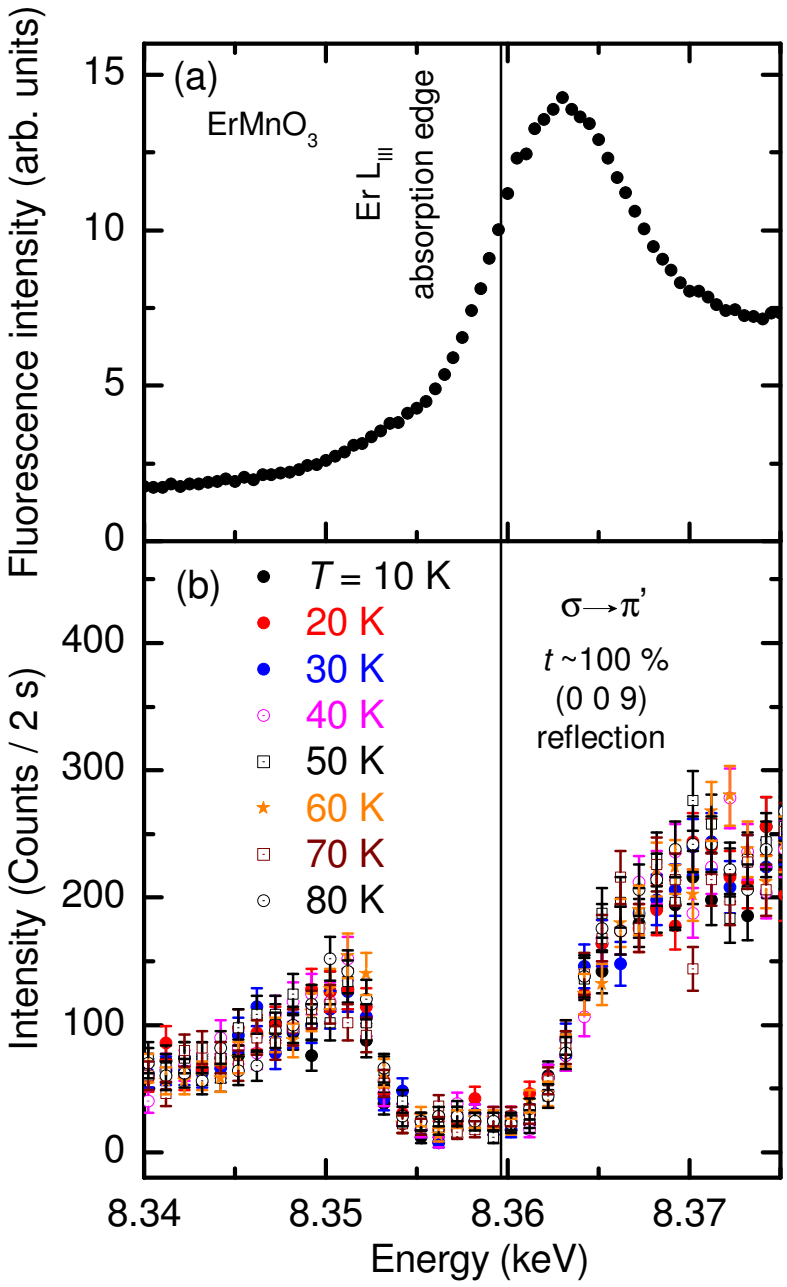

Figure 3.20 (a) Energy scan of the fluorescence signal. The dashed line depicts the Er L_{III} absorption edge as determined from the inflection point of the fluorescence signal. (b) Energy scan of the (0 0 9) reflection at several temperatures.

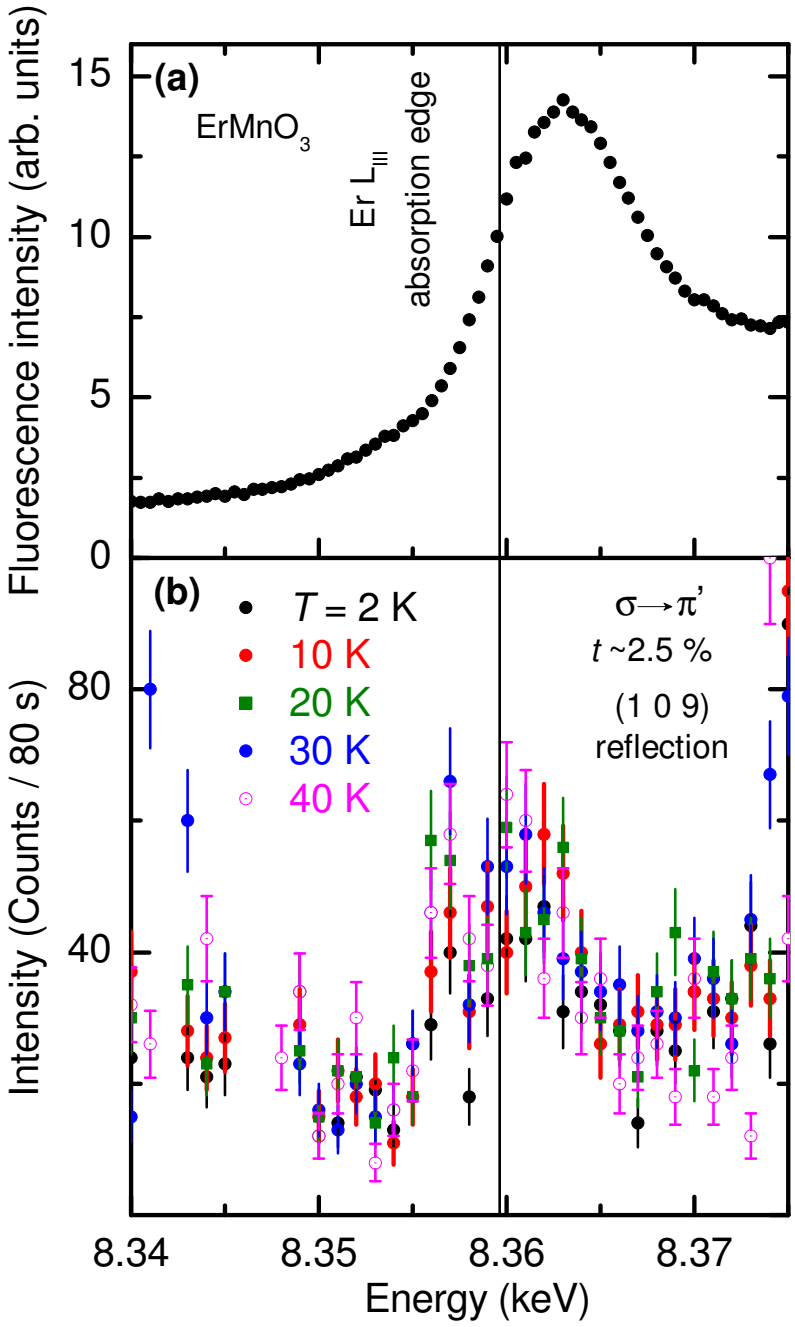

Figure 3.21 (a) Energy scan of the fluorescence signal. The dashed line depicts the Er L_{III} absorption edge as determined from the inflection point of the fluorescence signal. (b) Energy scan of the (1 0 9) reflection. The intensities at 8.340, 8.346 (out-side of the scale) and 8.375 keV are due to multiple charge scattering.

3.2.4 Magnetic Structure of Er^{3+} in $ErMnO_3$

As discussed above, there are two proposals for the magnetic order of Er^{3+} moments in $ErMnO_3$. Sugie *et al.*[44] proposed the magnetic representation Γ_6 (moments in the **a-b** plane) whereas Fiebig *et al.*[99] proposed magnetic representation Γ_2 (moments along the **c** direction) below approximately 6 K. Magnetization data in Fig. 3.19 shows a kink and an upturn around 80 and 13 K, respectively. Specific heat data shows phase transitions at 3 K and 80 K[112] and the transition at $T = 80$ K was identified with the magnetic ordering of the Mn^{3+} moments.[99, 115] Magnetization data, in addition, shows an irreversibility at 50 K between zero-field cooled data and field cooled data.[112] A similar irreversibility was observed for $HoMnO_3$ at around 40 K,[112] but the origin of the irreversibility is unknown. However, as we know now that the Ho^{3+} moments order below 40 K, irreversibility in magnetization below 50 K for $ErMnO_3$ may originate from the magnetic ordering of Er^{3+}. To shed light on the low temperature magnetic structure and to check if the origin of irreversibility is associated with magnetic ordering of Er^{3+} moments below 50 K, we have performed an XRMS experiment at the Er L_{III} edge. The experimental details are very similar to $HoMnO_3$ and $DyMnO_3$ and have been discussed before.

Magnetic structure in the temperature range 3 K$\leq T \leq$ 80 K

Similar to the measurements for $HoMnO_3$ and $DyMnO_3$, we measured (h 0 l) and (0 0 l) reflections with l = odd to distinguish between different magnetic structures. Specifically, (h 0 l) reflections with l = odd, are sensitive to the Γ_1, Γ_3 and Γ_6 magnetic representations whereas (0 0 l) reflections with l = odd, are sensitive to the Γ_3 representation (see Table 2.1.3.3). From figure 3.20, which shows energy scan through the (0 0 9) reflection at several temperatures, it is clear that the resonance features are absent for this reflection and, also, the observed signal in the vicinity of the absorption edge is temperature independent. Therefore, intermediate temperature phase (between 3-80 K) with magnetic representation Γ_3, that we have observed for Dy^{3+} and Ho^{3+} in the corresponding temperature ranges (8-68 K for Dy^{3+} and 4.5-40 K for Ho^{3+}), does *not* exist for Er^{3+}. To check the possibility of magnetic ordering according to the remaining representations, we have measured energy scans through the (1 0 9) reflection

shown in Fig. 3.21. A very weak resonance feature is present at the absorption edge. However, the intensity of this feature is temperature independent, pointing to the non-magnetic origin. Therefore, magnetic ordering according to the Γ_1 and Γ_6 representations can be excluded. The remaining possibilities are Γ_2, Γ_4 and Γ_5. As we mentioned for the LTP of $DyMnO_3$ that these representations yield intensity at the charge allowed reciprocal lattice points (l even) and extremely difficult to measure in an XRMS experiment.[70] However, we note that while Γ_4 is antiferromagnetic along the **c** direction, the representations Γ_2 and Γ_5 correspond to ferromagnetic moments along the **c** direction and in the **a-b** plane, respectively. No ferromagnetic signal has been observed above 3 K in the magnetization measurement,[112] therefore, Γ_2 and Γ_5 representations can be also excluded. The only possible magnetic representation in this temperature range is Γ_4. Since powder neutron diffraction measurements, performed by Park *et al.*[115] in the temperature range 10-85 K, have not found any signature of magnetic ordering of Er^{3+}, it is likely that Er^{3+} moments are paramagnetic in this temperature range.

Magnetic structure below $T \leq$ 3 K

Below 3 K, following the same argument presented above, magnetic ordering according to Γ_1, Γ_3 and Γ_6 representations can be excluded based on our XRMS experiment. The remaining possible magnetic representations are again Γ_2, Γ_4 and Γ_5. Observation of ferrimagnetic response and/or steep increase in magnetization[44, 99, 112] for small fields along the **c** direction, similar to that of $DyMnO_3$, supports a ferrimagnetic alignment of the Er^{3+} moments according to the magnetic representation Γ_2 below 3 K. Therefore, magnetization measurements together with XRMS measurements suggest that Γ_2 is the magnetic representation in the LTP.

3.2.5 Conclusions

In summary, we have determined the magnetic structure of Dy^{3+} moments in $DyMnO_3$ to be Γ_3 in the intermediate temperature magnetic phase, ITP (between 68 K and 8 K). The Dy^{3+} moments are aligned and antiferromagnetically correlated along the **c** direction. The temperature dependence of the magnetic intensity in the ITP can be explained by assuming a splitting of the ground state doublet by the exchange field from the ordered Mn^{3+} moments. In the

low temperature phase, LTP (below 8 K), XRMS together with magnetization measurements indicate that Γ_2 is the magnetic representation and the Dy^{3+} moments are ferrimagnetically aligned in the hexagonal **c** direction. We note that the magnetic structure in $DyMnO_3$ is the same as in $HoMnO_3$ in the ITP, however, in the LTP the magnetic order is different: the Ho^{3+} moments are antiferromagnetically aligned according to Γ_1 in contrast to the ferrimagnetic alignment of the Dy^{3+} moments in $DyMnO_3$. It is likely that the striking difference is due to the complex interplay between the magnetism of the two sublattices, Dy^{3+}/Ho^{3+} and Mn^{3+}. For $ErMnO_3$, we conclude that no ITP exists and the Er^{3+} moments order ferrimagnetically below 3 K according to magnetic representation Γ_2.

3.3 Origin of Magnetic Ordering and Different Magnetic Phases in RMnO$_3$: Superexchange Interaction

The different magnetic phases of rare-earth R^{3+} as well as Mn^{3+} moments together with the characteristic transition temperatures are summarized in Fig. 3.23. The ordering temperature of the Mn^{3+} moments in $HoMnO_3$ and $ErMnO_3$ are taken from literature.[112] The ordering temperature of Mn^{3+} moments in $DyMnO_3$ is not known from scattering experiments. However, from the specific heat data of a $DyMnO_3$ single crystal shown in Fig. 3.22 two phase transitions at high temperatures at 67.5 K and 64.5 K,[6] respectively, are discernable. We associate the higher transition temperature (67.5 K) with the magnetic ordering of the Mn^{3+} moments and the lower one (64.5 K) to the induced ordering of the Dy^{3+} moments by the Mn^{3+} since the observed transition temperature of Mn^{3+} moments is always higher than the rare-earths in the other hexagonal multiferroic compounds.

In the high temperature phase (HTP), only the Mn^{3+} moments are ordered according to the magnetic representation Γ_4.[45, 47, 48] In the intermediate temperature (ITP) and low temperature (LTP) phases, the rare-earth moments become ordered according to the magnetic representations shown in Fig. 3.23. In the ITP and LTP, the Mn^{3+} moments re-orient within the **a-b** plane according to the same magnetic representations as that of rare-earths.

[6]The transition temperatures have been determined from the peak in the specific heat data.

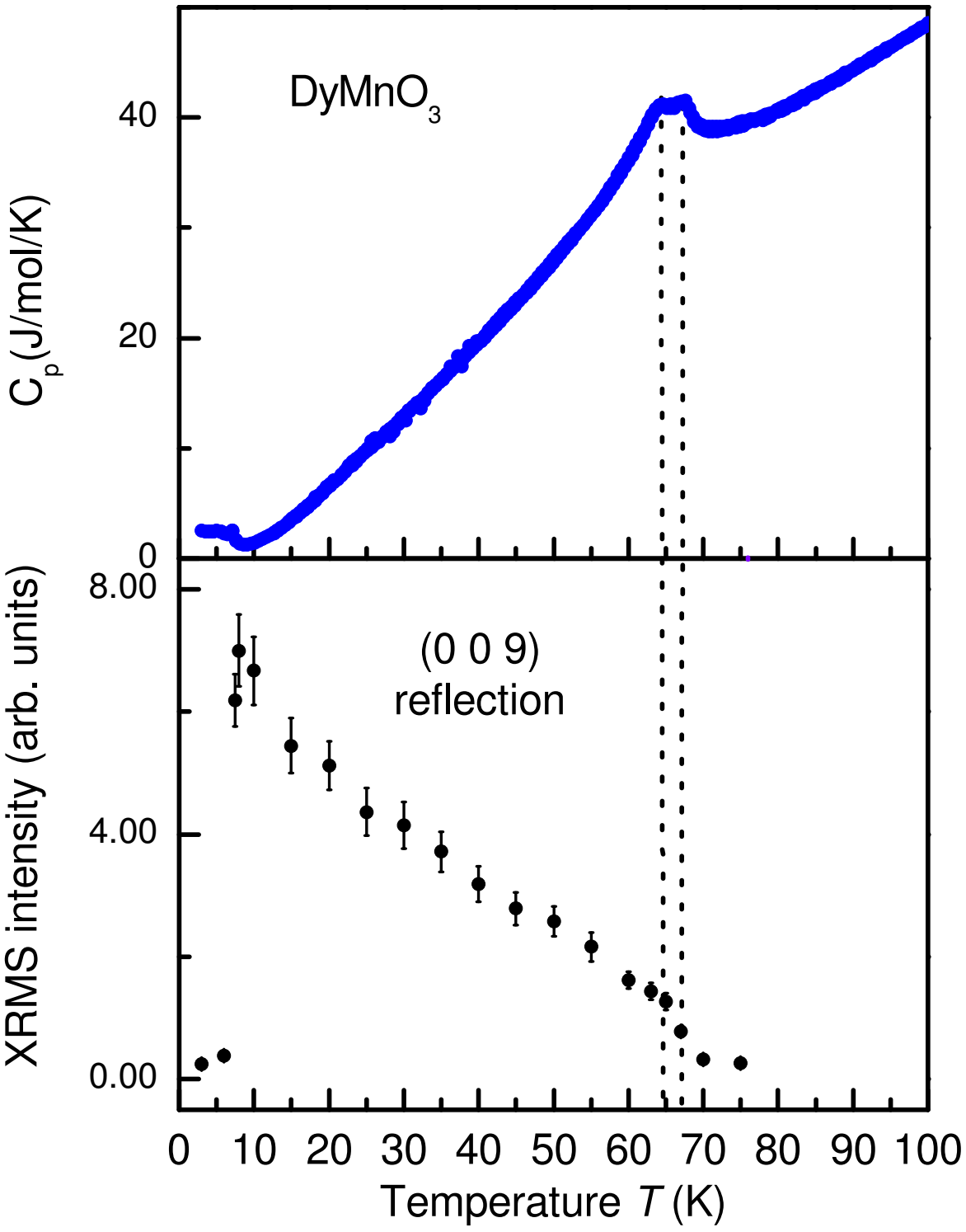

Figure 3.22 The specific heat of a $DyMnO_3$ single crystal (upper panel) and the measured XRMS intensity for the (0 0 9) reflection (lower panel).

From the diagram, we can see that the ordering temperature for the Mn^{3+} moments increases from Dy to Er, and may be understood if we consider the strength of Mn-O-Mn superexchange interaction across the series. The superexchange interaction depends on the overlap between the Mn $3d$ and O $2p$ orbitals and therefore, should scale with the distance between the Mn and O ions in the plane. We note that the superexchange interaction also depends on the bond angle Mn-O-Mn. However, the bond angle is the same across the series due to the special Wyckoff position ($4b$) of the in-plane oxygen ions. The in-plane lattice parameter decreases from Dy to Er, and therefore, the overlap between the Mn($3d$) and O($2p$) increases across the series. Hence, the ordering temperature for the Mn^{3+} moments increases across the series.

Considering the ITP, the Dy^{3+} and Ho^{3+} moments order according to the same magnetic representation Γ_3 whereas no such magnetic structure could be found for the Er^{3+}. For both the Ho^{3+} and Dy^{3+}, magnetism in the ITP can be explained assuming an exchange interaction between R^{3+} and Mn^{3+} and a splitting of the R^{3+} ground state quasi-doublet/doublet by this exchange field. We note that the crystal electric field splitting for Dy ($\sim$6 meV) is larger than that of Ho ($\sim$1.3 meV), consistent with the larger ordering temperature for Dy^{3+} and points to a stronger exchange interaction between Dy^{3+} and Mn^{3+} than between Ho^{3+} and Mn^{3+}. The ordering in the ITP is controlled by R-O-Mn interaction. Since the rare-earth $4f$ levels are well localized, the interaction between rare-earths and Mn is mediated by $5d$'s of the rare-earths. Therefore, the interaction strength in a $R\mathrm{MnO_3}$ series is determined by the $4f$-$5d$ exchange. In a naive picture, the $4f$-$5d$ overlap decreases for the heavy rare-earths due to lanthanide contraction and, therefore, one might expect that the strength of interaction decreases with increasing number of $4f$ electrons. In this picture, the absence of a scattering signal is quite consistent with the expectation that Er^{3+} should order at much lower temperature due to the smallness of exchange interaction between Er^{3+} and Mn^{3+}.

We also note that the transition temperature to the LTP decreases as we go from Dy to Er (8 K for Dy, 4.5 K for Ho, 3 K for Er).[7] The ordering in the LTP is controlled by R-R

[7]We have compared ordering temperatures from samples grown by the same floating zone technique. Flux grown samples show slightly different transition temperatures.

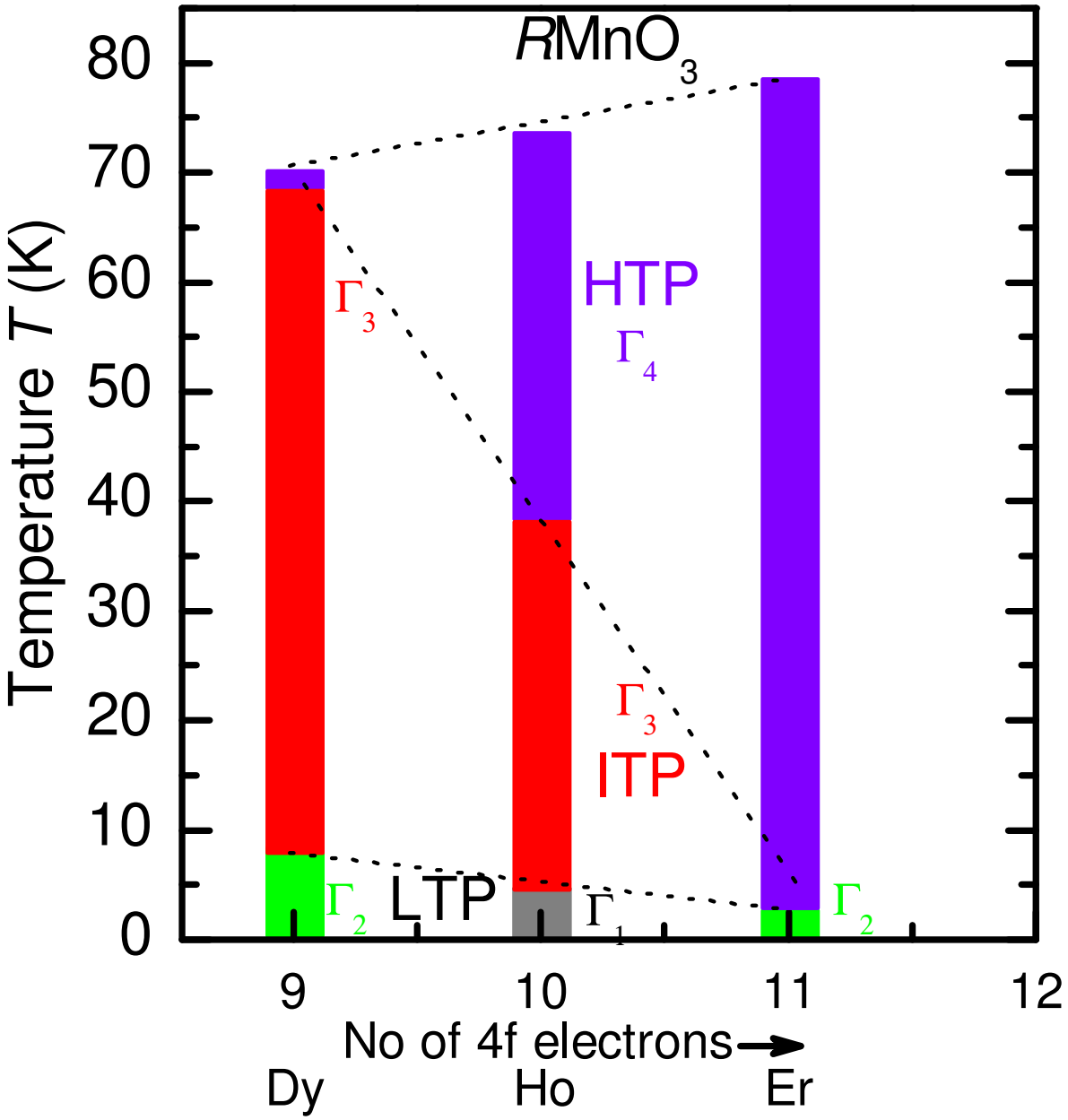

Figure 3.23 Magnetic representations of the rare-earths R^{3+} as well as Mn^{3+} moments. In the HTP (high temperature phase) only Mn^{3+} moments are ordered. In the ITP (intermediate temperature phase) and LTP (low temperature phase) the rare-earths become ordered. The magnetic representations of the ITP and LTP are same for both magnetic sublattices, R^{3+} and Mn^{3+}. The dotted lines indicate the trend observed across the rare-earth series for the ordering temperatures of R^{3+} and Mn^{3+} moments. The ordering temperature for Er^{3+} is taken from Ref. [112].

exchange. In this case, $4f$-$4f$ direct exchange is not possible due to the localized nature of $4f$ electrons and therefore, R-R interaction must be mediated by $5d$'s as in the ITP. Hence, the ordering temperature should decrease from Ho^{3+} to Er^{3+} for the same reason as mentioned above for the ITP.

The frustration at the Ho($2a$) site for the Γ_1 representation (the low temperature phase of Ho^{3+}), and the stabilization of the LTP according to the magnetic representation Γ_2 for the Dy^{3+} and Er^{3+} can be understood by considering the nearest neighbor R-R exchange interaction. The Ho($2a$) site in the Γ_1 representation is surrounded by equal number of up and down Ho(4b) moments and, therefore, the net interaction at the Ho($2a$) site vanishes, keeping Ho($2a$) moments frustrated if the size of the moment at the Ho(2a) site is not zero, i.e. not a singlet ground state. In the LTP with the representation Γ_2 for Dy^{3+} and Er^{3+}, frustration at the $R(2a)$ site can be overcome as shown in Fig. 3.24(b). Here, the $R(2a)$ moments are surrounded by six up $R(4b)$ moments. Therefore, a down moment at the $R(2a)$ site is preferred, considering antiferromagnetic nearest neighbor interactions.

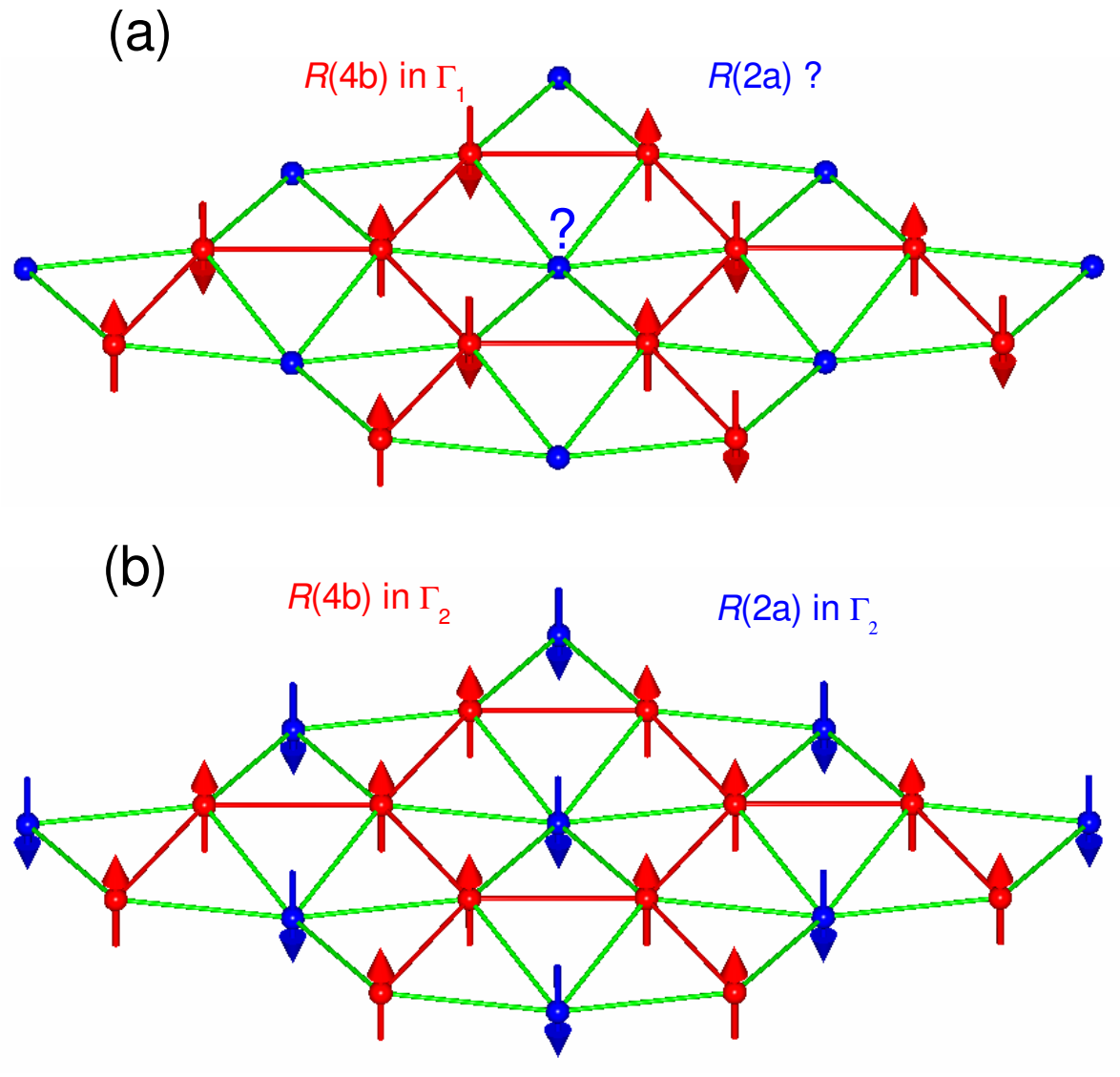

Figure 3.24 Arrangement of R^{3+} moments in the **a-b** plane for the low-temperature phase (LTP). (a) The Ho($4b$) moments are ordered according to magnetic representation Γ_1. Ho($2a$) moments are frustrated assuming non-zero magnetic moment. (b) The low temperature phase of Dy^{3+} and Er^{3+} according to the magnetic representation Γ_2.

CHAPTER 4. THE MAGNETIC ORDER OF $HoMnO_3$ IN AN APPLIED ELECTRIC FIELD

4.1 Introduction

Magnetoelectric multiferroic compounds, systems which exhibit both ferroelectric and magnetic effects within the same phase, have attracted considerable attention due to the potential for controlling electric polarization by an applied magnetic field[20] or, conversely, magnetic order through an applied electric field.[9] Recently, such a mechanism has been proposed for hexagonal $HoMnO_3$.[9] Despite numerous studies, however, the exact role that the Ho^{3+} ions play in the magnetic response, and the details of the magnetic ordering of the Ho^{3+} sublattices remain unclear.[41, 42, 44, 46, 48]

In the previous chapter we resolved the controversies of the zero field magnetic structures of the rare-earth moments through a detailed analysis of the XRMS data. Apart from the complex magnetic structures of the rare-earths in these compounds, perhaps of strongest interest is the proposal by Lottermoser *et al.*[9] that the application of an electric field changes the antiferromagnetic order of Ho^{3+} to ferromagnetic order, with the representation Γ_2, over the temperature range from 2 K to 76 K, based on SHG and optical Faraday rotation experiments.

To investigate the nature of the Ho^{3+} magnetic ordering in an applied electric field, we have performed magnetization measurements using SQUID magnetometer and studied element specific changes in magnetization using x-ray resonant magnetic scattering (XRMS) and x-ray magnetic circular dichroism (XMCD). The XRMS and XMCD experiments were performed at the Ho L_{III} absorption edge ($E = 8.071$ keV). For comparison, XMCD measurements on powder samples were also performed with another member of the series, $DyMnO_3$, at the Dy L_{III} absorption edge ($E = 7.790$ keV).

In the XRMS experiment, the scattering process involves an intermediate state which arises from either dipole (E1) allowed ($2p$ – $5d$) or quadrupole (E2) allowed ($2p$ – $4f$) electronic excitations.[58, 60] In ordered rare-earth magnetic materials, the technique is sensitive to the magnetization density through either the $4f$ electronic states directly (E2) or indirectly through the $4f$ – $5d$ exchange interaction (E1). Of importance here is that since this technique is element specific we can probe the magnetic structure associated with the Ho^{3+} moments directly. In the closely related XMCD measurements, the signal is defined as the difference in the absorption of left and right circularly polarized x-rays by a magnetized sample.[81] Since XMCD measurements are also performed at the absorption edges of elements of interest they can be viewed as measurements of the net magnetization for a specific elemental constituent of a magnetic compound, for example, measuring the contribution of Ho^{3+} to any ferromagnetic response of the sample.

4.2 Experimental Details

The sample pictures and preparations for the electric field measurements are shown in Fig. 4.1. For the SQUID magnetization measurements a thinned sample of $HoMnO_3$ with typical thickness of 130 μm was used. The sample was painted with the silver (Ag) paint on both sides and mounted on the stick of the SQUID magnetometer using the same silver paint. The silver paint act as an electrode for these measurement. The XRMS experiment was performed on the 6ID-B beamline at the Advanced Photon Source at the Ho L_{III} absorption edge using the same sample as used for magnetization measurements. For the XRMS experiments two different types of electrodes, gold (Au) as well as silver (Ag) were used. The sample was mounted on the cold-finger of a displex cryogenic refrigerator with the $\mathbf{a}^*$-$\mathbf{c}^*$ reciprocal plane coincident with the scattering plane. With the incident beam polarized perpendicular to the scattering plane (σ-polarized), measurements of the magnetic scattering were performed at the E1 and E2 resonances in the rotated (σ-$\pi^{'}$) scattering channel.[64] A Pyrolytic graphite PG (0 0 6) analyzer was used as a polarization analyzer to suppress the charge background (unrotated) relative to the magnetic scattering signal. The XMCD measurements were performed on the

4-ID-D beamline at the Advanced Photon Source by modulating the x-ray helicity at 11.3 Hz with a thin diamond phase retarder and using an lock-in amplifier to detect the related modulation in the absorption coefficient. Spectra were recorded from a 20 μm thin single crystal of $HoMnO_3$ coated with carbon as electrodes, and on powder samples of $HoMnO_3$ and $DyMnO_3$ spread over several layers of tape and then sandwiched between two layers of conducting aluminized mylar (total sandwich thickness of 280 μm). The samples were mounted on the cold finger of a horizontal field cryomagnet.

Study of Changes in the Bulk Magnetization: SQUID Magnetometery

The magnetization measurements were performed in the following sequence:

1. The sample was first cooled in both zero electric and magnetic fields from room temperature to base temperature, $T = 10$ K. Then a magnetic field (H) of 500 Oe was applied along the **c** direction and the magnetization was measured on heating up to $T = 90$ K.

2. The sample was cooled again to base temperature in the absence of any applied fields. Then both electric and magnetic fields of 500 Oe and 400 Volts, respectively, were applied along the **c** direction and magnetization was measured on heating up to $T = 90$ K.

3. The sample was cooled from 90 K to base temperature with both fields applied and magnetization was measured on cooling.

Figure 4.2 shows the results of the measurements described above. Specifically, magnetization measured with applied voltage is same as that with the zero voltage and the results are independent of the measurement sequence. From the magnetization measurements, we conclude that the bulk magnetization remain unchanged in an applied voltage of 400 Volts (Electric field, $E = 3\times10^6$ V/m).

One of the difficulties of the SQUID measurements was that voltages higher than 400 Volts could not be applied in the investigated temperature range, possibly due to the presence of He gas inside the SQUID magnetometer. Lottermoser *et al.*[9] reported measurements in an applied electric field of 1×10^7 V/m, which, according to their claim is one order of magnitude

higher than the required electric field to induce ferromagnetism. Therefore, an applied electric field E of 3×10^6 V/m should be enough to induce ferromagnetism.

Nevertheless, to obtain the same order of magnitude of the electric field that Lottermoser *et al.*[9] applied, and to see if Ho is responsible for the ferromagnetic response, we have performed element specific XRMS and XMCD measurements. For the XRMS experiments, a displex cryogenic refrigerator was prepared with the capability of applying high voltage. Since the sample is directly connected to the cold finger of the displex, measurements can be performed without any He exchange gas for the XRMS experiment. The sample was maintained under a vacuum of 2×10^{-6} mbar to avoid any discharge due to the presence of gaseous elements. The XMCD experiments were performed inside the horizontal field cryomagnet which is also under vacuum. Since the beam heating effects described before, particularly in the absence of any exchange gas, may be a concern in these experiments, we note that the metallic electrode (Ag or Au) on top of the sample reduces the beam heating by attenuating the incident beam as well as conducting the heat load across the sample.

Study of Element Specific Changes in Antiferromagnetism: X-ray Resonant Magnetic Scattering

We first confirmed the zero filed magnetic structure by measuring resonance enhancements and temperature dependence of the (0 0 9) reflection as a function of temperatures shown in Fig. 4.3 and Fig. 4.4, respectively. The observation of finite intensity for the (0 0 9) reflection and the close similarity to the measured temperature dependence for the sample without electrodes confirmed that the sample with electrodes behave very similar to the samples without any electrodes used for the zero field study. Specifically, in the temperature range 10−39 K, Ho^{3+} moments are antiferromagnetic along the **c** direction according to magnetic representation Γ_3.

After re-confirming the magnetic structure in zero field, we measured the temperature dependence of both the dipole and quadrupole resonances in an applied electric field. For these measurements, thinned (130 μm) samples coated with silver as well as gold (as electrodes) were used. Fields of up to 1×10^7 V/m, well above the saturation value reported by Lottermoser *et*

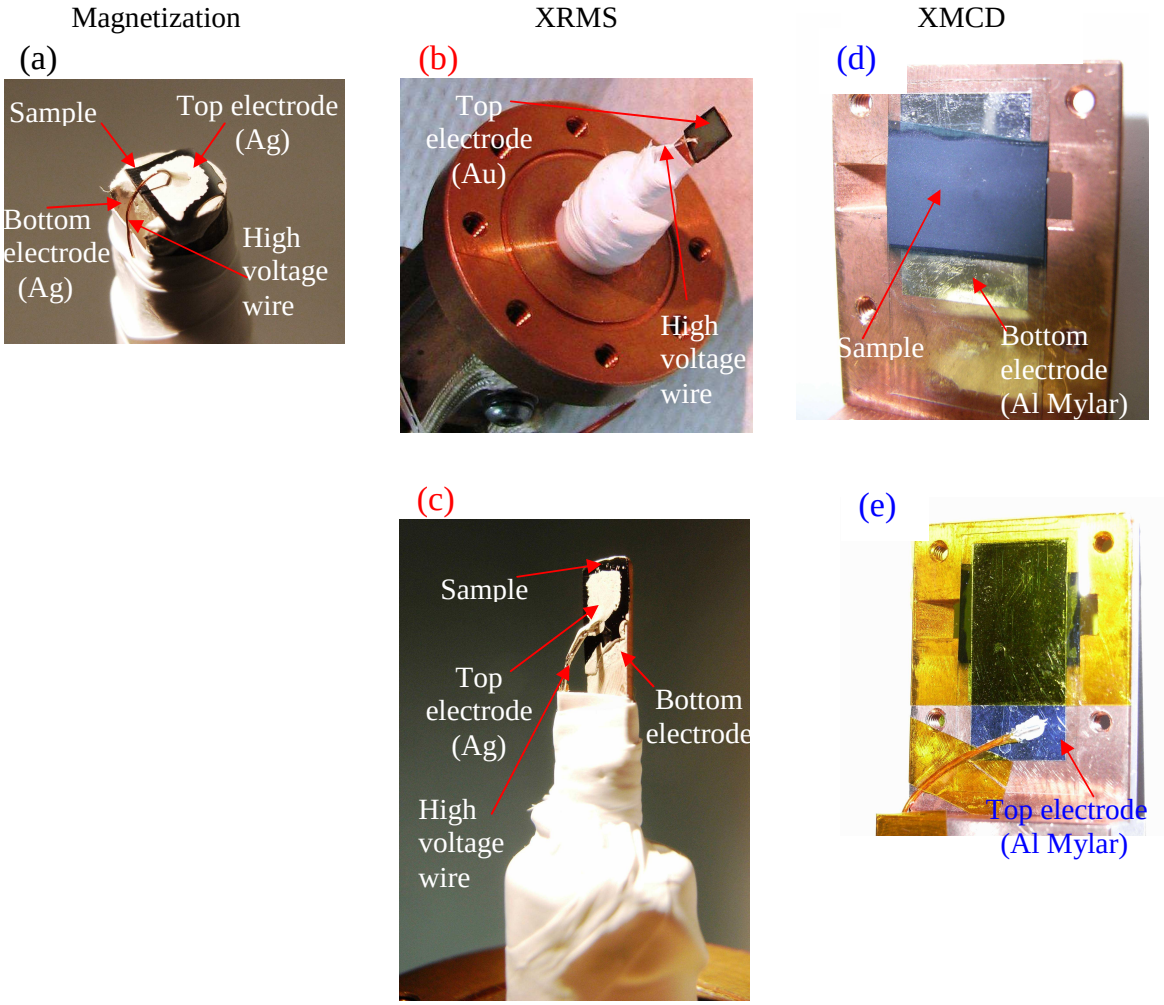

Figure 4.1 (a) Sample (black) is glued on top of the wooden stick with silver paint (white) (acting as a bottom electrode). A portion of the top of the sample is also covered with silver paint (white) which acts as a top electrode. The high voltage wire was connected to this top electrode with the silver paint. Being mounted on the wooden stick, a wire was connected to the bottom electrode which acts as a ground. The wire is embedded in the silver paint and invisible in the picture. (b) Sample coated with the gold electrode and (c) sample coated with the silver electrode. Both the samples were mounted on the Cu pin with silver paint. The Cu pin was connected to the ground and acts as a bottom electrode (d) Powder sample (black) spread over scotch tapes without top electrode. (e) The sample is covered with aluminized mylar which acts as a top electrode. The sample was fixed with capton tapes (yellow) with the sample holder and the sample holder was grounded.

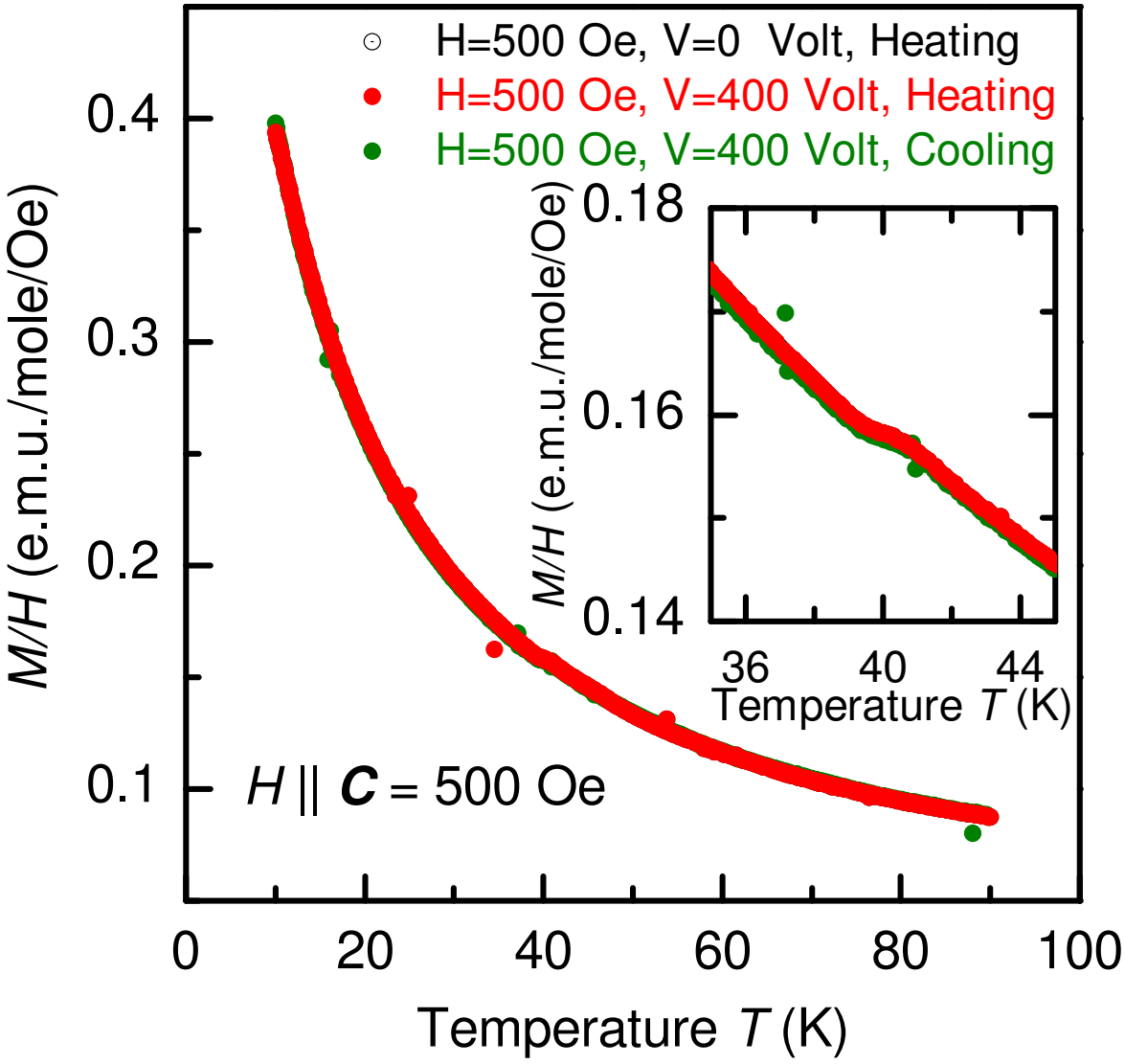

Figure 4.2 Magnetization of $HoMnO_3$ measured with and without applied voltage (electric fields).

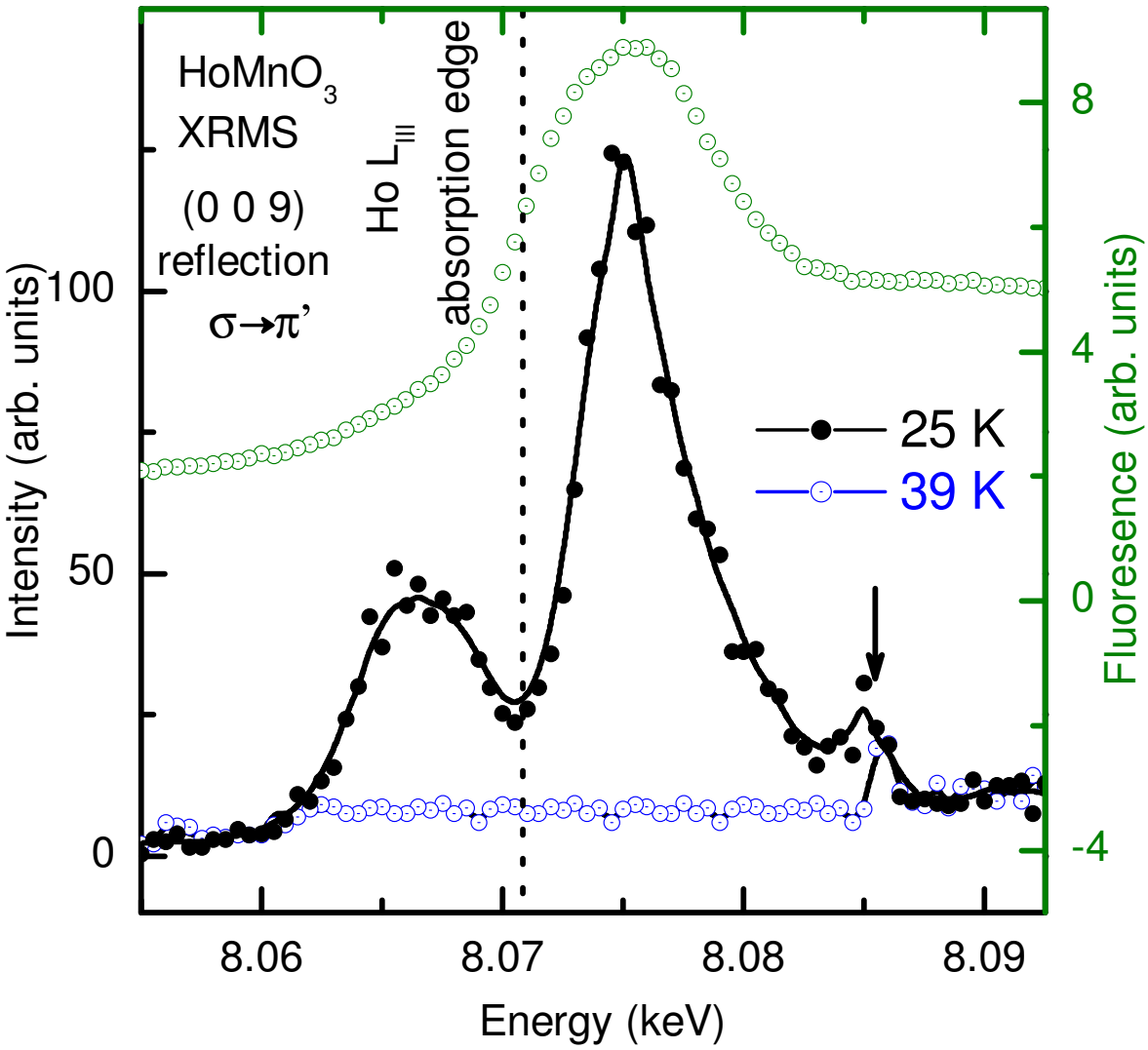

Figure 4.3 Energy scans for the magnetic (0 0 9) reflection and the fluorescence spectra through the Ho L_{III} absorption edge. The solid lines are guides to the eye. The small peak marked by a vertical arrow is due to multiple charge scattering.

al.[9], were obtained for an applied voltage of 1500 V. Figure 4.4 shows that there is no difference between the temperature dependence of the peak intensity in zero and the maximum applied electric field. Further, the inset to the Fig. 4.4 shows that there are no gross structural changes in this applied field since the peak position and the full width at half maximum remain same. We conclude that there is no change of the antiferromagnetic structure of Ho^{3+} in an applied electric field in the ITP.

Study of Element Specific Response of Ferromagnetism: X-ray Magnetic Circular Dichroism

Since the XRMS measurements probe only antiferromagnetic order and are not sensitive to small ferromagnetic components of the ordered magnetic moment, we have also performed (XMCD) measurements at the Ho L_{III} edge on single crystal and powder samples of $HoMnO_3$ and at the Dy L_{III} edge on powder sample of $DyMnO_3$. The single crystal sample of 20 μm thickness was too thick for absorption measurements in transmission geometry. However, since the fluorescence spectra from the sample is proportional to the absorption, we measured the fluorescence spectra, instead. Figure 4.5 shows the measured fluorescence spectra for both zero and applied electric fields. In the following measurements, XMCD is defined as:

$$\begin{aligned} \text{XMCD} &= \text{Flipping ratio} \\ &= \frac{[I(\text{r.c.p}) - I(\text{l.c.p})]}{[I(\text{r.c.p}) + I(\text{l.c.p})]} \end{aligned} \tag{4.1}$$

where r.c.p and l.c.p stand for the right circularly polarized and left circularly polarized light, respectively. The flipping ratio was calculated from the raw data in Fig. 4.5(a) according to the above equation and shown in Fig. 4.5(b). It is clear from Fig. 4.5 that the XMCD is unaffected by applied electric fields of up to approximately 1.25×10^7 V/m for single crystal sample.

We have also studied powder samples in transmission geometry for both $HoMnO_3$ and $DyMnO_3$ and, to confirm that we are able to see ferromagnetic signal by XMCD measurements, we applied a magnetic field and measured the XMCD signal. Fig. 4.6(a) and 4.7(a) show the results of these measurements. Though, these materials are not ferromagnetic in both zero

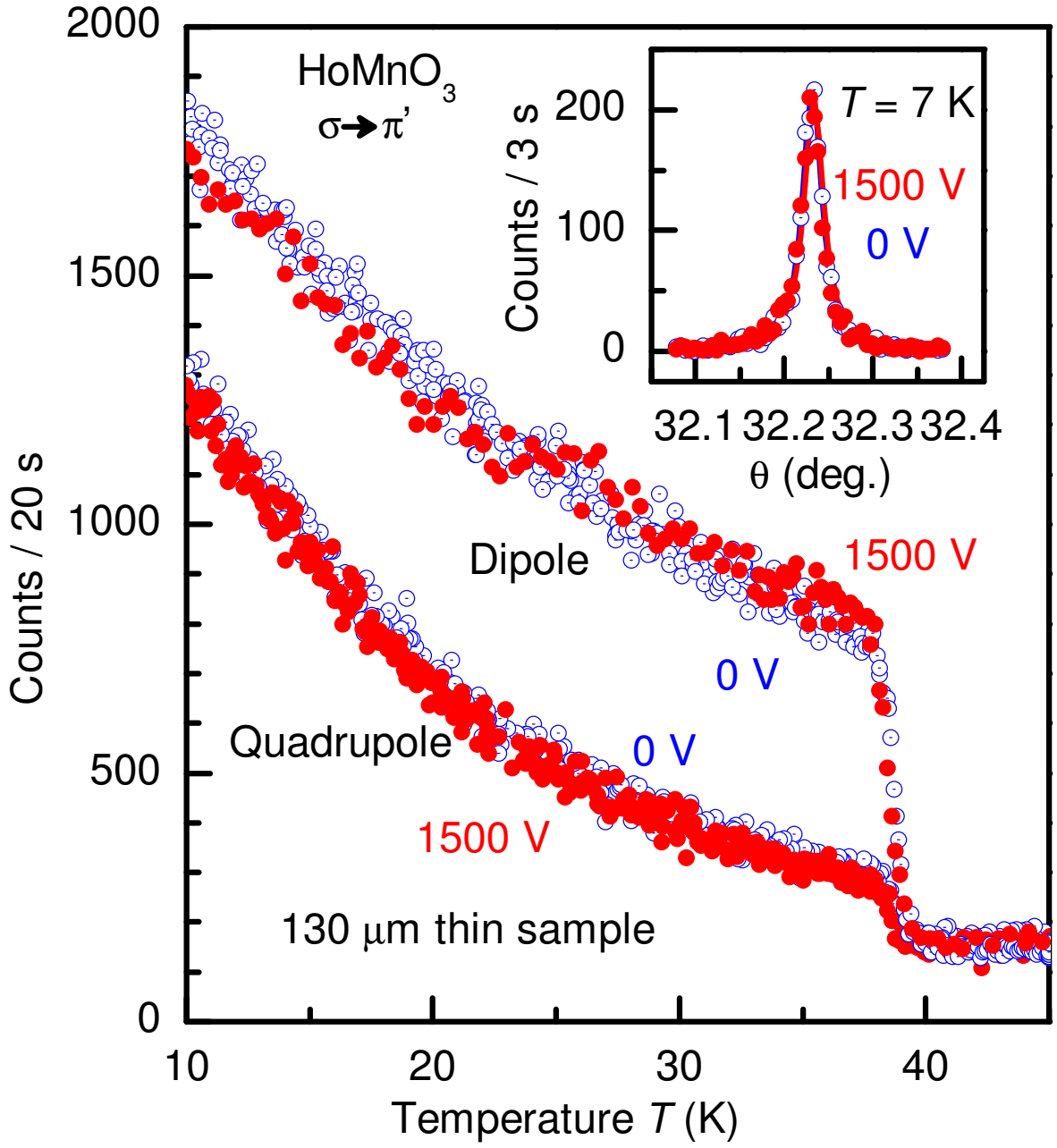

Figure 4.4 Effect of an applied electric field on the (0 0 9) antiferromagnetic peak. Inset: rocking scans at 0 V and 1500 V for the quadrupole resonance at 7 K.

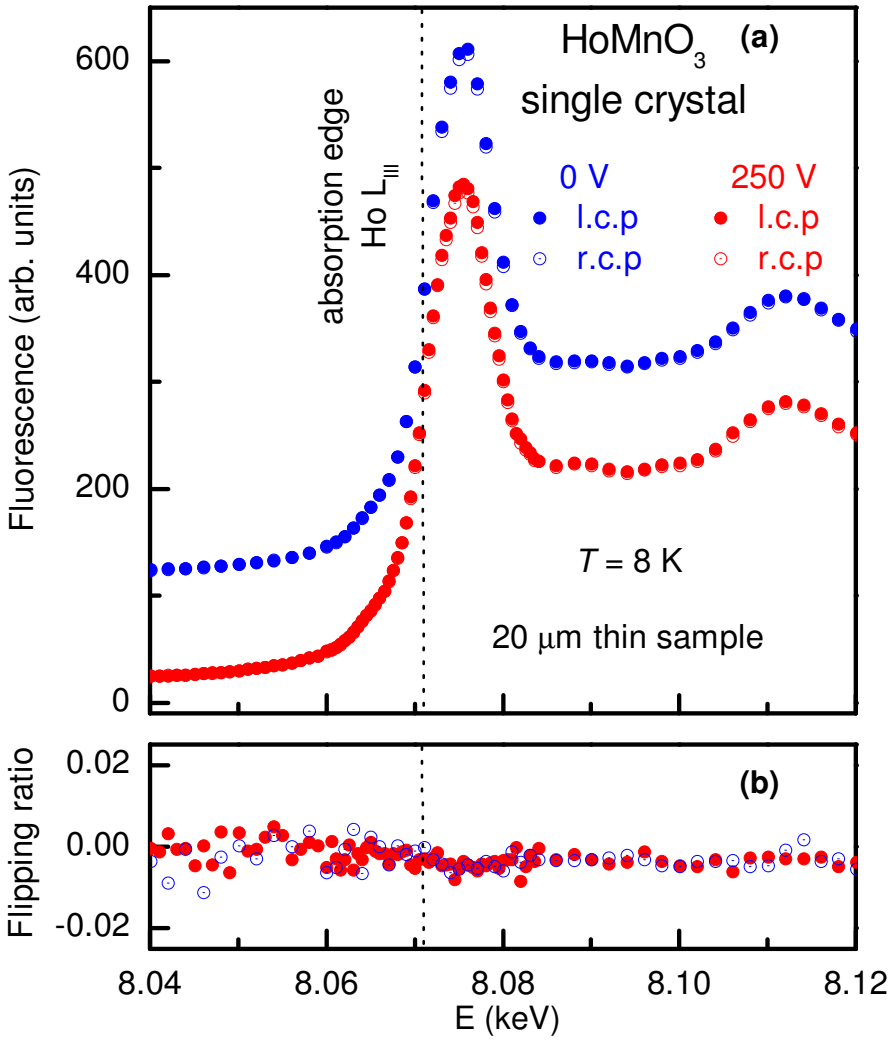

Figure 4.5 (a) Fluorescence spectra at the Ho L_{III} edge with applied electric fields and without any fields, measured on a single crystal sample at 4ID-D. (b) The flipping ratio is calculated from the spectra in (a)

and applied magnetic fields, a component of magnetic moment along the field direction can be induced by an external magnetic field. The induced component is very similar in origin to that of SQUID magnetization measurements except, in XMCD, we are measuring only the rare-earth element contribution instead of contributions from both R^{3+} and Mn^{3+}. Comparing the SQUID magnetization measurements, and the ability to observe signal in XMCD measurements in the lowest fields of 0.25 Tesla, we conclude that the present XMCD measurements are sensitive to magnetic moment $\geq 0.1\mu_B$ per formula unit. Further, the magnetic origin of the XMCD features was confirmed by the observation that the spectrum flips upon reversal of the applied magnetic field as shown in Fig. 4.6(a) and 4.7(a) for $HoMnO_3$ and $DyMnO_3$, respectively. The spectra for positive and negative magnetic fields in Fig. 4.6(a) and 4.7(a) were combined and shown in Fig. 4.6(b) and 4.7(b). The spectra were recorded following the same procedure for applied positive and negative electric fields and the combined spectra are shown in Fig. 4.6(b) and 4.7(b), together with the zero reference signal where no fields were applied. From Fig. 4.6(b) and 4.7(b), it is clear that the XMCD signal is unaffected by applied electric fields of up to approximately 1×10^7 V/m. Many other spectra were collected with all combinations of ($\pm$H, $\pm$E) between 8 and 80 K showing the same result.

4.3 Conclusion

From the extensive single crystal SQUID magnetization, XRMS and XMCD as well as XMCD on powder samples for two different hexagonal multiferroics, we conclude that there is no net ferromagnetic alignment of the Ho^{3+} with the application of an electric field as reported by Lottermoser *et al.*[9] We note that techniques used by Lottermoser *et al.*, namely, second harmonic generation and Faraday rotation, to detect ferromagnetic response of Ho^{3+} depend on the applied electric and/or magnetic fields. For example, second harmonic signal can be induced by an applied electric field[116] or Faraday coefficient can be changed by applied electric or magnetic fields or a combination of both.[117] Therefore, the signal observed by these techniques, may be an artifact of external electric field.

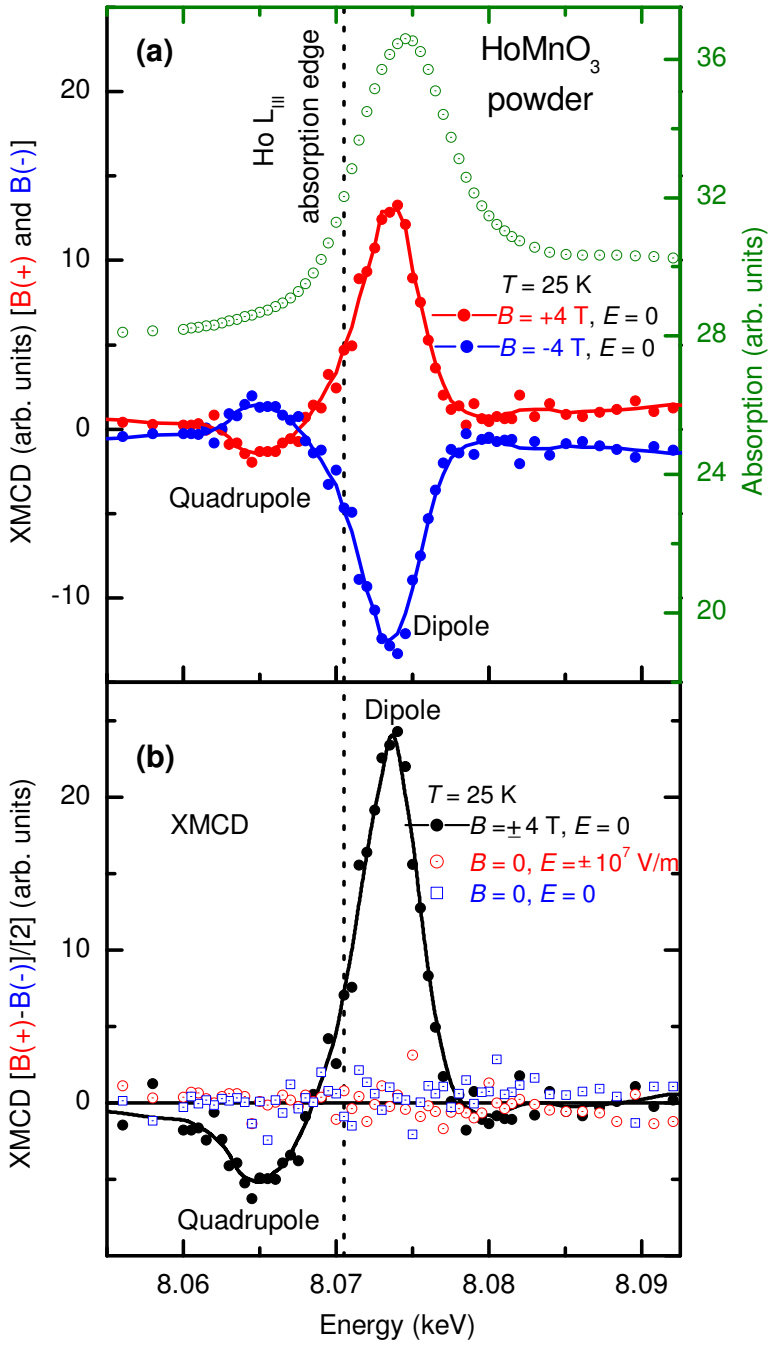

Figure 4.6 (a) Absorption spectra without any fields and XMCD spectra at the Ho L_{III} edge with applied magnetic fields measured on a powder sample at 4ID-D. (b) The combined XMCD spectra with applied magnetic fields, electric fields and without any fields.

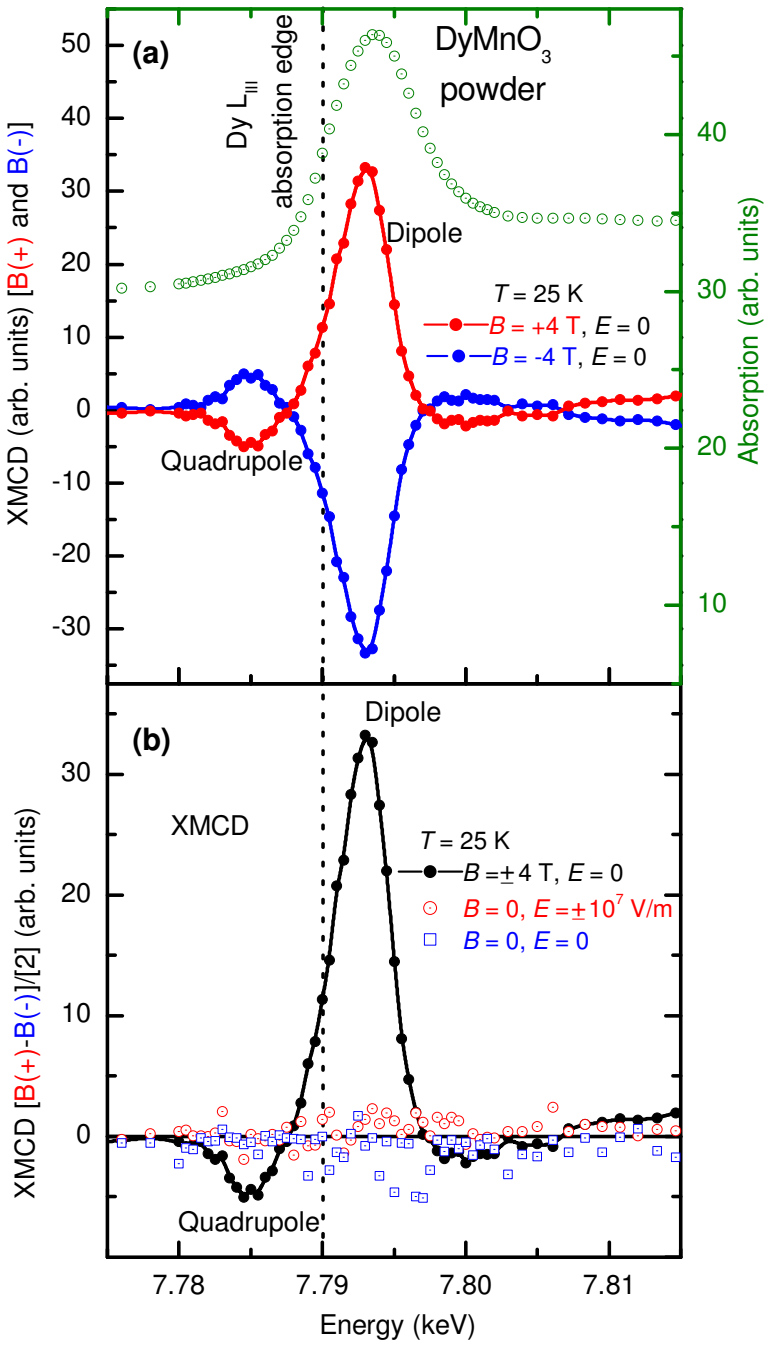

Figure 4.7 (a) Absorption spectra without any fields and XMCD spectra at the Dy L_{III} edge with applied magnetic fields measured on a powder sample at 4ID-D. (b) The combined XMCD spectra with applied magnetic fields, electric fields and without any fields.

CHAPTER 5. SUMMARY AND OUTLOOK

We have determined the magnetic structure of Ho^{3+} moments in $HoMnO_3$ by x-ray resonant magnetic scattering experiments. Specifically, we have determined that the magnetic structure of Ho^{3+} in $HoMnO_3$ to be Γ_3 in the intermediate temperature magnetic phase ITP (between 40 K and 4.5 K). The magnetic Ho^{3+} moments are aligned along the **c** axis and, at 12 K, the ratio between the magnetic moments of the Ho($2a$) and Ho($4b$) Wyckoff site is ~ -2. The moments at the Ho($2a$) site are antiferromagnetically aligned to the moments at the Ho($4b$) site in the **a-b** plane. The moments at the both sites are antiferromagnetically correlated along the **c** direction. The temperature dependence of magnetic moments in the ITP can be explained by assuming low lying crystal field levels. We also conclude that there is a change of the magnetic structure of Ho^{3+} at 4.5 K. Below 4.5 K, the magnetic phase can be well described by the co-existence of the ITP (Γ_3) with a decreasing 'ordered moment' and a new magnetic phase LTP with magnetic representation Γ_1 with a rapidly increasing Ho ($4b$) moment for decreasing temperatures. One consequence of this transition is that the Ho($2a$) moments can not order according to the representation Γ_1. Therefore, it is likely that either the Ho($2a$) moments are disordered down to the lowest achievable temperature of 2 K due to the frustration in the hexagonal lattice or the moments at the Ho(2a) site are suppressed due to the formation of a singlet ground state. We failed to observe resonant magnetic scattering from Mn K-edge due to the presence of non-magnetic anisotropic tensor scattering at the magnetic Bragg peaks. Therefore, existence of a **c** component of the Mn^{3+} moments, predicted by symmetry analysis, can not be tested.

We have also determined the magnetic structures of Dy^{3+} and Er^{3+} moments in $DyMnO_3$ and $ErMnO_3$, respectively. Dy^{3+} moments order according to the magnetic representation Γ_3

in the intermediate temperature magnetic phase, ITP (between 68 K and 8 K). The Dy^{3+} moments are aligned and antiferromagnetically correlated along the **c** direction. The temperature dependence of the magnetic intensity in the ITP can also be explained by assuming a splitting of the ground state doublet by the exchange field from the ordered Mn^{3+} moments. In the low temperature phase, LTP (below 8 K), XRMS together with magnetization measurements indicate that Γ_2 is the magnetic representation and the Dy^{3+} moments are ferrimagnetically aligned in the hexagonal **c** direction. We note that the magnetic structure in $DyMnO_3$ is the same as in $HoMnO_3$ in the ITP, however, in the LTP the magnetic order is different: the Ho^{3+} moments are antiferromagnetically aligned according to Γ_1 in contrast to the ferrimagnetic alignment of the Dy^{3+} moments in $DyMnO_3$. It is likely that the striking difference is due to the complex interplay between the magnetism of the two sublattices, Dy^{3+}/Ho^{3+} and Mn^{3+}. For $ErMnO_3$, we conclude that no ITP exists and the Er^{3+} moments order ferrimagnetically below 3 K according to magnetic representation Γ_2.

For the ITP, the Dy^{3+} and Ho^{3+} moments order according to the same magnetic representation Γ_3 but no such magnetic structure could be found for the Er^{3+}. For both the Ho^{3+} and Dy^{3+}, magnetism in the ITP can be explained assuming an exchange interaction between R^{3+} and Mn^{3+} and a crystal electric field splitting of the R^{3+} ground state quasi-doublet/doublet. We note that the crystal electric field splitting for Dy ($\sim$6 meV) is larger than that of Ho ($\sim$1.3 meV), consistent with the larger ordering temperature for Dy^{3+} and points to a stronger exchange interaction between Dy^{3+} and Mn^{3+} than between Ho^{3+} and Mn^{3+}. The ordering in the ITP is controlled by R-O-Mn interaction. Since the rare-earth $4f$ levels are well localized, the interaction between rare-earths and Mn is mediated by $5d$'s of the rare-earths. Therefore, the interaction strength in a $RMnO_3$ series is determined by the $4f$-$5d$ exchange. In a naive picture, the $4f$-$5d$ overlap decreases for the heavy rare-earths due to lanthanide contraction and, therefore, one might expect that the strength of interaction decreases with increasing number of $4f$ electrons. In this picture, the absence of a scattering signal is quite consistent with the expectation that Er^{3+} should order at much lower temperature due to the smallness of exchange interaction between Er^{3+} and Mn^{3+}.

Our XRMS experiments on the series of $R\mathrm{MnO_3}$ compounds raise some interesting questions regarding the magnetism in this series that we have to await for future investigations. XRMS experiments predict that the magnetic moments at the Ho($2a$) site for $\mathrm{HoMnO_3}$ are either in a disordered or in a spin singlet ground state below 4.5 K. Further measurements such as measurements of spin-fluctuation spectrum and crystal electric field levels below 4.5 K by inelastic neutron scattering will be a direct test for these predictions. For $\mathrm{DyMnO_3}$, modeling of the temperature dependence for the magnetic moments of $\mathrm{Dy^{3+}}$ predicts a splitting, $\Delta = (5.8 \pm 0.8)$ meV, of the ground state doublet of $\mathrm{Dy^{3+}}$ below 68 K by the exchange interaction between $\mathrm{Dy^{3+}}$ and $\mathrm{Mn^{3+}}$. Inelastic neutron scattering measurements of crystal field excitation is highly desirable to validate this prediction. We also assumed for $\mathrm{DyMnO_3}$ that the higher transition temperature of the observed split transition at 68 K in the specific heat data as the magnetic ordering temperature of the $\mathrm{Mn^{3+}}$ moments and the lower one as the magnetic ordering temperature of the $\mathrm{Dy^{3+}}$ moments. Further measurements are necessary to validate this assumption. Since we know now the magnetic structure of $\mathrm{Dy^{3+}}$ from XRMS, a complementary neutron scattering measurement can shed light on the nature of the split transition.

After determining the magnetic structures of these multiferroics, we focused on determining the magnetic structure in an applied electric field. From the extensive single crystal SQUID magnetization, XRMS and XMCD as well as XMCD on powder samples for two different hexagonal multiferroics, $\mathrm{HoMnO_3}$ and $\mathrm{DyMn_3}$, we conclude that electric field is not responsible for the reported[9] ferromagnetic response of Ho moments. Therefore, the "Holy Grail" of multiferroics – a ferroelectric ferromagnet with the potential for controlling magnetism by external electric field still needs to be found.

BIBLIOGRAPHY

[1] J. Clerk Maxwell. A Dynamical Theory of the Electromagnetic Field . *Phil. Trans. R. Soc. Lond.*, 155:459, 1865.

[2] S. W. Cheong and M. Mostovoy. Multiferroics: a magnetic twist for ferroelectricity. *Nat. Mater.*, 6:13, 2007.

[3] Daniel Khomskii. Classifying multiferroics: Mechanisms and effects. *Physics*, 2:20, 2009.

[4] L. D. Landau and E. M. Lifshitz. *Electrodynamics of continuous media*. Pergamon Press, Oxford, New York, 1960.

[5] Hans Schmidt. On a magnetoelectric classification of materials. *Int. J. of Magnetism*, 4:337, 1973.

[6] I. E. Dzyaloshinskii. The magnetoelectric effect in antiferromagnetic materials. *Zhurnal Eksperimental'noi i Teoreticheskoi Fiziki*, 37:881, 1959.

[7] D. N. Astrov. Magnetoelectric effect in chromium oxide. *Sov. Phys. JETP*, 13:729, 1961.

[8] Nicola A. Hill. Why Are There so Few Magnetic Ferroelectrics? *J. Phys. Chem. B*, 104:6694, 2000.

[9] T. Lottermoser, T. Lonkai, U. Amann, D. Hohlwein, J. Ihringer, and M. Fiebig. Magnetic phase control by an electric field. *Nature*, 430:541, 2004.

[10] N. A. Spaldin and M. Fiebig. The Renaissance of Magnetoelectric Multiferroics. *Science*, 309:391, 2005.

[11] J. F. Scott. Application of Modern Ferroelctrics. *Science*, 315:954, 2007.

[12] M. Kenzelmann, A. B. Harris, S. Jonas, C. Broholm, J. Schefer, S. B. Kim, C. L. Zhang, S.-W. Cheong, O. P. Vajk, and J. W. Lynn. Magnetic Inversion Symmetry Breaking and Ferroelectricity in $TbMnO_3$. *Phys. Rev. Lett.*, 95:087206, 2005.

[13] G. Lawes, A. B. Harris, T. Kimura, N. Rogado, R. J. Cava, A. Aharony, O. Entin-Wohlman, T. Yildirim, M. Kenzelmann, C. Broholm, and A. P. Ramirez. Magnetically Driven Ferroelectric Order in $Ni_3V_2O_8$. *Phys. Rev. Lett.*, 95:087205, 2005.

[14] O. Heyer, N. Hollmann, I. Klassen, S. Jodlauk, L. Bohatỳ, P. Becker, J. A. Mydosh, T. Lorenz, and D. Khomskii. A new multiferroic material: $MnWO_4$. *J. Phys.: Condens. Matter*, 18:471, 2006.

[15] H. Murakawa, Y. Onose, F. Kagawa, S. Ishiwata, Y. Kaneko, and Y. Tokura. Rotation of an Electric Polarization Vector by Rotating Magnetic Field in Cycloidal Magnet $Eu_{0.55}Y_{0.45}MnO_3$. *Phys. Rev. Lett.*, 101:197207, 2008.

[16] Maxim Mostovoy. Ferroelectricity in Spiral Magnets. *Phys. Rev. Lett.*, 96:067601, 2006.

[17] I. A. Sergienko and E. Dagotto. Role of the Dzyaloshinskii-Moriya interaction in multiferroic perovskites. *Phys. Rev. B*, 73:094434, 2006.

[18] Maxim Mostovoy. Lecture Notes on "Multiferroics and magnetoelectric material" presented at Summer School on Multiferroics and Beyond, University of Calfornia, Santa Barbara, 2008.

[19] T. Goto, T. Kimura, G. Lawes, A. P. Ramirez, and Y. Tokura. Ferroelectricity and Giant Magnetocapacitance in Perovskite Rare-Earth Manganites. *Phys. Rev. Lett.*, 92:257201, 2004.

[20] T. Kimura, T. Goto, H. Shintani, K. Ishizaka, T. Arima, and Y. Tokura. Magnetic control of ferroelectric polarization. *Nature*, 426:55, 2003.

[21] T. Kimura, G. Lawes, T. Goto, Y. Tokura, and A. P. Ramirez. Magnetoelectric phase diagrams of orthorhombic $R\mathrm{MnO_3}$ (R = Gd, Tb, and Dy). *Phys. Rev. B*, 71:224425, 2005.

[22] N. Hur, S. Park, P. A. Sharma, J. S. Ahn, S. Guha, and S.-W Cheong. Electric polarization reversal and memory in a multiferroic material induced by magnetic fields. *Nature*, 429:392, 2004.

[23] Y. J. Choi, H. T. Yi, S. Lee, Q. Huang, V. Kiryukhin, and S.-W. Cheong. Ferroelectricity in an Ising Chain Magnet. *Phys. Rev. Lett.*, 100:047601, 2008.

[24] V. G. Zubkov, G. V. Bazuev, A. P. Tyutyunnik, and I. F. Berger. Synthesis, Crystal Structure, and Magnetic Properties of Quasi-One-Dimensional Oxides $\mathrm{Ca_3CuMnO_6}$ and $\mathrm{Ca_3Co_{1+x}Mn_{1-x}O_6}$. *J. Solid State Chem.*, 160:293, 2001.

[25] Naoshi Ikeda, Hiroyuki Ohsumi, Kenji Ohwada, Kenji Ishii, Toshiya Inami, Kazuhisa Kakurai, Youichi Murakami, Kenji Yoshii, Shigeo Mori, Yoichi Horibe, and Hijiri Kitô. Ferroelectricity from iron valence ordering in the charge-frustrated system $\mathrm{LuFe_2O_4}$. *Nature*, 436:1136, 2005.

[26] J. van den Brink and D.I. Khomskii. Multiferroicity due to charge ordering. *J. Phys.: Condens. Matter*, 20:434217, 2008.

[27] A. D. Christianson, M. D. Lumsden, M. Angst, Z. Yamani, W. Tian, R. Jin, E. A. Payzant, S. E. Nagler, B. C. Sales, and D. Mandrus. Three-Dimensional Magnetic Correlations in Multiferroic $\mathrm{LuFe_2O_4}$. *Phys. Rev. Lett.*, 100:107601, 2008.

[28] H. L. Yakel, W. C. Koehler, E. F. Bertaut, and E. F. Forrat. On the crystal structure of the manganese (III) trioxides of the heavy lanthanides and yttrium. *Acta Crystallogr., Sect. A: Found. Crystallogr.*, 16:957, 1963.

[29] B. B. Van Aken, T. T. M. Palstra, A. Filippetti, and N. A. Spaldin. The origin of ferroelectricity in magnetoelectric $\mathrm{YMnO_3}$. *Nat. Mater.*, 3:164, 2004.

[30] W. C. Koehler, H. L. Yakel, E. O. Wollan, and J. W. Cable. A note on the magnetic structures of rare earth manganese oxides. *Phys. Lett.*, 9:93, 1964.

[31] Philippe Coeuré, Philippe Guinet, Jean C. Peuzin, Georges Buisson, and E. Felix Bertaut. Ferroelectric properties of hexagonal orthomanganites of yttrium and rare earths. In *Proc. Int. Meeting on Ferroelectricity V*, page 332. Institute of Physics of the Czechoslovak Academy of Sciences, Prague, 1966.

[32] R. D. Shannon. Revised effective ionic radii and systematic studies of interatomic distances in halides and chalcogenides. *Acta Crystallogr., Sect. A: Found. Crystallogr.*, 32:751, 1976.

[33] P. G. Radaelli, L. C. Chapon, A. Daoud-Aladine, C. Vecchini, P. J. Brown, T. Chatterji, S. Park, and S.-W. Cheong. Electric Field Switching of Antiferromagnetic Domains in YMn_2O_5: A Probe of the Multiferroic Mechanism. *Phys. Rev. Lett.*, 101:067205, 2008.

[34] Y. Bodenthin, U. Staub, M. García-Fernández, M. Janoschek, J. Schlappa, E. I. Golovenchits, V. A. Sanina, and S. G. Lushnikov. Manipulating the Magnetic Structure with Electric Fields in Multiferroic $ErMn_2O_5$. *Phys. Rev. Lett.*, 100:027201, 2008.

[35] Seongsu Lee, Taekjib Choi, W. Ratcliff II, R. Erwin, S.-W. Cheong, and V. Kiryukhin. Single ferroelectric and chiral magnetic domain of single-crystalline $BiFeO_3$ in an electric field. *Phys. Rev. B*, 78:100101, 2008.

[36] George T. Rado. Observation and Possible Mechanisms of Magnetoelectric Effects in a Ferromagnet. *Phys. Rev. Lett.*, 13:335, 1964.

[37] T. H. O'dell and E. A. D. White. Electric field induced Faraday rotation in chromic oxide. *Philos. Mag.*, 22:649, 1970.

[38] P. G. Radaelli and L. C. Chapon. A neutron diffraction study of RMn_2O_5 multiferroics. *J. Phys.: Condens. Matter*, 20:434213, 2008.

[39] V. Yu. Ivanov, A. A. Mukhin, A. S. Prokhorov, A. M. Balbashov, and L. D. Iskhakova. Magnetic properties and phase transitions in hexagonal $DyMnO_3$ single crystals. *Phys. Solid State*, 48:1726, 2006.

[40] S. Nandi, A. Kreyssig, J. Q. Yan, M. D. Vannette, J. C. Lang, L. Tan, J. W. Kim, R. Prozorov, T. A. Lograsso, R. J. McQueeney, and A. I. Goldman. Magnetic structure of Dy^{3+} in hexagonal multiferroic $DyMnO_3$. *Phys. Rev. B*, 78:075118, 2008.

[41] A. Muñoz, J. A. Alonso, M. J. Martínez-Lope, M. T. Casáis, J. L. Martínez, and M. T. Fernández-Díaz. Evolution of the Magnetic Structure of Hexagonal $HoMnO_3$ from Neutron Powder Diffraction Data. *Chem. Mater.*, 13:1497, 2001.

[42] Th. Lonkai, D. G. Tomuta, U. Amann, J. Ihringer, R. W. A. Hendrikx, D. M. Többens, and J. A. Mydosh. Development of the high-temperature phase of hexagonal manganites. *Phys. Rev. B*, 69:134108, 2004.

[43] N. Hur, I. K. Jeong, M. F. Hundley, S. B. Kim, and S.-W. Cheong. Giant magnetoelectric effect in multiferroic $HoMnO_3$ with a high ferroelectric transition temperature. *Phys. Rev. B*, 79:134120, 2009.

[44] H. Sugie, N. Iwata, and K. Kohn. Magnetic Ordering of Rare Earth Ions and Magnetic-Electric Interaction of Hexagonal $R\mathrm{MnO}_3$ (R = Ho, Er, Yb or Lu). *J. Phys. Soc. Jpn.*, 71:1558, 2002.

[45] M. Fiebig, Th. Lottermoser, and R. V. Pisarev. Spin-rotation phenomena and magnetic phase diagrams of hexagonal $R\mathrm{MnO}_3$. *J. Appl. Phys.*, 93:8194, 2003.

[46] M. Fiebig, C. Degenhardt, and R. V. Pisarev. Magnetic phase diagram of $HoMnO_3$. *J. Appl. Phys.*, 91:8867, 2002.

[47] Th. Lonkai, D. Hohlwein, J. Ihringer, and W. Prandl. The magnetic structures of $YMnO_{3-\delta}$ and $HoMnO_3$. *Appl. Phys. A*, 74:S843, 2002.

[48] P. J. Brown and T. Chatterji. Neutron diffraction and polarimetric study of the magnetic and crystal structures of $HoMnO_3$ and $YMnO_3$. *J. Phys.: Condens. Matter*, 18:10085, 2006.

[49] O. P. Vajk, M. Kenzelmann, J. W. Lynn, S. B. Kim, and S.-W. Cheong. Magnetic Order and Spin Dynamics in Ferroelectric $HoMnO_3$. *Phys. Rev. Lett.*, 94:087601, 2005.

[50] R. R. Briss. *Symmetry and Magnetism.* North-Holland, Amsterdam, 1966.

[51] B. Lorenz, A. P. Litvinchuk, M. M. Gospodinov, and C. W. Chu. Field-Induced Reentrant Novel Phase and a Ferroelectric-Magnetic Order Coupling in $HoMnO_3$. *Phys. Rev. Lett.*, 92:087204, 2004.

[52] Thomas Lottermoser and Manfred Fiebig. Magnetoelectric behavior of domain walls in multiferroic $HoMnO_3$. *Phys. Rev. B*, 70:220407, 2004.

[53] S. Nandi, A. Kreyssig, L. Tan, J. W. Kim, J. Q. Yan, J. C. Lang, D. Haskel, R. J. McQueeney, and A. I. Goldman. Nature of Ho Magnetism in Multiferroic $HoMnO_3$. *Phys. Rev. Lett.*, 100:217201, 2008.

[54] P. M. Platzman and N. Tzoar. Magnetic scattering of x rays from electrons in molecules and solids. *Phys. Rev. B*, 2:3556, 1970.

[55] F. De Bergevin and M. Brunel. Observation of magnetic superlattice peaks by X-ray diffraction on an antiferromagnetic NiO crystal. *Phys. Lett. A*, 39:141, 1972.

[56] F. de Bergevin and M. Brunel. Diffraction of X-rays by magnetic materials. I. General formulae and measurements on ferro- and ferrimagnetic compounds. *Acta Crystallogr., Sect. A: Found. Crystallogr.*, 37:314, 1981.

[57] Doon Gibbs, D. E. Moncton, K. L. D'Amico, J. Bohr, and B. H. Grier. Magnetic x-ray scattering studies of holmium using synchro- tron radiation. *Phys. Rev. Lett.*, 55:234, 1985.

[58] Doon Gibbs, D. R. Harshman, E. D. Isaacs, D. B. McWhan, D. Mills, and C. Vettier. Polarization and resonance properties of magnetic x-ray scattering in holmium. *Phys. Rev. Lett.*, 61:1241, 1988.

[59] E. Balcar and S. W. Lovesey. *Theory of magnetic neutron and photon scattering.* Oxford University Press, 1989.

[60] J. P. Hannon, G. T. Trammell, M. Blume, and Doon Gibbs. X-Ray Resonance Exchange Scattering. *Phys. Rev. Lett.*, 61:1245, 1988.

[61] Doon Gibbs, G. Grübel, D. R. Harshman, E. D. Isaacs, D. B. McWhan, D. Mills, and C. Vettier. Polarization and resonance studies of x-ray magnetic scattering in holmium. *Phys. Rev. B*, 43:5663, 1991.

[62] M. Blume. Magnetic scattering of x rays. *J. Appl. Phys.*, 57:3615, 1985.

[63] M. Blume and Doon Gibbs. Polarization dependence of magnetic x-ray scattering. *Phys. Rev. B*, 37:1779, 1988.

[64] J. P. Hill and D. F. McMorrow. Resonant Exchange Scattering: Polarization Dependence and Correlation Function. *Acta Crystallogr., Sect. A: Found. Crystallogr.*, 52:236, 1996.

[65] J. W. Kim, Y. Lee, D. Wermeille, B. Sieve, L. Tan, S. L. Bud'ko, S. Law, P. C. Canfield, B. N. Harmon, and A. I. Goldman. Systematics of x-ray resonant scattering amplitudes in $R\mathrm{Ni}_2\mathrm{Ge}_2$ (R=Gd, Tb, Dy, Ho, Er, Tm): The origin of the branching ratio at the L edges of the heavy rare earths. *Phys. Rev. B*, 72:064403, 2005.

[66] Th. Brückel. Lecture notes on "Magnetic X-Ray Scattering".

[67] C. Detlefs, A. H. M. Z. Islam, A. I. Goldman, C. Stassis, P. C. Canfield, J. P. Hill, and D. Gibbs. Determination of magnetic-moment directions using x-ray resonant exchange scattering. *Phys. Rev. B*, 55:R680, 1997.

[68] Carsten Detlefs. *X-ray resonant exchange scattering of reare-earth nickel borocarbides.* PhD dissertation, Iowa State University, Ames, Iowa, USA, 1997.

[69] M. D. Hamrick. Theory of elestic x-ray resonant exchange scattering in lanthanides and actinides. *M. A. Thesis, Rice University*, 1990.

[70] J. W. Kim, A. Kreyssig, P. Ryan, E. Mun, P. C. Canfield, and A. I. Goldman. X-ray resonant magnetic scattering study of spontaneous ferrimagnetism. *Appl. Phys. Lett.*, 90:202501, 2007.

[71] S. Nandi, A. Kreyssig, Y. Lee, Yogesh Singh, J. W. Kim, D. C. Johnston, B. N. Harmon, and A. I. Goldman. Magnetic ordering in $EuRh_2As_2$ studied by x-ray resonant magnetic scattering. *Phys. Rev. B*, 79:100407(R), 2009.

[72] E. F. Bertaut. On group theoretical techniques in magnetic structure analysis. *J. Magn. Magn. Mater.*, 24:267, 1981.

[73] E. F. Bertaut. Representation analysis of magnetic structures. *Acta Crystallogr., Sect. A: Found. Crystallogr.*, 24:217, 1968.

[74] A. S. Wills. A new protocol for the determination of magnetic structures using simulated annealing and representational analysis (SARAh). *Physica B*, 276-278:680, 2000.

[75] A. S. Wills. Long-range ordering and representational analysis of the jarosites. *Phys. Rev. B*, 63:064430, 2001.

[76] A. P. Cracknell. *Magnetism in crystalline materials: applications of the theory of groups of cambiant symmetry.* Pergamon Press, New York, 1975.

[77] O. V. Kovalev. *Irreducible representations of the space groups.* Routledge, 1965.

[78] J. A. Izjumov, V. E. Naish, and R. P. Ozerov. *Neutron diffraction of magnetic materials.* Consultants Bureau, New York, 1991.

[79] J. Rossat-Mignod. In Kurt Sköld and David L. Price, editors, *Methods of Experimental Physics*, volume 23, chapter 19. Academic Press, Inc., Orlando, 1987.

[80] Th. Brückel, D. Hupfeld, J. Strempfer, W. Caliebe, K. Mattenberger, A. Stunault, N. Bernhoeft, and G. J. McIntyre. Antiferromagnetic order and phase transitions in

GdS as studied with X-ray resonance-exchange scattering. *Eur. Phys. J. B*, 19:475, 2001.

[81] J. C. Lang. X-ray Magnetic Circular Dichroism. In E. N. Kaufmann, editor, *Methods in materials research: a current protocols publication*, chapter 10c2. J. Wiley & Sons, New York, 2000.

[82] Paolo Carra, B. T. Thole, Massimo Altarelli, and Xindong Wang. X-ray circular dichroism and local magnetic fields. *Phys. Rev. Lett.*, 70:694, 1993.

[83] B. T. Thole, P. Carra, F. Sette, and G. van der Laan. X-ray circular dichroism as a probe of orbital magnetization. *Phys. Rev. Lett.*, 68:1943, 1992.

[84] Paolo Carra and Massimo Altarelli. Dichroism in the x-ray absorption spectra of magnetically ordered systems. *Phys. Rev. Lett.*, 64:1286, 1990.

[85] Xindong Wang, T. C. Leung, B. N. Harmon, and P. Carra. Circular magnetic x-ray dichroism in the heavy rare-earth metals. *Phys. Rev. B*, 47:9087, 1993.

[86] C. T. Chen, Y. U. Idzerda, H.-J. Lin, N. V. Smith, G. Meigs, E. Chaban, G. H. Ho, E. Pellegrin, and F. Sette. Experimental Confirmation of the X-Ray Magnetic Circular Dichroism Sum Rules for Iron and Cobalt. *Phys. Rev. Lett.*, 75:152, 1995.

[87] M. Fiebig, D. Fröhlich, K. Kohn, St. Leute, Th. Lottermoser, V. V. Pavlov, and R. V. Pisarev. Determination of the Magnetic Symmetry of Hexagonal Manganites by Second Harmonic Generation. *Phys. Rev. Lett.*, 84:5620, 2000.

[88] L. Tan, A. Kreyssig, J. W. Kim, A. I. Goldman, R. J. McQueeney, D. Wermeille, B. Sieve, T. A. Lograsso, D. L. Schlagel, S. L. Budko, V. K. Pecharsky, and K. A. Gschneidner, Jr. Magnetic structure of Gd_5Ge_4. *Phys. Rev. B*, 71:214408, 2005.

[89] O. P. Vajk, M. Kenzelmann, J. W. Lynn, S. B. Kim, and S.-W. Cheong. Neutron-scattering studies of magnetism in multiferroic $HoMnO_3$. *J. Appl. Phys.*, 99:08E301, 2006.

[90] B. Lorenz, F. Yen, M. M. Gospodinov, and C. W. Chu. Field-induced phases in $HoMnO_3$ at low temperatures. *Phys. Rev. B*, 71:014438, 2005.

[91] E. Galstyan, B. Lorenz, K. S. Martirosyan, F. Yen, Y. Y. Sun, M. M. Gospodinov, and C. W. Chu. Magnetic hysteretic phenomena in multiferroic $HoMnO_3$ single crystals and polycrystals with nano- and micrometer particle size. *J. Phys.: Condens. Matter*, 20:325241, 2008.

[92] M. N. Popova, S. A. Klimin, E. P. Chukalina, E. A. Romanov, B. Z. Malkin, E. Antic-Fidancev, B. V. Mill, and G. Dhalenne. High-resolution optical spectroscopy investigation of Nd_2BaNiO_5 and $Nd_{0.1}Y_{1.9}BaNiO_5$ and crystal-field parameters for rare-earth linear-chain nickelates. *Phys. Rev. B*, 71:024414, 2005.

[93] A. Zheludev, J. P. Hill, and D. J. Buttrey. X-ray magnetic scattering study of three-dimensional magnetic order in the quasi-one-dimensional antiferromagnet Nd_2BaNiO_5. *Phys. Rev. B*, 54:7216, 1996.

[94] Ravi Sachidanandam, T. Yildirim, A. B. Harris, Amnon Aharony, and O. Entin-Wohlman. Single-ion anisotropy, crystal-field effects, spin reorientation transitions, and spin waves in R_2CuO_4 (R=Nd, Pr, and Sm). *Phys. Rev. B*, 56:260, 1997.

[95] U. Ranon and K. Lee. Paramagnetic Resonance of Ho^{3+} in a Trigonal Site in SrF_2. *Phys. Rev.*, 188:539, 1969.

[96] V. Hardy, C. Martin, G. Martinet, and G. André. Magnetism of the geometrically frustrated spin-chain compound Sr_3HoCrO_6: Magnetic and heat capacity measurements and neutron powder diffraction. *Phys. Rev. B*, 74:064413, 2006.

[97] H. D. Zhou, J. A. Janik, B. W. Vogt, Y. J. Jo, L. Balicas, M. J. Case, C. R. Wiebe, J. C. Denyszyn, J. B. Goodenough, and J. G. Cheng. Specific heat of geometrically frustrated and multiferroic $RMn_{1-x}Ga_xO_3$ (R = Ho, Y). *Phys. Rev. B*, 74:094426, 2006.

[98] O. P. Vajk. Private comunications.

[99] M. Fiebig, C. Degenhardt, and R. V. Pisarev. Interaction of Frustrated Magnetic Sublattices in $ErMnO_3$. *Phys. Rev. Lett.*, 88:027203, 2001.

[100] T. Nomura, J. Masuzawa, and T. Katsufuji. Dynamical specific heat of two-phase coexistence in $R\mathrm{MnO}_3$. *Phys. Rev. B*, 74:220403, 2006.

[101] J. Voigt, J. Persson, J. W. Kim, G. Bihlmayer, and Th. Brückel. Strong coupling between the spin polarization of Mn and Tb in multiferroic $TbMnO_3$ determined by x-ray resonance exchange scattering. *Phys. Rev. B*, 76:104431, 2007.

[102] S. L. Chang. *Multiple Diffraction of X-rays in Crystals*. Springer-Verlag, 1984.

[103] Lizhi Tan. *Investigations of the $R_5(Si_xGe_{1-x})_4$ intermetallic compounds by X-ray resonant magnetic scattering*. PhD dissertation, Iowa Sate Unversity, Ames, Iowa, USA, 2008.

[104] K. D. Finkelstein, Qun Shen, and S. Shastri. Resonant x-ray diffraction near the iron K edge in hematite (α-Fe_2O_3). *Phys. Rev. Lett.*, 69:1612, 1992.

[105] Jun Kokubun, Ayako Watanabe, Masayoshi Uehara, Yoshiyuki Ninomiya, Hidetaka Sawai, Nobuyuki Momozawa, Kohtaro Ishida, and Vladimir E. Dmitrienko. Chiral and magnetic effects in forbidden x-ray scattering from antiferromagnetic hematite alpha -Fe_2O_3 and eskolaite Cr_2O_3. *Phys. Rev. B*, 78:115112, 2008.

[106] M. Blume. Magnetic effects in anomalous dispersion. In G. Materlik, C. J. Park, and K. Fischer, editors, *Resonant Anomalous X-ray Scattering*, chapter V. North-Holland, Netherlands, 1994.

[107] D. H. Templeton and L. K. Templeton. Polarized X-ray absorption and double refraction in vanadyl bisacetylacetonate. *Acta Crystallogr., Sect. A: Found. Crystallogr.*, 36:237, 1980.

[108] S. P. Collins, D. Laundy, and A Stunault. Anisotropic resonant diffraction from $HoFe_2$. *J. Phys.: Condens. Matter*, 13:1891, 2001.

[109] V. E. Dmitrienko. Forbidden reflections due to anisotropic X-ray susceptibility of crystals. *Acta Crystallogr., Sect. A: Found. Crystallogr.*, 39:29, 1983.

[110] A. Kirfel, A. Petcov, and K. Eichhorn. Anisotropy of anomalous dispersion in X-ray diffraction. *Acta Crystallogr., Sect. A: Found. Crystallogr.*, 47:180, 1991.

[111] Naoki Kamegashira, Hirohisa Satoh, and Satoshi Ashizuka. Synthesis and crystal structure of hexagonal $DyMnO_3$. *Mater. Sci. Forum*, 449-452:1045, 2004.

[112] F. Yen, C. dela Cruz, B. Lorenz, E. Galstyan, and Y. Y. Sun. Magnetic phase diagrams of multiferroic hexagonal $R\mathrm{MnO}_3$ (R = Er, Yb, Tm, and Ho). *J. Mater. Res.*, 22:2163, 2007.

[113] Brian G. Wybourne. *Spectroscopic Properties of Rare Earths.* Interscience Publishers, New York, 1965.

[114] D. Bravo, A. A. Kaminskiiz, and F. J. López. Electron paramagnetic resonance investigation of Dy^{3+} ions in $Bi_4Ge_3O_{12}$ single crystals. *J. Phys.: Condens. Matter*, 10:3261, 1998.

[115] J. Park, U. Kong, S. I. Choi, J.-G. Park, C. Lee, and W. Jo. Magnetic structure studies of $ErMnO_3$. *Appl. Phys. A*, 74:S802, 2002.

[116] C. H. Lee, R. K. Chang, and N. Bloembergen. Nonlinear Electroreflectance in Silicon and Silver. *Phys. Rev. Lett.*, 18:167, 1967.

[117] D. Adamenko, I. Klymiv, V. M. Duda, R. Vlokh, and O. Vlokh. Electrically and magnetically induced optical rotation in $Pb_5Ge_3O_{11}$:Cr crystals at the phase transition. 1. Electrogyration effect in $Pb_5Ge_3O_{11}$:Cr . *Ukrainian Journal of Physical Optics*, 8:42, 2007.

ACKNOWLEDGEMENTS

I would like to thank everyone who helped me in the last three years conducting research at Iowa State University.

First and foremost, I would like to thank my advisor Dr. Alan I. Goldman for his guidance, relentless patience and support throughout this research. Specifically, I like to thank him for meticulously editing this thesis within a very short period of time. I also thank him for exposing me to different areas of condensed matter physics. His belief in me always inspired me pursuing research and completing my graduate education.

I would also like to thank my *informal* co-advisor Dr. Andreas Kreyssig for acquainting me to all the instruments here at Ames and at Advanced Photon Source, Argonne, IL. I appreciate his help in writing papers and for his undaunted enthusiasm in answering any type of questions. I would like to thank my past lab-mate Dr. Lizhi Tan and present lab-mates Mingyu Kim and Gustav Rustan for their help and many fruitful discussions. I like to thank Dr. J. W. Kim, Dr. D. S. Robinson, Dr. Jonathan Lang, Dr. Daniel Haskel and Dr. Zahirul Islam at the Advanced Photon source for their help during experiments and intellectual contribution to this work. Specially, I thank Dr. J. W. Kim for giving me permission to wake him up at any time in the night during experiments at APS.

I like to thank Dr. J. Q. Yan for preparing single crystals and for basic characterizations. I would like to thank Dr. S. L. Budk'ko and Dr. M. D. Vannette for magnetization measurements. I like to thank Dr. Robert J. McQueeney for answering all my trivial questions during my first neutron scattering experience with him.

I would also like to express my sincere gratitude to Dr. Paul C. Canfield, Dr. Joerg Schmalian, Dr. Jianwei Qiu and Dr. Xiaoli Tan for serving on my thesis committee and for

many helpful comments and guidance on my research.

I would also like to thank all my friends at ISU whose companionship brought a lot of joy and laughter throughout my graduate studies especially my room-mates Bose and Ram and my tennis partner Debu.

Lastly, and most importantly, I am grateful to my sisters and my parents for their support and encouragement and, allowing me to come to USA. I am thankful to my maternal uncle, Sakshi Paul, for financial support during difficult times of our family. I acknowledge financial support during my Master's degree and before coming to USA, from UCO Bank, India.

Finally, my sincere gratitude to all my teachers who shaped my life and showed me this path. I specially thank Dr. Dipak Ghosh, Dr. A. K. Majumdar, Dr. Amit Dutta, Dr. Y. N. Mohapatra and Dr. Abinash Singh for teaching condensed matter physics.

The work at the Ames Laboratory and at the MU-CAT sector was supported by the US DOE under Contract No. DE-AC02-07CH11358. This work was supported by the Director of Energy Research, Office of Basic Sciences. Use of the Advanced Photon Source was supported by US DOE under Contract No. DE-AC02-06CH11357.